University of California
Santa Barbara

Soluto-inertial phenomenon: Driving colloidal migration over millimeter distances

A dissertation submitted in partial satisfaction
of the requirements for the degree

Doctor of Philosophy
in
Chemical Engineering

by

Anirudha Banerjee

Committee in charge:

Professor Todd Squires, Chair
Professor Javier Read de Alaniz
Professor Matthew Helgeson
Professor Rachel Segalman

September 2019

The Dissertation of Anirudha Banerjee is approved.

Professor Javier Read de Alaniz

Professor Matthew Helgeson

Professor Rachel Segalman

Professor Todd Squires, Committee Chair

July 2019

Soluto-inertial phenomenon: Driving colloidal migration over millimeter distances

Acknowledgements

Five years. It is an incredibly long period of time – to put things in perspective, about 10% of the productive years of an average human being. At this point you might be thinking that I will say something like – "oh, but these last five years were such a breeze" or "I didn't even realize I spent that much time working on my project!", but trust me when I say that these five years were extremely challenging. Had it not been for the support I received from the people I am about to mention next, I don't know if I would have been able to do this. My acknowldgements would be incomplete if I didn't throw in a cheesy quote right at the beginning, so at the expense of being a cliché, I will say that "I did get by with a little help from my advisor, my committee members, my family, and of course, my friends." – The Beatles (graduate student version).

Todd, I still don't know what I did to make you bestow your unwavering faith upon me, when you gave me this project to work on. I was a scared, unsure, first year student who had literally no clue what he was doing in graduate school, but you took me in your lab and gave me this opportunity – for that I will be forever grateful. You know, one could fill pages writing praises about your vision as a researcher and your ability to think about physical systems in a way that is so unique, yet impactful. I truly believe that if I could retain and implement even a fraction of what you have taught me, I would be able to comfortably sustain my scientific career. I have always admired the kind of trust you have in your students' ability to solve difficult problems on their own, without getting frustrated with them. It has not only made me a better researcher, but has also taught me how to be patient and accepting of others, and be respectful of everyone's perspective. I think that is, perhaps, the most profound effect you have had on my life. Thank you for being so supportive, taking such a keen interest in my successes and failures in graduate school, and investing so much of your personal time in making sure that I achieve my

goals.

I want to thank my committee members, Matt Helgeson, Javier Read de Alaniz and Rachel Segalman. Matt – thanks for telling me about your organogel system in great detail during my first year and letting me work with Paula Malo de Molina, Gwen Zhang and Juntae Kim in your lab. Had I not been working with those gels, I probably would not have made the serendipitous discovery that led to my first paper. Javier – thanks for teaching me a little bit of organic chemistry and introducing me to Zach Page and Neil Dolinski who taught me how to make the pNIPAm gels. You have always taken a keen interest in my project and made some brilliant suggestions that have greatly improved the quality of my work. Rachel – thanks for helping me stay focused on the big picture goals. Your advice during my committee meetings were always on point and gave me a lot of clarity in figuring out future research directions.

I want to thank all Squires group members, both old and new. It is unfortunate that most journals only publish "successful" experiments, but to get to that point requires a lot of tinkering and trouble-shooting. I was fortunate enough to always get the help and support that I needed to develop those successful experiments, from each and every member of the group. In all honesty, this work is a collective effort of the entire group. I would also like to thank the enthusiastic undergraduate students – Lisa Nguyen, Johanna Eriksson, and Megan Cavanaugh, who chose to start their scientific adventures under my guidance.

I want to thank all the fine folks that I met in Santa Barbara, whom I have the pleasure of calling my friends. In particular, I want to thank Rodrigo Nery Azevedo who taught me microfluidics and introduced me to The Smiths; Doug Vogus and Arash Nowbahar who treated me like their younger brother and taught me how to cope with graduate school, while never missing an opportunity to pick on me; Ian Williams who helped me develop a knack for image analysis; Harishankar Manikantan who shared my enthusiasm

for progressive rock music; Joe Barakat who made sure that I didn't completely lose my mind in my final year by constantly organizing game nights; my Indian clique – Anusha Pusuluri, Ekta Prashnani, Anchal Agarwal, Pratik Soni and Rucha Thakar who made sure that I wore traditional attire at least once every year during Diwali; my classmates – Justin Yoo, Jacob Monroe, and Tuan Nguyen who stuck together and provided constant moral support as well as witnessed together, the Taco Tuesday price at El Paseo rise from $7 to $9 over a period of four years!

I want to thank my parents, who have put in so much hard work to make sure that me and my brother get the best possible education. Thanks dad for making me reason out each and every thing in life and not take anything for granted. Mom, I know that I have never thanked you enough for staying up with me through countless nights, making sure that I understood every little detail in the book before a test. But know that all that I have achieved in life is because you persevered and taught me the true meaning of work ethic. Thanks for letting me pursue my dreams in the US, even though it meant being thousands of miles away from you guys. I would also like to thank my brother, Abhishek Banerjee, who has been a constant source of inspiration for me. Your altruism and humility, despite your many accomplishments are qualities that I always look up to. Thanks for making my life a thousand times simpler by holding my hand and showing me how to tackle real world problems (and scientific ones too!).

And finally, to my girlfriend, Meghna Jain, who has always been so supportive and encouraging throughout these five years. You are the one person that kept me sane, especially on days when I would come back home late at night after a failed experiment. Even though you were physically not there, your adorably stupid antics on FaceTime used to always cheer me up. Thanks for putting up with me and tolerating my rants about graduate school and research. I have been extremely fortunate to have you in my life, because your love truly brings out the best in me.

Curriculum Vitæ

Anirudha Banerjee

Education

Ph.D. in Chemical Engineering, University of California, Santa Barbara (UCSB) 2019

Graduate Certificate in Management Practice, UCSB 2018

B.Tech. in Chemical Engineering, Indian Institute of Technology (IIT) Kharagpur 2014

Research Experience

Graduate Student Researcher, UCSB January 2015 - July 2019

Research Intern, Procter and Gamble Co, Cincinnati, OH June 2018 - September 2018

Undergraduate Student Researcher, IIT Kharagpur August 2013 - July 2014

Publications

Banerjee A, Squires TM, Drop in additives for suspension manipulation: Colloidal motion induced by sedimenting soluto-inertial beacons. *in preparation*

Tang X, Shi N, **Banerjee A**, Abdel-Fattah A, Mashat A, Squires TM, Sculpting diffusiophoretic migration with reactive solutes. *in preparation*

Vogus DR, Angulo C, **Banerjee A**, Nowbahar A, Squires TM, The effect of solute interaction on diffusivity and permeability within PEG-DA hydrogels. *in preparation*

Banerjee A, Vogus DR, Squires TM, Design strategies for engineering soluto-inertial suspension interactions. ***Physical Review E*** (under review)

Banerjee A, Squires TM, Long-range, selective, on-demand suspension interactions: Combining and triggering soluto-inertial beacons. ***Science Advances*** (accepted)

Azevedo RN, **Banerjee A**, Squires TM (2017) Diffusiophoresis in ionic surfactant gradients. ***Langmuir*** 33(38): 9694-9702

Banerjee A, Williams I, Azevedo RN, Helgeson ME, Squires TM (2016) Soluto-inertial phenomena: Designing long-range, long-lasting, surface-specific interactions in suspensions. ***Proc Natl Acad Sci USA*** 113(31): 8612-8617 - **Feature article**

Conference Presentations

Banerjee A, Squires TM, Diffusiophoretic migration of colloids induced by freely falling soluto-inertial beacons. *13$^{\text{th}}$ International Symposium on Electrokinetics (E.L.K.I.N.) @ MIT* (2019) Cambridge, MA (Poster)

Banerjee A, Squires TM, Drop in additives for suspension manipulation. *Gordon Research Conference on Complex Active and Adaptive Material Systems* (2019) Ventura, CA (Poster)

Banerjee A, Squires TM, Drop in additives for suspension manipulation. *2018 AIChE Annual Meeting* (2018) Pittsburgh, PA (Oral)

Banerjee A, Squires TM, Directing millimeter scale colloidal migration with soluto-inertial beacons. *APS March Meeting* (2018) Los Angeles, CA (Oral)

Banerjee A, Squires TM, Enhancing controlled colloidal migration through engineering soluto-inertial synergy. *Gordon Research Conference* (Poster) & *Gordon Research Seminar on Colloidal, Macromolecular and Polyelectrolyte Solutions* (2018) Ventura, CA (**Invited talk**)

Banerjee A, Williams I, Azevedo RN, Helgeson ME, Squires TM, Soluto-inertial phenomena: Designing long-range, long-lasting, surface-specific interactions in suspensions. *2016 AIChE Annual Meeting* (2016) San Francisco, CA (Oral)

Banerjee A, Williams I, Azevedo RN, Helgeson ME, Squires TM, Soluto-inertial phenomena: Designing long-range, long-lasting, surface-specific interactions in suspensions. *90th ACS Colloid and Surface Science Symposium* (2016) Cambridge, MA (Oral)

Banerjee A, Azevedo RN, Paustian JS, Squires TM, Diffusiophoretic mobility measurements of colloids under surfactant gradients. *CeNS Workshop: "Channels and Bridges to the Nanoworld"* (2015) Venice, Italy (Poster)

Honors and Awards

Best Poster Award, 2019
13$^{\text{th}}$ International Symposium on Electrokinetics (E.L.K.I.N.) @ MIT.

UCSB Graduate Division **Dissertation Fellowship** 2019

UCSB Academic Senate **Doctoral Student Travel Award.** 2019

Best Oral Presentation Award, 2018
11$^{\text{th}}$ Clorox-Amgen Graduate Student Symposium, UCSB.

UCSB Art of Science **Honorable Mention** – 2018
scientific "art-work" displayed at UCSB Library and the MOXI museum.

Best Overall Presentation, UCSB Chemical Sciences Student Seminar. 2018

Nominated by the Department of Chemical Engineering for the 2018
UCSB Academic Senate **Outstanding Teaching Assistant Award.**

Schlinger Fellowship for **Excellence in Chemical Engineering Research**. 2017

Semi-finalist in UCSB Grad Slam – 2017
a campus wide competition for the best three minute talk by a graduate student.

Abstract

Soluto-inertial phenomenon: Driving colloidal migration over millimeter distances

by

Anirudha Banerjee

Liquid suspensions of micron-scale particles and drops play a ubiquitous role in a broad spectrum of materials of central importance to modern life. A suite of interactions has long been known and exploited to formulate such suspensions; however, all such interactions act over less than a micron in water – and often much less. Here, we introduce a concept to design and engineer non-equilibrium interactions in suspensions, which are particle surface-dependent, may last for hundreds of seconds, and extend hundreds of times farther than is currently possible.

First, we show that these interactions rely on diffusiophoresis which refers to the migration of colloids under concentration (or chemical potential) gradients. Three ingredients are required to design the soluto-inertial interactions – i) chemical "beacons" that establish and sustain solute fluxes, ii) particles that respond to the fluxes and migrate via diffusiophoresis, and iii) solute that mediates the interaction between the suspended colloids and the beacon.

In subsequent chapters, we highlight the versatility of the SI concept and introduce distinct strategies to manipulate solute gradients, and hence suspension behavior, using beacons with different physico-chemical properties. We demonstrate on-demand particle migration using beacons that can be actuated with a trigger. We then show the synergy between multiple, distinct beacons that modify solute fluxes in solution in a way that allows directed, yet selective colloidal migration to specific target sites. Moreover, we provide a general conceptual framework to enable direct prediction of the range, duration

and strength of the SI effects in suspension, for a given beacon-solute pair.

While most of the work presented here involves suspension interactions mediated by fixed, cylindrical beacons in well controlled microfluidic devices, we conclude by showing manipulation of bulk suspensions by freely falling, spherical beacons. The beacon forms a solute wake as it sediments, which subsequently diffuses out, inducing diffusiophoretic migration of nearby suspended objects. Motivated by this simple observation, we eventually envision freely suspended beacons, that will not only establish solute fluxes, but also migrate in response, thereby suggesting new possibilities in active matter.

The conceptual versatility of the soluto-inertial interactions presented here suggests new capabilities for sorting and separating colloidal mixtures, targeting particle delivery to specific sites, enhancing rates of suspension flocculation, and synthesizing novel materials.

Contents

List of Figures

List of Tables

Chapter 1

Introduction to suspension interactions

1.1 Colloids in everyday products

Colloidal suspensions and emulsions of 10 nm - 10 μm particles play a central role in a wide variety of industrial, technological, biological, and everyday processes. Everyday goods including shampoos, cosmetics,[1,2] inks, vaccines, paints[3] and foodstuffs[4,5] as well as industrial products such as drilling muds, ceramics and pesticides[6–8] rely fundamentally on stably suspended microparticles for their creation and/or operation. This incredible versatility derives from the extensive variety of properties (*e.g.* mechanical, optical, and chemical) attainable in suspension through a generic set of physico-chemical strategies.[9–12] A proper understanding of the stability and dynamics of suspensions in general thus underpins both fundamental science and technological applications.

The properties and performance of suspensions depend preeminently on the effective interactions between particles. The last few decades have seen critical inventions that have enabled direct visualization of these interaction forces. Earlier work by Derjaguin,[13]

Overbeek & Sparnaay,[14] and Tabor & Winterton[15] ultimately led Israelachvili & Tabor to develop the Surfaces Forces Apparatus (SFA)[16] that could resolve measurements on the scale of a nanometer, using crossed cylinders covered with mica sheets. Several independent experimental measurements with the SFA have confirmed the existence of both attractive as well as repulsive interactions and other molecular level complex forces between colloidal surfaces.[17]

1.2 Equilibrium colloidal interactions, DLVO theory

The unique properties that can be attributed to colloidal systems, especially their stability, are a consequence of the delicate balance between the various inter-particle interaction forces. The celebrated Derjaguin-Landau-Verwey-Overbeek (DLVO) theory[18–20] balances electrostatic interactions (typically repulsive) between charged colloids – as screened by ions in the surrounding electrolyte – against van der Waals attractions, and successfully predicts the stability, phase behavior, and response of electrostatically stabilized suspensions.

Figure 1.1 shows the typical DLVO curve, where the interaction energy (or potential) between two charged colloids is plotted against their separation distance. Key things to note for colloidal stability are the occurrences of the primary and secondary minimum (Fig. 1.1 top inset) and an energy barrier in the potential energy landscape. Particle surfaces can come into irreversible adhesive contact (due to van der Waals attraction) if they reach the primary minimum, however, they must overcome the energy barrier (due to electrostatic repulsion) in order to do so. One way to lower the energy barrier is to decrease the surface potential by increasing the salt concentration (Fig. 1.1 bottom inset). However, particles might still come into contact in a secondary minimum, even in the presence of a high energy barrier, but adhesion is much weaker and typically reversible.

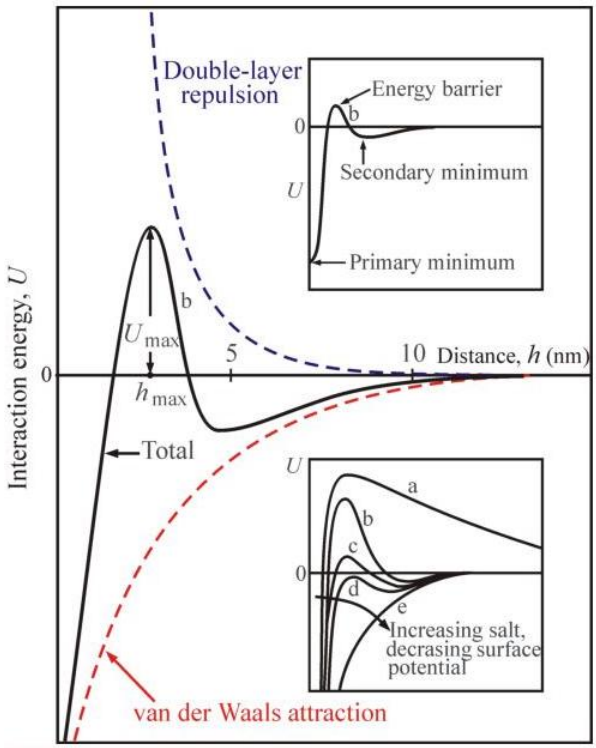

Figure 1.1: DLVO theory. The balance between van der Waals attractive forces (red dashed curve) and electrostatic repulsive forces (blue dashed curve) results in a potential energy landscape that can predict the stability of suspensions. Top Inset - when two charged particles come close to each other, they first encounter a secondary minimum in potential energy, where they can come into reversible contact. They must then cross an energy barrier to finally come into irreversible contact at the primary minimum. Bottom inset - the strength of this energy barrier may be lowered by 'screening' the surface charge of particles by increasing the salt concentration of solution. Figure adapted from *Intermolecular and Surface Forces*.[40]

1.3 Equilibrium colloidal interactions, beyond DLVO

Additional (non-DLVO) forces can either be naturally present or can also be used to stabilize or destabilize colloidal suspensions. Oscillatory solvation forces arise when liquid molecules are forced to order between two surfaces or within confined spaces.[21,22] Additionally, hydration forces arise when the liquid hydrogen bonding network between two surfaces is disrupted.[23] These forces are typically repulsive for hydrophilic surfaces

as water molecules can strongly bind to such surfaces. Grafted or adsorbed macromolecules provide short-range steric repulsions that stabilize suspended particles against van der Waals-induced flocculation.[24–27] By contrast, non-adsorbed macromolecules that remain dispersed in solution introduce entropic depletion attractions whose strength and range is set by the size and concentration of depletants.[28,29] Such depletion interactions scale with thermal energy (k_BT), and thus enable tunable and reversible attractions.[30,31] Clever design of shaped or patterned colloids yields 'lock-and-key' colloidal interactions[32,33] and so-called 'colloidal molecules'.[34,35] Grafting ligand-functionalized molecules to colloidal surfaces enables molecular sensing,[36,37] and sophisticated design of colloidal self-assembly.[38,39]

1.4 Extending the range of equilibrium colloidal interactions

Despite the past century's advances in the understanding, control and engineering of colloidal forces, the range of colloidal interactions remains fundamentally limited. van der Waals interactions extend for tens of nanometers[40–42] (Fig. 1.1). Steric repulsions[40,43] and depletion attractions[28,40,44] are limited by the size of the adsorbed, grafted, or suspended macromolecules, typically in the $\sim 10-100$ nm range. Of colloidal interactions, electrostatics have the longest range, yet are fundamentally limited by the (Debye) length scale over which the surface charge is screened by electrolyte ions:[26,40,43] the largest possible Debye screening length in room temperature aqueous suspensions is $\leqslant 1$ μm, and more typically between 1 – 100 nm (Fig. 1.1). Longer screening lengths are possible in non-polar solvents, but control and stabilization of non-aqueous charges and suspensions remains challenging.[45–48]

Magnetic and hydrodynamic interactions are unscreened and can extend to longer ranges;[26,43] but are essentially indiscriminate and less easily controlled, designed, or tuned. Defects introduced by particles in liquid crystals give rise to inter-particle forces over particle length scales;[49,50] yet are limited to liquid crystalline materials. Interaction lengthscales can further be increased by applying external fields to drive colloidal systems out of equilibrium,[51,52] e.g. using optical,[53–55] electric[56–58] and magnetic fields;[59,60] shear flow,[61,62] confinement[63] and interfacial curvature.[64,65] However, constant user input is required to reliably apply these external fields and monitor the response of the sytem, making it challenging to design sustained, long-range particle interactions in a controlled manner.

1.5 Motivation for this work

The goal of this work is to break the sub micron lengthscale limitations imposed by typical equilibrium interactions, with minimal intervention required from the user. We demonstrate, for the first time, controlled colloidal motion persisting over millimeter distances using solute concentration gradients generated *in-situ*. Migration of colloids under such gradients is known as diffusiophoresis, where the speed and even direction of colloidal migration depends upon the interactions between the solute and the colloid surface chemical properties. This chemical specificity gives users the flexibility to tune and design these interactions, by simply selecting the appropriate solute-particle combination. Moreover, despite the non-equilibrium nature of these interactions, we show that particle migration can be sustained for tens of minutes, by choosing materials that maintain the solute gradients over long durations.

The focus of this dissertation is to introduce this versatile concept by showing the experimental realization of the phenomenon and the various ways in which users may

generate and sustain concentration gradients. At the same time, we also provide a general theoretical framework with the goal of facilitating easy prediction of the range and duration of these interactions as well as selection of the right ingredients. Finally, we speculate the role that these novel interactions might play in advancing the field of active matter and demonstrate our efforts towards realizing fully autonomous behavior i.e. particles that generate gradients and also migrate in response.

1.6 Organization of thesis

Chapter 2 gives a brief background on diffusiophoresis, which refers to the motion of colloids under gradients of solute concentration (or chemical potential). We explore some of the basic physics of the 'screening layer' around a charged particle at equilibrium (electrostatics) and its response to externally applied potential fields (electrokinetics). Chapter 3 describes the concept of "soluto-inertial" interactions, that yield long-range, long-lasting and chemically specific particle migration in suspensions. Chapter 4 further highlights the versatility of the phenomenon, by introducing capabilities that allow on-demand suspension interactions and directed yet selective delivery of particles from one location to another. Chapter 5 provides tools that enable theoretical prediction of the soluto-inertial effect, for different combinations of the ingredients chosen to design the interactions.

The proof of principle demonstrations described in Chapters 3 and 4 involve experiments performed in well controlled, confined microfluidic geometries. Chapter 6 aims to extend the concept to apply to bulk suspensions, where soluto-inertial "additives" induce diffusiophoretic migration of neighboring colloids. Finally, Chapter 7 touches upon some of the applications of the soluto-inertial concept, such as guiding particles to quickly navigate complex geometries, where transport is otherwise diffusion limited. Moreover, it

also describes “soluto-capillary” motion as an alternative transport mechanism in systems where diffusiophoretic motion is suppressed. Chapter 8 summarizes the key findings from this research and offers ideas to apply the concept of soluto-inertial interactions to develop novel active material systems.

Bibliography

[1] Maitland G. Transforming "formulation": systematic soft materials design. *Soft Matter.* 2005; 1(2): 93–94.

[2] Hougeir FG, Kircik L. A review of delivery systems in cosmetics. *Dermatologic Therapy.* 2012; 25(1): 234–237.

[3] Goehring L, Li J, Kiatkirakajorn PC. Drying paint: from micro-scale dynamics to mechanical instabilities. *Phil. Trans. R. Soc. A.* 2017; 375: 20160161.

[4] Ubbink J. Soft matter approaches to structured foods: from "cook-and-look" to rational food design? *Faraday Discussions.* 2012; 158: 9.

[5] McClements DJ. The future of food colloids: Next-generation nanoparticle delivery systems. *Current Opinion in Colloid and Interface Science.* 2017; 28: 7–14.

[6] Lehn JM. Perspectives in chemistry - aspects of adaptive chemistry and materials. *Angewandte Chemie - International Edition.* 2015; 54(11): 3276–3289.

[7] Saldanha PL, Lesnyak V, Manna L. Large scale syntheses of colloidal nanomaterials. *Nano Today.* 2017; 12: 46–63.

[8] Gupta A, Eral HB, Hatton TA, Doyle PS. Nanoemulsions: formation, properties and applications. *Soft Matter.* 2016; 12(11): 2826–2841.

[9] Dickinson E. Colloids in food: Ingredients, structure, and stability. *Annual Review of Food Science and Technology.* 2015; 6: 211–233.

[10] Joshi YM. Dynamics of colloidal glasses and gels. *Annual review of chemical and biomolecular engineering.* 2014; 5: 181–202.

[11] Finne-Wistrand A, Albertsson AC. The use of polymer design in resorbable colloids. *Annual Review of Materials Research.* 2006; 36: 369–395.

[12] Zhang J, Luijten E, Granick S. Toward design rules of directional janus colloidal assembly. *Annual Review of Physical Chemistry.* 2014; 66: 581–600.

[13] Derjaguin BV, Titijevskaia AS, Abricossova II, Malkina AD. Investigations of the forces of interaction of surfaces in different media and their application to the problem of colloid stability. *Discuss. Faraday Soc..* 1954; 18: 24-41.

[14] Overbeek JTG, Sparnaay MJ. Classical coagulation. london-van der waals attraction between macroscopic objects. *Discuss. Faraday Soc..* 1954; 18: 12-24.

[15] Tabor D, Winterton RHS. The direct measurement of normal and retarded van der waals forces. *Proceedings of the Royal Society of London. A. Mathematical and Physical Sciences.* 1969; 312(1511): 435-450.

[16] Israelachvili JN, Tabor D. The measurement of van der waals dispersion forces in the range 1.5 to 130 nm. *Proceedings of the Royal Society of London. A. Mathematical and Physical Sciences.* 1972; 331(1584): 19-38.

[17] Israelachvili JN, Min Y, Akbulut M, et al. Recent advances in the surface forces apparatus (sfa) technique. 2010.

[18] Derjaguin B, Landau L. Theory of the stability of strongly charged lyophobic sols and of the adhesion of strongly charged particles in solutions of electrolytes. *Acta Physico Chemica URSS.* 1941; 14: 633–662.

[19] Verwey EJW. Theory of the stability of lyophobic colloids. *J. Phys. Chem..* 1948; 51(3): 631–636.

[20] Verwey EJW, Overbeek JTG. *Theory of the stability of lyophobic colloids.* Elsevier 1948.

[21] Israelachvili J. Solvation forces and liquid structure, as probed by direct force measurements. *Accounts of Chemical Research.* 1987; 20(11): 415-421.

[22] Koga K. Solvation forces and liquid–solid phase equilibria for water confined between hydrophobic surfaces. *The Journal of Chemical Physics.* 2002; 116(24): 10882-10889.

[23] Parsegian V, Zemb T. Hydration forces: Observations, explanations, expectations, questions. *Current Opinion in Colloid & Interface Science.* 2011; 16(6): 618 - 624.

[24] Napper DH. *Polymeric stabilization of colloidal dispersions.* Academic Press 1983.

[25] Tadros TF. Steric Stabilisation and Flocculation by Polymers. *Polymer Journal.* 1991; 23: 683–696.

[26] Russel W, Saville D, Schowalter W. *Colloidal Dispersions.* Cambridge Monographs on MechanicsCambridge University Press 1989.

[27] Mewis J, Wagner N. *Colloidal Suspension Rheology.* Cambridge Series in Chemical EngineeringCambridge University Press 2011.

[28] Asakura S, Oosawa F. Interaction between particles suspended in solutions of macromolecules. *Journal of Polymer Science.* 1958; 33(126): 183–192.

[29] Vrij A. Polymers at interfaces and the interactions in colloidal dispersions. *Pure and Applied Chemistry.* 1976; 48(4): 471–483.

[30] Edwards TD, Yang Y, Everett WN, Bevan MA. Reconfigurable multi-scale colloidal assembly on excluded volume patterns. *Scientific Reports.* 2015; 5: 13612.

[31] Colon-Melendez L, Beltran-Villegas DJ, Van Anders G, et al. Binding kinetics of lock and key colloids. *Journal of Chemical Physics.* 2015; 142: 174909.

[32] Sacanna S, Irvine WTM, Chaikin PM, Pine DJ. Lock and key colloids. *Nature.* 2010; 464(7288): 575–578.

[33] Ashton DJ, Jack RL, Wilding NB. Porous liquid phases for indented colloids with depletion interactions. *Physical Review Letters.* 2015; 114(23): 237801.

[34] Teich EG, Anders GV, Klotsa D, Dshemuchadse J, Glotzer SC. Clusters of polyhedra in spherical confinement. *PNAS.* 2015; 113(6): E669–E678.

[35] Glotzer SC, Solomon MJ. Anisotropy of building blocks and their assembly into complex structures. *Nature Materials.* 2007; 6: 557–562.

[36] Pregibon DC, toner M, Doyle PS. Multifunctional Encoded Particles for High-Throughput Biomolecule Analysis. *Science.* 2006; 315: 1393–1396.

[37] Geerts N, Eiser E. DNA-functionalized colloids: Physical properties and applications. *Soft Matter.* 2010; 6(19): 4647–14.

[38] Rogers WB, Crocker JC. Direct measurements of dna-mediated colloidal interactions and their quantitative modeling. *Proceedings of the National Academy of Sciences.* 2011; 108(38): 15687–92.

[39] McGinley JT, Jenkins I, Sinno T, Crocker JC. Assembling colloidal clusters using crystalline templates and reprogrammable dna interactions. *Soft Matter.* 2013; 9: 9119.

[40] Israelachvili JN. *Intermolecular and Surface Forces.* Academic Press3rd ed. 2011.

[41] Hamaker H. The London—van der Waals attraction between spherical particles. *Physica.* 1937; 4(10): 1058–1072.

[42] Lifshitz EM. The Theory of Molecular Attractive Forces between Solids. *Soviet Physics.* 1956; 2(1): 73–83.

[43] Ivlev A, Löwen H, Morfill G, Royall CP. *Complex Plasmas and Colloidal Dispersions.* World Scientific 2012.

[44] Vincent B. The calculation of depletion layer thickness as a function of bulk polymer concentration. *Colloids and Surfaces.* 1990; 50: 241–249.

[45] Hsu MF, Dufresne ER, Weitz DA. Charge stabilization in nonpolar solvents. *Langmuir.* 2005; 21(11): 4881–4887.

[46] Smith GN, Hallett JE, Eastoe J. Celebrating Soft Matter's 10th Anniversary: Influencing the charge of poly(methyl methacrylate) latexes in nonpolar solvents. *Soft Matter.* 2015.

[47] Rios de Anda I, Statt A, Turci F, Royall CP. Low-density crystals in charged colloids: Comparison with Yukawa theory. *Contributions to Plasma Physics.* 2015; 55(2-3): 172–179.

[48] Sainis SK, Germain V, Mejean CO, Dufresne ER. Electrostatic Interactions of Colloidal Particles in Nonpolar Solvents: Role of Surface Chemistry and Charge Control Agents. *Langmuir.* 2008; 24(4): 1160–1164.

[49] Guzmán O, Kim EB, Grollau S, Abbott NL, Pablo JJ. Defect Structure around Two Colloids in a Liquid Crystal. *Phys. Rev. Lett..* 2003; 91(23): 235507–4.

[50] Koenig Jr. GM, Pablo JJ, Abbott NL. Characterization of the Reversible Interaction of Pairs of Nanoparticles Dispersed in Nematic Liquid Crystals. *Langmuir.* 2009; 25(23): 13318–13321.

[51] Löwen H. Particle-resolved instabilities in colloidal dispersions. *Soft Matter.* 2010; 6: 3133–3142.

[52] Löwen H. Colloidal dispersions in external fields. *Journal of Physics: Condensed Matter.* 2012; 24: 460201.

[53] Brunner M, Bechinger C. Phase behavior of colloidal molecular crystals on triangular light lattices. *Physical Review Letters.* 2002; 88(24): 248302.

[54] Evers F, Hanes RDL, Zunke C, et al. Colloids in light fields: Particle dynamics in random and periodic energy landscapes. *European Physical Journal: Special Topics.* 2013; 222(11): 2995–3009.

[55] Palacci J, Sacanna S, Steinberg AP, Pine DJ, Chaikin PM. Living crystals of light-activated colloidal surfers. *Science.* 2013; 339: 936–340.

[56] Juárez JJ, Mathai PP, Liddle JA, Bevan MA. Multiple electrokinetic actuators for feedback control of colloidal crystal size. *Lab on a Chip.* 2012; 12: 4063–4070.

[57] Vissers T, Wysocki A, Rex M, et al. Lane formation in driven mixtures of oppositely charged colloids. *Soft Matter.* 2011; 7(6): 2352.

[58] Yethiraj A, Blaaderen AV. A colloidal model system with an interaction tunable from hard sphere to soft and dipolar. *Nature.* 2003: 513–517.

[59] Dillmann P, Maret G, Keim P. Two-dimensional colloidal systems in time-dependent magnetic fields. *The European Physical Journal Special Topics.* 2013; 222: 2941–2959.

[60] Martinez-Pedrero F, Cebers A, Tierno P. Dipolar rings of microscopic ellipsoids: Magnetic manipulation and cell entrapment. *Physical Review Applied.* 2016; 6(3): 1–11.

[61] Williams I, Oguz EC, Speck T, Bartlett P, Löwen H, Royall CP. Transmission of torque at the nanoscale. *Nature Physics.* 2016; 12: 98–103.

[62] Eisenmann C, Kim C, Mattsson J, Weitz Da. Shear melting of a colloidal glass. *Physical Review Letters.* 2010; 104: 8–11.

[63] Löwen H. Twenty years of confined colloids: from confinement-induced freezing to giant breathing. *Journal of Physics: Condensed Matter.* 2009; 21: 474203.

[64] Cavallaro M, Botto L, Lewandowski EP, Wang M, Stebe KJ. Curvature-driven capillary migration and assembly of rod-like particles. *Proceedings of the National Academy of Sciences.* 2011; 108(52): 20923–20928.

[65] Ershov D, Sprakel J, Appel J, Cohen Stuart Ma, Gucht J. Capillarity-induced ordering of spherical colloids on an interface with anisotropic curvature. *Proceedings of the National Academy of Sciences of the United States of America.* 2013; 110: 9220–4.

Chapter 2

Diffusiophoresis: Colloidal migration under solute concentration gradients

Most surfaces develop a surface charge when in contact with water. Depending on solution conditions with which the surface is in contact, certain surface groups might dissociate to give the surface a net positive or negative charge. On the other hand, certain ionic species in solution might have a stronger binding affinity towards a given surface than others, thereby adsorbing onto the surface.[1]

When an electrolyte solution comes into contact with such a charged surface, ions of the opposite charge, counter-ions, get electrostatically attracted by the surface, while like charge co-ions are repelled. The counter-ions also experience an entropic force as they get more concentrated, causing them to be repelled from the surface. The electrostatic and entropic forces balance each other at equilibrium, at a distance known as the Debye screening length, λ_D. The electrostatic effects of the charged surface are screened over this length.

2.1 The electric double layer: Poisson-Boltzmann equation

A charged surface, along with the region over which its charge is screened (λ_D) are collectively known as the electric double layer (EDL). The ions in the EDL set up a spontaneous electrostatic field, ϕ, which is governed by the Poisson equation,

$$\nabla^2\phi = -\frac{\rho}{\epsilon}, \tag{2.1}$$

where ρ is the charge density and ϵ is the permittivity of water. For a monovalent, binary electrolyte $\rho = e(n_+ - n_-)$, where e is the elementary charge. The ions in the EDL then respond to the potential, ϕ and at equilibrium rearrange according to the Boltzmann distribution,

$$n_\pm = n_0 \exp\left(\mp\frac{e\phi}{k_BT}\right), \tag{2.2}$$

where k_BT represents thermal energy and n_0 is the bulk ion concentration. A mean field approximation further suggests that the ions respond to the field established by those same ions. Therefore, inserting $n_\pm$ from Eq. 2.2 into Poisson's equation (Eq. 2.1) yields the Poisson-Boltzmann equation

$$\nabla^2\phi = -\frac{n_0 e}{\epsilon}\left(\exp\left(-\frac{e\phi}{k_BT}\right) - \exp\left(\frac{e\phi}{k_BT}\right)\right) = \frac{2n_0 e}{\epsilon}\sinh\left(\frac{e\phi}{k_BT}\right). \tag{2.3}$$

$e\phi/k_BT$ is a dimensionless quantity which gives the strength of the electrostatic potential, ϕ relative to the thermal potential

$$\phi_{\mathrm{Th}} = \frac{k_BT}{e}. \tag{2.4}$$

Non-dimensionalizing Eq. 2.3 by ϕ_{Th} then gives

$$\nabla^2\tilde{\phi} = \kappa^2 \sinh\tilde{\phi}, \tag{2.5}$$

where $\tilde{\phi} = \phi/\phi_{\mathrm{Th}}$. Moreover,

$$\kappa^{-1} = \lambda_D = \sqrt{\frac{\epsilon k_B T}{2n_0 e^2}} \tag{2.6}$$

is the expression for the Debye length, λ_D discussed previously. For small applied potentials ($\tilde{\phi} \ll 1$), Eq. 2.5 can be linearized ($\sinh\phi \approx \phi$) to give

$$\nabla^2\phi = \kappa^2\phi. \tag{2.7}$$

For a planar surface, Eq. 2.7 can be solved to obtain

$$\phi = \zeta e^{-\kappa z}. \tag{2.8}$$

ζ is known as the zeta potential of a charged surface and is defined as the potential drop across the diffuse layer of counter ions.

2.2 Electrokinetics: Electrophoresis and diffusiophoresis

So far we have only looked at the characteristics of the EDL under static, equilibrium conditions. We now turn to investigating the response of the ions in the EDL when an external field is applied in the bulk. Different electrokinetic effects emerge, depending on the nature of the external field. For example, an applied electric field forces the

electrically charged EDL to drive an electro-osmotic flow along a stationary surface (Fig. 2.1A). If the surface is free to move (e.g. a charged colloidal particle), however, it responds by migrating through the fluid via electrophoresis (Fig. 2.1B). On the other hand, a concentration gradient of ions in the bulk solution creates a gradient in the EDL thickness, which subsequently causes an entropically driven diffusioosmotic flow along the surface (Fig. 2.1C). Free surfaces of charged particles under the influence of ionic strength gradients respond by migrating via diffusiophoresis (Fig. 2.1D).

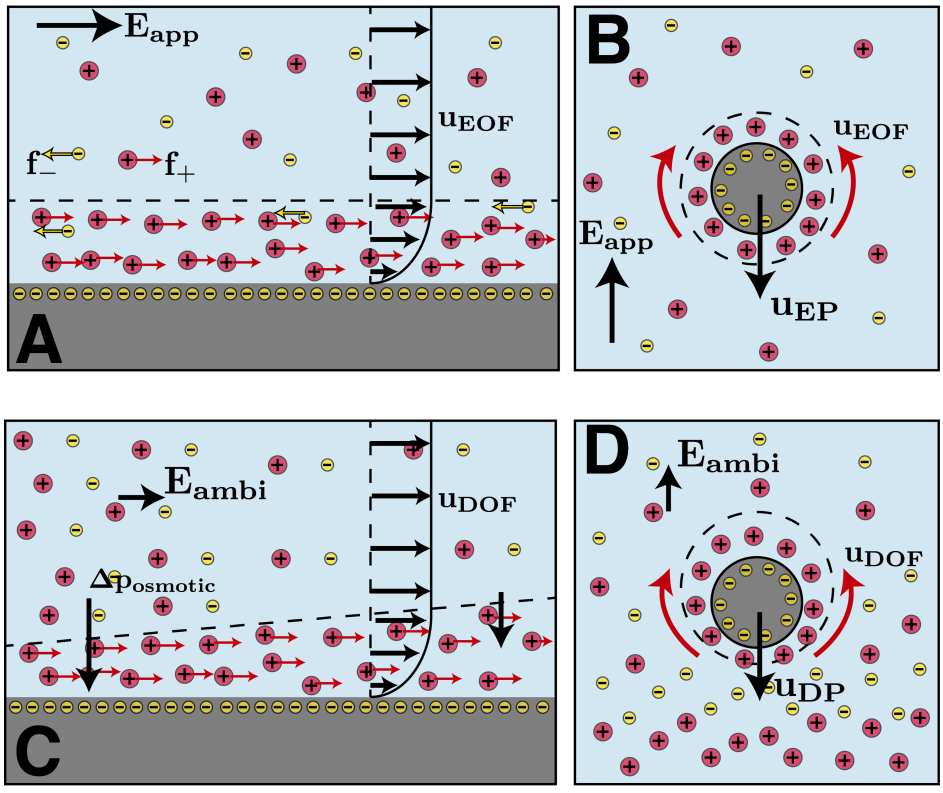

Figure 2.1: Four different electrokinetic effects. (A) An externally applied electric field (E_{app}) drives an electroosmotic fluid flow (u_{EOF}) in the EDL along a charged surface. (B) The free surface of a charged particle responds to the electroosmotic "slip" flow by migrating through the fluid via electrophoresis (u_{EP}). (C) A concentration gradient of ions in the bulk solution, on the other hand, drives a diffusioosmotic flow (u_{DOF}) along the charged surface. (D) Again, freely suspended colloids respond by migrating via diffusiophoresis (u_{DP}). This figure is an adaptation of Figure 5.2 in.[2]

External fields in the bulk can be expressed generally in terms of a gradient in the chemical potential $\nabla\mu_i^B$, such that the force on each ion within the EDL can be expressed as

$$F_i = -\nabla\mu_i^B. \tag{2.9}$$

This excess force acts on the surplus or deficit ions in the EDL, relative to the bulk, $\Delta n_i(x,z) = n_i(x,z) - n_i^B(x)$. The electrokinetic flow driven by this excess force can then be evaluated using the Stokes equation with a body force term,

$$0 = \eta\frac{\partial^2 u_x}{\partial z^2} - \sum_{i=1}^{N}\Delta n_i\frac{\partial\mu_i^B}{\partial x}. \tag{2.10}$$

Integrating Eq. 2.10 twice, gives

$$u_x^i(z) = \frac{1}{\eta}\frac{\partial\mu_i^B}{\partial x}\int_0^z\int_0^{z'}\Delta n_i(z'')dz''dz' = \frac{1}{\eta}\frac{\partial\mu_i^B}{\partial x}\int_0^z z'\Delta n_i(z')dz'. \tag{2.11}$$

Each ion's contribution to the slip velocity outside the EDL (at $z\to\infty$) can then be estimated from Eq. 2.11,

$$u_s^i = \frac{1}{\eta}\frac{\partial\mu_i^B}{\partial x}\int_0^\infty z'\Delta n_i(z')dz' = M_i\frac{\partial\mu_i^B}{\partial x}. \tag{2.12}$$

From the linearized Poisson-Boltzmann equation (Eq. 2.7), Eq. 2.12 can be evaluated exactly for the case of a monovalent, symmetric electrolyte, revealing

$$M_\pm = -\frac{\epsilon}{e\eta}\left(\mp\frac{\zeta}{2} + 2\frac{k_BT}{e}\ln\cosh\frac{e\zeta}{4k_BT}\right). \tag{2.13}$$

With this general expression for the slip mobility, $M_\pm$, we shall now explore the two

specific cases of electroosmosis/electrophoresis and diffusioosmosis/diffusiophoresis.

For electrophoresis, the applied external electric field (E_{app}) is related to the chemical potential as

$$\mu_{\pm}^{B} = \pm e\phi = \mp eE_{\text{app}}x, \tag{2.14}$$

so that $\nabla\mu_{\pm}^{B} = \mp eE_{\text{app}}$. From Eqs. 2.12 and 2.13, the electroosmotic slip velocity on a charged surface can then be expressed as

$$u_{\text{EOF}} = \sum_{i=1}^{2} M_i \nabla\mu_i^B = -\frac{\epsilon\zeta}{\eta}E_{\text{app}}, \tag{2.15}$$

which is also known as the Helmholtz-Smoluchowski equation. While Eq. 2.15 gives the slip velocity of the fluid on a fixed surface, a charged particle on the other hand responds to this fluid flow by migrating in the opposite direction. The force from the external field only acts on the EDL, and the particle double layer ensemble is completely force free from the perspective of the bulk fluid. The particle electrophoretic velocity is therefore equal and opposite to the electroosmotic slip velocity given by Eq. 2.15,

$$u_{\text{EP}} = \frac{\epsilon\zeta}{\eta}E_{\text{app}}. \tag{2.16}$$

Morrison later generalized this expression for the electrophoretic velocity for particles of any arbitrary shape.[3] Moreover, he showed that fluid disturbance due to phoretic motion decays like r^{-3}, much quicker than typical hydrodynamic interactions (e.g. those emerging from sedimenting particles) that decay like r^{-1}. Therefore, inter-particle interactions in most phoretic phenomena are typically ignored.

Diffusioosmotic flows in the double layer have two contributing factors. First, the concentration gradient of ions in the bulk creates an osmotic pressure gradient within

the EDL. Higher concentrations lead to higher pressures in the EDL and vice versa, causing the fluid to flow towards regions of lower ionic strength, or down the concentration gradient. This is defined as chemi-diffusioosmosis. Second, when the ions of an electrolyte have different diffusivities, they move through the bulk liquid at different rates. Overall electroneutrality however requires that the two ions migrate together (ambipolar diffusion), and thereby a spontaneous electric field is setup.[4,5] This field hastens the motion of the slower ion and retards the motion of the faster ion. Naturally, this electric field then drives a fluid flow through the EDL, defined as electro-diffusioosmosis.

The general expression for the chemical potential gradient in this case can be expressed as the sum of these two distinct fileds,

$$\nabla \mu_{\pm}^{B} = k_B T \frac{\nabla n_0^B}{n_0^B} \mp e E_{\text{ambi}}, \tag{2.17}$$

where we have used the electroneutrality condition, $\nabla n_+^B = \nabla n_-^B = \nabla n_0^B$, n_0^B is the bulk electrolyte concentration. The first term on the right hand side of Eq. 2.17 represents the osmotic pressure gradient, while the second term represents the electric field due to ambipolar diffusion of ions. This electric field can be obtained by balancing the flux of cations and anions in the bulk solution via the Nernst-Planck equation to give[6]

$$E_{\text{ambi}} = \beta \frac{k_B T}{e} \frac{\nabla n_0^B}{n_0^B}, \tag{2.18}$$

where the parameter β is defined by

$$\beta = \frac{D_+ - D_-}{D_+ + D_-}. \tag{2.19}$$

D_+ and D_- are the diffusion coefficients of the positive and negative ions, respectively. Plugging $\nabla \mu_{\pm}^B$ from Eq. 2.17 into Eq. 2.12 and using the slip mobility from 2.13 then

gives the diffusioosmotic slip velocity on a fixed surface[6–8]

$$u_{\mathrm{DOF}} = \sum_{i=1}^{2} M_i \nabla \mu_i^B = -\frac{\epsilon}{\eta}\frac{k_B T}{e}\left(\zeta\beta + \frac{4k_B T}{e}\ln\cosh\frac{e\zeta}{4k_B T}\right)\nabla \ln n_0^B. \tag{2.20}$$

As before, the free surface of a charged particle responds to the diffusioosmotic slip flow by migrating via diffusiophoresis, with velocity given by

$$u_{\mathrm{DP}} = \frac{\epsilon}{\eta}\frac{k_B T}{e}\left(\zeta\beta + \frac{4k_B T}{e}\ln\cosh\frac{e\zeta}{4k_B T}\right)\nabla \ln n_0^B. \tag{2.21}$$

The first term in Eq. 2.21 represents the electro-diffusiophoretic (EDP) contribution while the second term represents chemi-diffusiophoresis (CDP). EDP is proportional to both ζ and β and therefore particle motion emerging from just this contribution can be directed either up or down the concentration gradient, depending on the particle surface charge and diffusivity of the ions. On the other hand, the CDP contribution scales like $\cosh\zeta$ which is always positive, regardless of the surface charge. Thus, CDP is always directed up the concentration gradient. Ultimately, a balance between EDP and CDP decides the directionality of particle migration via diffusiophoresis. Another key feature of diffusiophoretic velocities is that they scale like $\nabla \ln n_0^B$ which means that even small gradients and small solute concentrations may drive strong, observable diffusiophoretic migration. We shall explore this feature in greater detail in Chapter 5.

The migration under non-electrolyte gradients is less well characterized and is believed to arise due to a non-uniform concentration of solute/solvent in the local environment around the particle, creating an excess or depletion region of solute/solvent at the particle interface. The bulk concentration gradient ∇c, applies an entropic force on this excess/depletion layer, which drives a 'solvoosmotic' slip flow along the surface of the colloid. This flow in turn causes a freely suspended colloidal particle to migrate

solvophoretically. The velocity of the colloidal particle in this case was first derived by Anderson and Prieve,[9]

$$u_{SP} = \frac{k_B T}{\eta} L^2 \nabla c \int_0^\infty y \left[\exp\left(\frac{-\phi(y)}{k_B T} \right) - 1 \right] dy. \tag{2.22}$$

This form of the velocity assumes a solute-surface interaction energy, given by ϕ, with the characteristic length scale over which this interaction occurs (i.e. the thickness of the excess/depletion layer) given by L.

2.3 Microfluidic platform to visualize and quantify diffusiophoretic migration

Although diffusiophoresis was first observed and reported by Derjaguin way back in 1947,[10] systematic measurements of the phenomenon were not made until very recently with the advent of microfluidics.[11,12] Since then, there has been a renewed interest in diffusiophoresis in areas ranging from membrane fouling,[13] to tranport into dead-end pores,[14,15] to water treatment,[16] to self propelling particles,[17–20] to active matter.[21–23]

The main difficulty in quantifying diffusiophoretic velocities that are typically on the order of a few microns per second, is establishing stable concentration gradients in the bulk, in a reliable and controllable fashion. Moreover, small convective drift velocities which are usually difficult to suppress in bulk suspensions could very easily interfere with the measurements.

The Squires group recently developed a microfluidic platform that enables chemical gradients to be directly imposed, and diffusiophoretic migration be visualized and measured under various solute and solvent gradients.[24] Figure 2.2A shows the three channel microfluidic device used for making the measurements. The three channels, labeled

I, II and III, are separated from each other by semi-permeable hydrogel membrane microwindows (HMMs) (Fig. 2.2B). These microwindows are permeable to solute and solvent diffusion and to electric fields, yet act as rigid walls from the standpoint of fluid flow. Channels I and III are maintained at high and low concentrations of solute, respectively. A gradient in solute concentration is thus established across channel II, where colloidal particles migrate diffusiophoretically under that gradient.

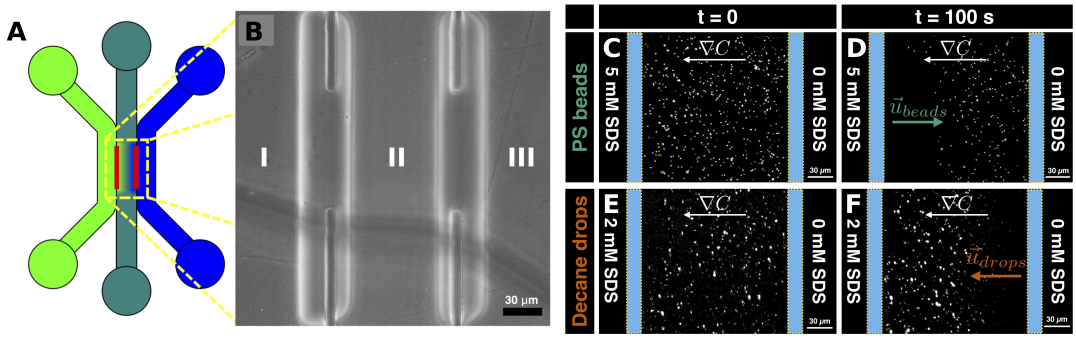

Figure 2.2: Visualization of diffusiophoretic migrations under chemical gradients. (A) Pictorial representation of the three channel microfluidic device used for visualizing and measuring diffusiophoretic migration. (B) The three channels are separated by semi-permeable hydrogel membrane microwindows. (C and D) PS colloids, initially uniformly distributed (C), migrate diffusiophoretically down SDS concentration gradients, as seen after 100 s (D). (E and F) By contrast, the DP of fluorescently-dyed decane drops is directed up SDS gradients. Parts (A) and (B) adapted from Paustian *et al*, *Langmuir*. 2015; 31: 4402–4410.[25]

The application of this microfluidic platform to study and visualize diffusiophoretic motion is shown in Fig. 2.2C-F, where high and low concentrations of sodium dodecyl-sulfate (SDS) flow through the outer 'reservoir' channels, to establish and maintain an SDS gradient of controllable strength across the central sample channel. Fluorescent, sulfonated polystyrene colloids (PS) move diffusiophoretically down SDS concentration gradients, consistent with electro-diffusiophoresis,[6,26] treating the (ionic) surfactant SDS as an electrolyte (Fig. 2.2C-D).[27] By contrast, decane drops migrate up SDS gradients, consistent with non-uniform SDS adsorption onto the droplet surface that either creates

surface tension gradients and thus 'soluto-capillary' migration,[28] or diffusiophoresis under strong adsorption[29] (Fig. 2.2E-F).

The microfluidic device described here provides a platform to routinely measure solute-particle interactions and diffusiophoretic mobility of different kinds of colloids under various chemical environments. In what follows, we shall use the knowledge obtained from these measurements to select the solute to drive the diffusiophoretic migration of particular colloids of interest.

Bibliography

[1] Russel W, Saville D, Schowalter W. *Colloidal Dispersions*. Cambridge Monographs on MechanicsCambridge University Press 1989.

[2] Squires TM. *Particles in Electric Fields*ch. 5, : 59-79. John Wiley & Sons, Ltd 2016.

[3] Morrison F. Electrophoresis of a particle of arbitrary shape. *Journal of Colloid and Interface Science.* 1970; 34(2): 210 - 214.

[4] Deen W. *Analysis of Transport Phenomena*. Topics in Chemical EngineeringOUP USA 1998.

[5] Cussler EL. *Diffusion: Mass Transfer in Fluid Systems*. Cambridge Series in Chemical EngineeringCambridge University Press3 ed. 2009.

[6] Prieve DC, Anderson JL, Ebel JP, Lowell ME. Motion of a particle generated by chemical gradients. Part 2. Electrolytes. *Journal of Fluid Mechanics.* 1984; 148: 247.

[7] Anderson JL. Colloid transport by interfacial forces. *Ann. Rev. Fluid Mech..* 1989; 21: 61–99.

[8] Anderson JL, Prieve DC. Diffusiophoresis: Migration of Colloidal Particles in Gradients of Solute Concentration. *Separation & Purification Reviews.* 1984; 13(1): 67–103.

[9] Anderson JL, Lowell ME, Prieve DC. Motion of a particle generated by chemical gradients Part 1. Non-electrolytes. *Journal of Fluid Mechanics.* 1982; 117: 107–121.

[10] Derjaguin B, Sidorenkov G, Zubashchenko E, Kiseleva E. Kinetic phenomena in the boundary layers of liquids 1. the capillary osmosis. *Kolloid. Zh..* 1947; 9(2): 335-347.

[11] Abécassis B, Cottin-Bizonne C, Ybert C, Ajdari a, Bocquet L. Boosting migration of large particles by solute contrasts. *Nature materials.* 2008; 7: 785–789.

[12] Palacci J, Cottin-Bizonne C, Ybert C, Bocquet L. Osmotic traps for colloids and macromolecules based on logarithmic sensing in salt taxis. *Soft Matter.* 2012; 8(1): 980.

[13] Kar A, Guha R, Dani N, Velegol D, Kumar M. Particle deposition on microporous membranes can be enhanced or reduced by salt gradients. *Langmuir.* 2014; 30(3): 793–799.

[14] Kar A, Chiang TY, Ortiz Rivera I, Sen A, Velegol D. Enhanced transport into and out of dead-end pores. *ACS nano.* 2015; 9(1): 746–53.

[15] Shin S, Um E, Sabass B, Ault JT, Rahimi M, Warren PB. Size-dependent control of colloid transport via solute gradients in dead-end channels. *Proceedings of the National Academy of Sciences.* 2016; 113(2): 257-261.

[16] Shin S, Shardt O, Warren PB, Stone HA. Membraneless water filtration using CO 2. *Nature Communications.* 2017; 8(May): 1–6.

[17] Kline TR, Paxton WF, Mallouk TE, Sen A. Catalytic Nanomotors: Remote-Controlled Autonomous Movement of Striped Metallic Nanorods. *Angewandte Chemie.* 2005; 117(5): 754–756.

[18] Moran JL, Posner JD. Electrokinetic locomotion due to reaction-induced charge auto-electrophoresis. *Journal of Fluid Mechanics.* 2011; 680: 31–66.

[19] Brady JF. Particle motion driven by solute gradients with application to autonomous motion: continuum and colloidal perspectives. *Journal of Fluid Mechanics.* 2011; 667: 216–259.

[20] Golestanian R, Liverpool TB, Ajdari A. Propulsion of a molecular machine by asymmetric distribution of reaction products. *Physical Review Letters.* 2005; 94(22): 1–4.

[21] Ibele M, Mallouk TE, Sen A. Schooling behavior of light-powered autonomous micromotors in water. *Angewandte Chemie - International Edition.* 2009; 48(18): 3308–3312.

[22] Theurkauff I, Cottin-Bizonne C, Palacci J, Ybert C, Bocquet L. Dynamic clustering in active colloidal suspensions with chemical signaling. *Physical Review Letters.* 2012; 108(June): 1–5.

[23] Buttinoni I, Volpe G, Kümmel F, Volpe G, Bechinger C. Active Brownian motion tunable by light. *Journal of Physics: Condensed Matter.* 2012; 24: 284129.

[24] Paustian JS, Azevedo RN, Lundin STB, Gilkey MJ, Squires TM. Microfluidic microdialysis: Spatiotemporal control over solution microenvironments using integrated hydrogel membrane microwindows. *Physical Review X.* 2014; 3: 1–13.

[25] Paustian JS, Angulo CD, Nery-Azevedo R, Shi N, Abdel-Fattah AI, Squires TM. Direct Measurements of Colloidal Solvophoresis under Imposed Solvent and Solute Gradients. *Langmuir.* 2015; 31: 4402–4410.

[26] Derjaguin BV, Dukhin SS, Korotkova AA. Diffusiophoresis in electrolyte solutions and its role in the Mechanism of the formation of films from caoutchouc latexes by the ionic deposition method. *Progress in Surface Science.* 1993; 43(20): 153–158.

[27] Nery-Azevedo R, Banerjee A, Squires TM. Diffusiophoresis in Ionic Surfactant Gradients. *Langmuir.* 2017(1).

[28] Levich BG, Kuznetsov AM. On the motion of drops in liquids under the action of surface active substances. *Dokl. Acad. Nauk SSSR.* 1962; 146: 145–147.

[29] Anderson JL, Prieve DC. Diffusiophoresis Caused by Gradients of Strongly Adsorbing Solutes. *Langmuir.* 1981; 7: 403–406.

Chapter 3

Soluto-inertial suspension interactions

Diffusiophoresis (DP) is a non-equilibrium phenomenon, thus, particles migrate so long as gradient in the solute concentration exists. Therefore, to ensure sustained interactions, solute fluxes must be long lasting. Here, we introduce the concept of solute-inertia that enables solute gradients to evolve over extended periods of time. Solute-inertia refers to the degree of slowness with which the concentration of solute in a material approaches that of it's surrounding. The concept is analogous to thermal-inertia in heat transport, wherein materials with high volumetric heat capacity in poor heat transfer media resist changes in temperature and thus, maintain long-lasting heat flux. Similarly in mass transport, materials that impart solute-inertia can maintain concentration gradients over long periods of time, causing colloidal particles that sense that gradient to migrate via DP. We refer to such soluto-inertial (SI) materials as "chemical beacons", depicted by the grey circle in Fig. 3.1.

This chapter is adapted from Banerjee *et al., Proceedings of the National Academy of Sciences USA.* 2016; 113(31): 8612-8617.[1]

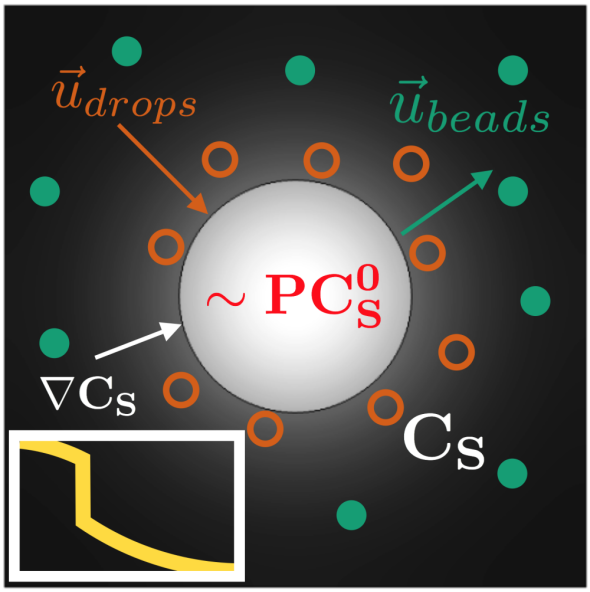

Figure 3.1: Long-range soluto-inertial (SI) interactions. An SI beacon (gray), initially loaded with a high solute concentration, is placed in a solute-free suspension. A solute out-flux is established during equilibration, driving nearby suspended particles into diffusiophoretic migration. The magnitude and direction of migration depends on interactions between the particle surface and the solute, depicted here by particles of different surface chemistries (orange and green) that migrate either up or down the solute gradient. Inset: schematic radial profile of solute concentration inside and outside of the beacon.

Our proposed mechanism for long-range and long-lasting interactions in suspensions, requires three key ingredients. First, a particle or structure must act as a beacon that generates a long-lasting solute flux. Second are the suspended objects (*e.g.* colloidal particles, polymers, or emulsion drops), which may be attracted or repelled from the beacon. Third is the solute whose flux mediates the interaction by driving suspended objects into diffusiophoretic migration. Careful choice of these three ingredients (beacon, solute and suspended particle) enables the duration, direction and range of the beacon-suspension interactions to be designed and engineered.

SI beacons can be made from materials that strongly partition the solute, so that solute within the beacon (C_B) equilibrates at a concentration that exceeds the concentration

in the neighboring solution (C_S) by a large partition coefficient P, giving $C_B = PC_S$, where $P \gg 1$.[2] With such a choice, a beacon 'loaded' with solute that is placed in a solute-free suspension equilibrates over long time scales, as demonstrated and described in the following section, ensuring a long-lived solute out-flux (and thus SI interaction). Therefore, the key physico-chemical property required of the SI beacon is that it strongly partitions whatever solute has been selected to attract or repel the colloids of interest. Other strategies to choose beacon materials that maximize solute unloading time in solution are discussed in Chapter 5.

3.1 Proof of principle

Whether the beacon attracts or repels colloids in suspension depends on how those colloids migrate under the chosen solute flux. Figure 2.2 shows oppositely directed motion of decane drops and polystyrene (PS) particles under an SDS flux, suggesting that an SI beacon designed to emit SDS should attract decane droplets, but repel PS particles. SDS is known to associate with polyethylene glycol (PEG),[3,4] further suggesting that PEG hydrogels will strongly partition SDS, and thus function as SI beacons. Figure 3.2 shows a cylindrical SI beacon of radius $R \approx 200$ μm created by photo-polymerizing a PEG-diacrylate (PEG-DA) precursor solution *in situ* within a microfluidic "stickers"[5] device (Fig. 3.2) by exposure to masked, ultra-violet light (similar to the procedure followed in[6–8]), then flushing unreacted precursor from the device.

The experimental procedure is shown schematically in Fig. 3.3. An SI beacon is initially loaded by immersion in a 5 mM SDS solution (Fig. 3.3A). The SDS 'loading' solution is then flushed by flowing in a suspension of colloids and/or drops (Fig. 3.3B). The SDS that had partitioned into the SI beacon is no longer in equilibrium with the surrounding solution, and therefore diffuses out of the SI beacon to equilibrate. The

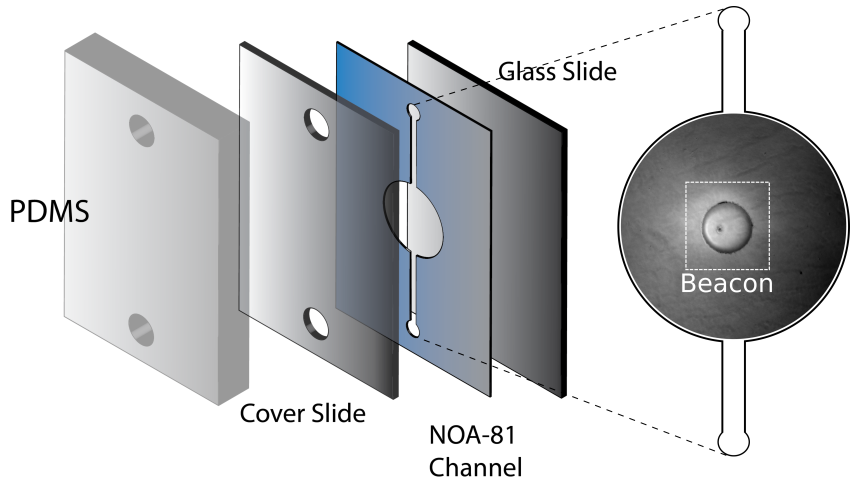

Figure 3.2: Platform to visualize and observe the SI phenomena. Microfluidic device used for demonstrating the SI phenomena, with the PEG-DA beacon photo-polymerized at the center.

resulting SDS concentration gradient persists as long as SDS out-fluxes from the SI beacon (Fig. 3.3C), within which suspended colloids and/or drops migrate diffusiophoretically.

Figure 3.3D-E reveals this system to behave as predicted: PEG-DA beacons partition SDS, and therefore establish a long-lived, long-ranged SDS flux that effectively repels PS colloids, but attracts decane drops. In particular, PS particles are repelled from the SI beacon (down the SDS gradient), forming a $300 - 400$ μm-thick particle-free region around the beacon (Fig. 3.3D). PS particle migration is evident for at least 1000 seconds, by which time most of the particles have migrated out of the microscope field of view. The particle surface-specificity of SI interactions is verified by following the same procedure, but introducing decane droplets instead of PS colloids. As expected, decane droplets experience a long-range, long-lasting SI attraction towards the beacon, moving up the imposed SDS gradient as shown by the streak lines in Fig. 3.3E The range and duration in this case is comparable to that observed with PS particles. Notably, the SI interaction range (here $100 - 1000$ μm) is 10^3-10^4 times larger than the Debye screening length that limits the electrostatic interaction.

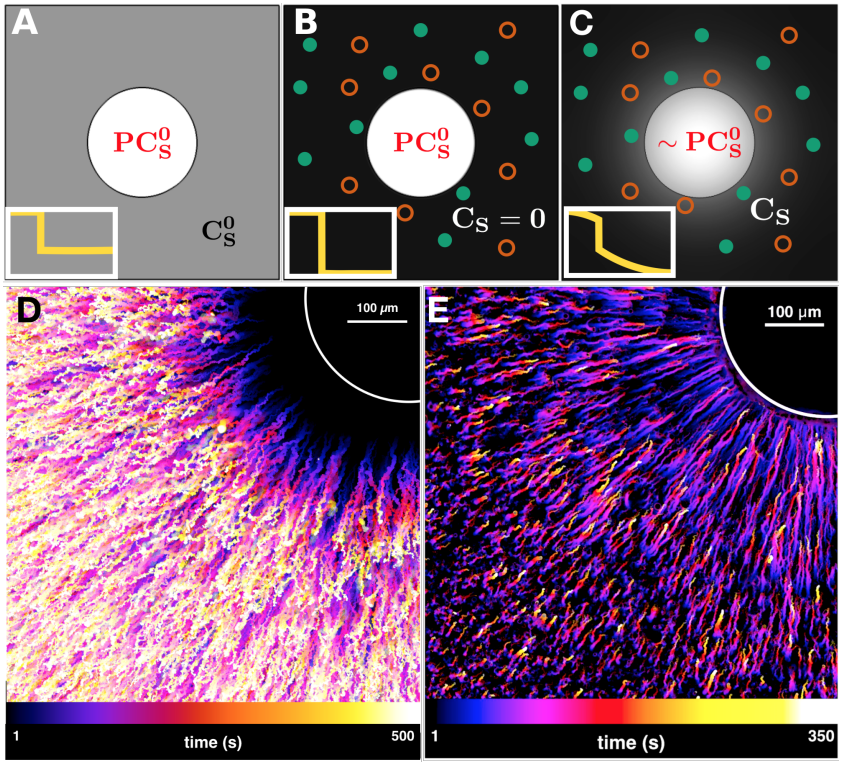

Figure 3.3: Experimental demonstration of the SI phenomena. (A) Loading beacon with solute. (B) Flushing loading solution. (C) Slow equilibration of stored solute into particle suspension. Insets show radial concentration profiles throughout the experiment. (D) Time-stamped streak lines of PS particle migration in first 500 s of experiment, directed *away* from the SI beacon and (E) decane droplet migration in first 350 s of experiment, directed *towards* the SI beacon.

3.2 SI model

Having shown that the SI effect can be exploited to generate and direct diffusiophoretic motion in suspensions, we now develop a simple model of this behavior, focusing initially on spherical SI beacons to avoid the mathematical subtleties of 2D diffusion. Other models that capture the nuances of coupled mass transport processes in the beacon and solution phases are discussed in detail in Chapter 5.

A spherical SI beacon is initially loaded by immersion in a loading solution of concentration C_S^0, and thus equilibrates with some beacon concentration $C_B^0 = PC_S^0$. When

suspended in a solute-free environment ($C_S = 0$), the solute in the beacon $C_B(t)$ diffuses out into the surrounding solution. We assume that the solute concentration within the beacon evolves rapidly enough that intra-beacon concentration gradients can be neglected [$C_B(r,t) \approx C_B(t)$], and that the concentration within the beacon $C_B(t)$ changes on time scales much slower than are required for $C_S(r,t)$ to evolve. Under these quasi-steady assumptions, the concentration field around a spherical, SI beacon of radius R which partitions solute with a partition coefficient P obeys

$$C_S(r,t) = \frac{C_B(t)}{P}\frac{R}{r}. \tag{3.1}$$

This concentration field gives rise to a diffusion-limited solute flux $J = 4\pi DRC_B(t)/P$ out of the beacon, where D is the diffusion coefficient of the solute. This out-flux must equal the rate at which solute molecules are lost from the beacon,

$$J = \frac{4\pi DRC_B(t)}{P} = -\frac{d}{dt}\left[\frac{4\pi R^3}{3}C_B(t)\right], \tag{3.2}$$

which can be solved to give the beacon concentration

$$C_B(t) = C_B^0 \exp^{-\frac{3D}{PR^2}t}, \tag{3.3}$$

Eqn. 3.3 reveals a natural SI time scale,

$$\tau_{SI} = P\frac{R^2}{3D}, \tag{3.4}$$

over which SI beacons emit solute, which exceeds the diffusion time scale $\tau_D = \frac{R^2}{D}$ by the partition coefficient P, and may thus be many orders of magnitude longer when $P \gg 1$.

We further investigate the range over which colloidal particles migrate diffusiophoreti-

cally under the concentration gradient set by the SI beacon. Diffusiophoretic migration velocities under electrolyte gradients are predicted[9,10] to obey

$$u_{DP} = D_{DP} \nabla \ln C_S \tag{3.5}$$

where D_{DP} is the diffusiophoretic mobility of the particle, whose magnitude and sign both depend on the surface chemistry of the particle and solute (Eq. 2.21). Using Eq. 3.5 for the quasi-steady concentration field around a spherical SI beacon (Eq. 3.1), reveals colloids to migrate under a quasi-steady SI out-flux with velocity

$$u_{DP}(r) = -\frac{D_{DP}}{r}, \tag{3.6}$$

decaying with distance like r^{-1}. Several features are notable: the SI migration velocity (i) is independent of $C_B(t)$, the instantaneous concentration of solute in the beacon, (ii) decays slowly with distance from the SI beacon, and (iii) is particle surface-specific, as determined by D_{DP}.

3.3 Quantitative measurements of migration velocity

Individual particle trajectories can be extracted from micrograph series, allowing particle velocities to be measured directly in space and time (using algorithms adapted from[11] and techniques described in[12]). Figure 3.6 shows raw (inset) and scaled velocity profiles at different times, around cylindrical SI beacons of two different radii (R_P = 130 μm and 200 μm).

No steady-state concentration profile exists for 2D structures like the SI beacons shown

in Fig. 3.2. We therefore solve the transient mass transport problem analytically and numerically using COMSOL Multiphysics®, under the same quasi-steady assumptions described in Section 3.2. Concentration fields $C_S(r,t)$ in bulk solution evolve much more rapidly than in the SI beacon, and so we impose a quasi-steady boundary condition $C_B(t)$. The validity of this assumption is illustrated in Fig. 3.4 which shows good agrrement between the full solution to the mass transport equations (Fig. 3.4A) and the approximate quasi-steady evolution (Fig. 3.4B). Moreover, if $P \gg 1$, the boundary condition at the beacon-solution interface at short times can simply be approximated as a constant, $C_B(t) \sim C_0$, shown by Fig. 3.4C. As seen in Figs. 3.4D-F, diffusiophoretic velocity profiles obtained in all three cases, Fig. 3.4D fully transient vs Fig. 3.4E quasi-steady vs Fig. 3.4F constant boundary condition, are nearly identical. Since the values of solute diffusivity in the beacon phase and P are not known a priori for our system, and because PEG- DA strongly partitions SDS (P is large), we simply impose a fixed boundary condition at the beacon surface to obtain analytical expressions for the solute concentration profile in solution.

Guided by the scaling arguments for spherical SI beacons, we scale distance by the beacon radius R_P, time by the diffusion time R_P^2/D_{SDS} of dissolved SDS, and concentrations by a concentration scale C_0. In cylindrical coordinates, the non-dimensionalized diffusive mass transport equation in the radial direction is given by

$$\frac{\partial \tilde{C}}{\partial \tilde{t}} = \frac{1}{\tilde{r}} \frac{\partial}{\partial \tilde{r}} \left(\tilde{r} \frac{\partial \tilde{C}}{\partial \tilde{r}} \right), \tag{3.7}$$

where $C_S = C_0 \tilde{C}$, $r = R_P \tilde{r}$ and $t = (R_P^2/D_{SDS})\tilde{t}$. The diffusion coefficient D_{SDS} of aqueous SDS below the critical micelle concentration is taken as 780 μm^2/s.[13] The concentration field $\tilde{C}(\tilde{r},\tilde{t})$ is then computed by enforcing $\tilde{C}(\tilde{r}=1,\tilde{t}) = 1$ and $d\tilde{C}/d\tilde{r}(\tilde{r} \rightarrow$

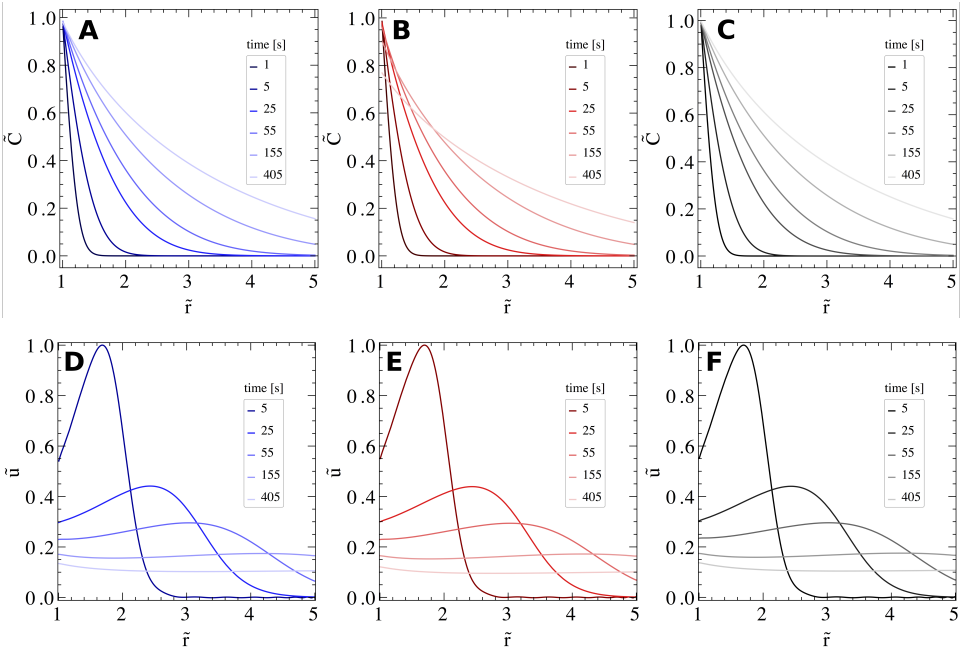

Figure 3.4: Validity of the quasi-steady state assumption. Time evolution of the concentration profile of SDS in solution, corresponding to different boundary conditions at the beacon - solution interface. (A) Boundary concentration is calculated by solving coupled mass transport equations inside and outside the beacon, with $D_B = 30\ \mu\text{m}^2/\text{s}$ and $P = 30$. (B) Concentration at boundary is assumed to decay exponentially with decay constant $= D_{SDS}/PR_P^2$. (C) Fixed boundary condition is imposed at the interface. (D-F) Velocity profiles corresponding to the concentration profiles depicted in (A-C), respectively.

$\infty, \tilde{t}) \to 0$. The analytical solution to Eq. 3.7 with these boundary conditions

$$C_S(r,t) = C_0 + \sum_n \beta_n \left[-\frac{Y_0(\lambda_n R_P)}{J_0(\lambda_n R_P)} J_0(\lambda_n r) + Y_0(\lambda_n r) \right] \exp^{-\lambda_n^2 D_{SDS} t}, \tag{3.8}$$

is in good agreement with the numerical model (Fig. 3.5). Here,

$$\beta_n = \frac{\int_{R_P}^{R_\infty} r S_0(\lambda_n r)(C_i - C_0) dr}{\int_{R_P}^{R_\infty} r S_0(\lambda_n r) S_0(\lambda_n r) dr}, \tag{3.9}$$

with

$$S_0(\lambda_n r) = Y_0(\lambda_n r) - \frac{Y_0(\lambda_n R_P)}{J_0(\lambda_n R_P)} J_0(\lambda_n r). \tag{3.10}$$

J_0 and Y_0 are 0 order Bessel functions of the first and the second kind, respectively, and λ_n are roots of the equation

$$Y_0(\lambda R_P) J_1(\lambda R_\infty) - J_0(\lambda R_P) Y_1(\lambda R_\infty) = 0, \tag{3.11}$$

where J_1 and Y_1 are 1st order Bessel functions of the first and the second kind, respectively.

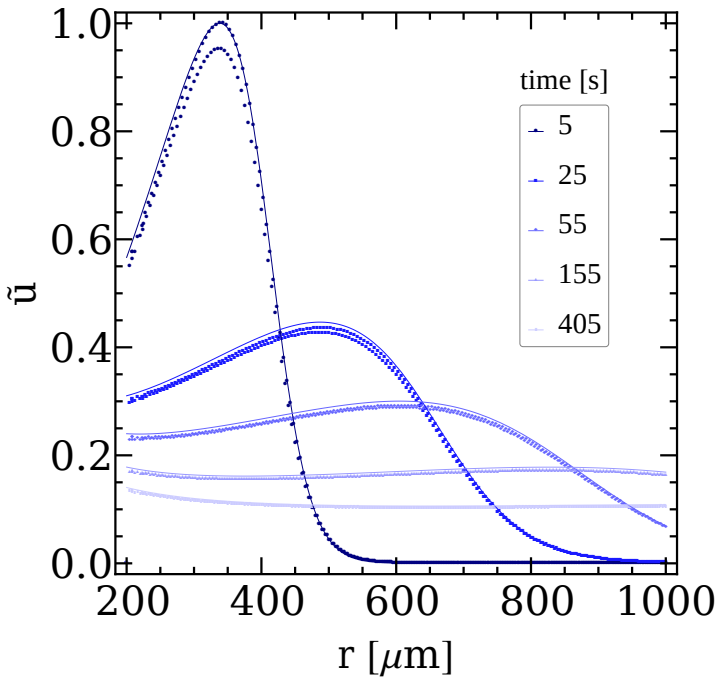

Figure 3.5: Analytical vs numerical model for SI transport. Comparison between the numerical and analytical solutions corresponding to $R_P = 200$ μm and $R_\infty = 2000$ μm. The smooth curves represent the analytical solution found by computing the first 100 terms of the Fourier series given by Eqn. 3.8, while the points represent the numerical solution. The comparison is demonstrated for five time steps, represented by different colors, as indicated in the legend.

The DP migration velocities of suspended particles can then be computed at any position and time from $\tilde{C}(\tilde{r},\tilde{t})$ using Eqn. 3.5, and are simply proportional to $\nabla \ln \tilde{C}(\tilde{r},\tilde{t})$. The diffusiophoretic mobility D_{DP} of PS particles under SDS gradients is not known *a priori*. To compare the measured and calculated SI migration velocities, we normalize all measured or calculated velocities by a single value, corresponding to the maximum value that was measured or calculated,

$$\tilde{u} = \frac{u}{u_{\max}} = \frac{\nabla \ln C_S}{\max |\nabla \ln C_S|}. \tag{3.12}$$

So long as D_{DP} is constant, normalizing velocities in this way enables direct comparisons between measured and calculated velocity profiles at different times, irrespective of the single (unknown) parameter D_{DP}.

Figure 3.6 shows the non-dimensional radial velocity profiles of PS colloids measured in experiments with SI beacons of radii $R_P = 200$ μm (filled blue points) and $R_P = 130$ μm (empty red points). Each differently colored set of data corresponds to a finite time window, and depict the time evolution of the measured velocity profile around the beacon. Appropriate non-dimensionalization allows the experimental data to be compared to the SI model, the predictions from which are plotted as solid lines corresponding to each of the experimental time intervals shown. When properly scaled according to the SI arguments presented above, measured velocity profiles show excellent agreement, in space and time, not only between the two different-sized SI beacons, but also between the experimental measurements and the SI model predictions. This collapse justifies our choice of the length, time and velocity scales as well as confirms that the mass transport model coupled with the quasi-steady state assumption captures the observed SI migration phenomenon quantitatively. It should be noted that while the velocity profile appears increasingly flat as time progresses, it remains non-zero in both the SI model and in experiment. The

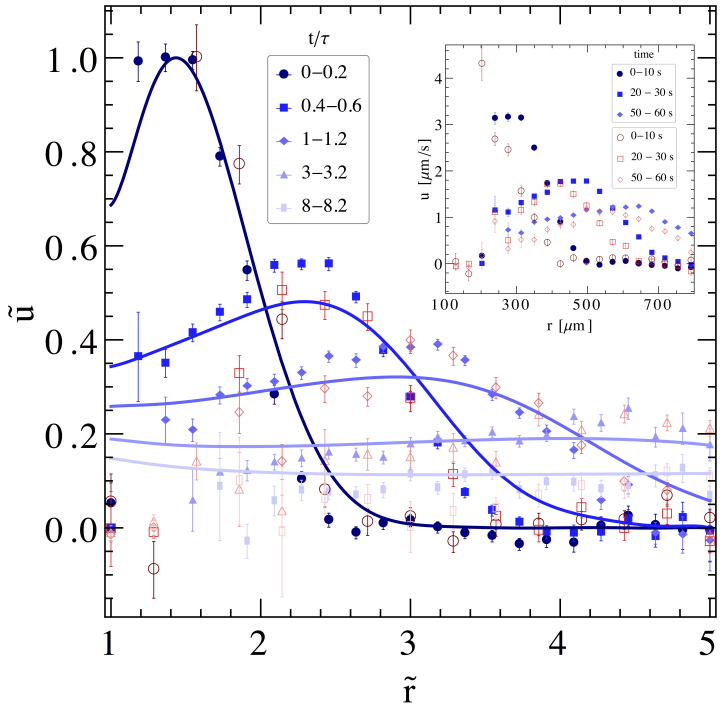

Figure 3.6: Quantitative measurements of SI migration velocities. Radial SI velocity profiles for PS colloids migrating around cylindrical SI beacons of radii $R_P = 130$ μm (open red symbols) and 200 μm (filled blue symbols), at different times. Points represent data measured in experiment, with unscaled data shown in the inset. Scaling distance by post radii R_P, velocities by the maximum velocity $u_{\max}$ measured at any place and time in each experiment, and time by the radial diffusion time R_P^2/D_{SDS} collapses measured data for both posts onto the profiles computed from the quasi-steady mass transport model. Measured and computed velocity profiles at different (scaled) times are represented with different colors, with corresponding t/τ values indicated in the key.

success of the scalings for the SI time scale (Eq. 3.3) and distance scale R_P, along with the quantitative agreement between theory and experiment in Fig. 3.6, underscores the quantitative capability to design a long-range, long-lasting suspension interaction.

3.4 Conclusion

The general SI strategy described here shares many features in common with previous observations involving DP, specifically involving reacting or dissolving interfaces. Derjaguin elucidated the existence and influence of DP on latex film formation onto salt-soaked surfaces.[9] Prieve and co-workers noted an analogy with chemically-reacting systems, *e.g.* as steel dissolution drives the diffusiophoretically-accelerated deposition of latex particles.[14] More recently, McDermott *et al.* showed that calcium carbonate particles dissolving in unsaturated aqueous solutions act as diffusioosmotic micropumps, driving flows along neighboring surfaces.[15] Zheng and Pollack[16] reported long-range exclusion near hydrogel boundaries, and Florea *et al.*[17] revealed ion exchange reactions to form a colloidal exclusion zone near membrane surfaces.

We have established a conceptual framework for the design and engineering of long-ranged, non-equilibrium colloidal interactions in suspension, whose magnitude and direction depends on the surface chemistry of the suspended particles. Our results highlight the versatility and generality enabled by combining the slow, SI release of solute, with the diffusiophoretic migration of suspended particles. The direction and speed of suspended particle migration can be controlled by appropriate choice of solute, and the range and duration of the SI interaction can be tuned by choosing size and material of the SI beacon to maximize the partition coefficient. With this specific PEG-DA (beacon) - SDS (solute) system, we have revealed SI interactions to last for tens of minutes, and extend over hundreds of microns. Moreover, fairly simple scaling arguments and numerical computations capture the quantitative and qualitative characteristics of SI interactions. The results and conclusions from this study are also profiled in.[18]

3.5 Materials and Methods

3.5.1 Device Fabrication

A single inlet/outlet microfluidic device is used, with a large central circular chamber (Fig. 3). A computer controlled laser cutter (Trotec Speedy 100) cuts the channel into 60 μm-thick scotch tape. The cut tape is then stuck to a petri dish, which is used as a master for making a PDMS replica of the design. The PDMS master is used to fabricate the device in "microfluidic stickers" (NOA - 81, Norland Adhesive).[5] The central chamber has a radius of 2 mm while the inlet and outlet channels are 500 μm wide. A glass cover slide is used to seal the device, with holes drilled to provide access for inlet and outlet tubing. A PDMS inlet is ozone bonded to the cover slide to provide support for inlet and outlet pins and tubings. The device is then baked at 80^o C for at least 4 hours to strengthen bonding.

3.5.2 Sample Preparations

Sodium dodecylsulfate (SDS) solutions are prepared by diluting a 10 mM SDS (Sigma Aldrich) stock solution in deionized water. PEG-DA precursor solution is prepared by mixing 33%(v/v) PEG(700)-DA (Sigma-Aldrich) with 4%(v/v) photoinitiator (2-hydroxy-2-methylpropiophenone, Sigma-Aldrich) in deionized water. 0.25% v/v fluorescent PS beads, 1 μm diameter (Bangs Laboratories FS03F) are suspended in clear de-ionized water to form the PS suspension. The decane emulsion is prepared by first adding 0.5% v/v fluorescent yellow 131SC dye (Keystone) to decane (Sigma Aldrich). 1% v/v of the dyed decane is vortexed for 30 s with a 1 mM SDS solution (in DI water) and then sonicated for 15 s to create 1–2 μm decane droplets in water.

3.5.3 Experimental Setup

PEG-DA gels are used as SI structures and fabricated using the microscope projection lithography technique.[6,19] A UV lamp is set to 30 mW/cm^2 (measured at an empty objective slot). A 1000 μm diameter circular photomask is inserted into the microscope and aligned as described previously.[7] PEG-DA precursor solution is injected until the channel is filled. The syringe is disconnected and 2 minutes are allowed for flow to relax. 500 ms ultraviolet exposure is used with a 10x objective to photopolymerize the gel. The precursor solution is flushed from the device by flowing DI water for 30 minutes. This results in hydrogel posts of diameter of 375–425 μm (Figure 3). Different sizes of posts are obtained by changing the size of the photomask, the exposure time and the objective magnification.

Experiments are performed using an inverted microscope (Nikon TE2000U). The hydrogel SI structure is initially loaded with a fixed concentration (5 mM) of SDS, by maintaining flow in the channel for 20 minutes. SDS solution is then flushed out by displacing with the suspension of PS particles or decane drops. The inlet is pressurized to 500 mbar and the channel is flushed for 5 seconds before reducing the pressure to 20 mbar. The focus is adjusted to the center of the channel using a 10x objective. Video recording is started (Andor iXon 885 fluorescence camera) and flow in the channel is stopped using the technique described in.[20] In each experiment, images are recorded for 1000 seconds at 1 frame per second, with 0.1 s exposure times.

3.5.4 Data Analysis

Two dimensional particle trajectories are extracted from the fluorescence micrograph series using algorithms adapted from those of Crocker and Grier[11] and implemented in the R programming language, previously employed for analysis of brightfield micrographs.[12]

For each image series a background image was calculated by finding the time-averaged brightness for each pixel. This background was subtracted from each image in the series. Images were further processed with a spatial bandpass filter and a local background subtraction to eliminate pixel noise and long wavelength brightness fluctuations. This processing has the added benefit of removing out-of-focus particle images, allowing the analysis to focus on particles in the microscope's focal plane. Local brightness maxima are identified as candidate particle positions, and a brightness-weighted centroiding over the particle diameter is performed to obtain particle co-ordinates with subpixel precision. Finally, trajectories are obtained by linking particle positions between frames in the acquired videos.

The PS particles explore all three dimensions on the timescale of the experiments. However, due to the axisymmetry of the concentration gradient, two-dimensional tracking in the x–y plane is sufficient to observe and explore the diffusiophoretic particle motion. Instantaneous particle velocities in the radial direction are obtained from frame-to-frame displacements and velocity profiles are calculated by averaging the velocities within annular regions of width 50 pixels with the origin fixed at the centre of the beacon. The concentration profile evolves with time and therefore, so does the velocity profile, and as such velocity profiles are calculated independently over 4.5 second (for $R_P = 130$ μm) and 10 second (for $R_P = 200$ μm) intervals throughout the experiment. Splitting the experiment into chunks in this way provides more samples in each annular bin, improving the statistics of averaging and suppressing noise in the velocity profiles.

Acknowledgements

Ian Williams, Rodrigo Nery Azevedo, and Matt Helgeson are co-authors on this work. We acknowledge the American Chemical Society Petroleum Research Foundation (Grant

54141-ND5) for primary support of this work. We would also like to thank support from the National Institutes of Health (Grant HL-51177), the Institute for Collaborative Biotechnologies (Grant W911NF-09-0001) from the US Army Research Office, and the National Science Foundation (NSF Grant CBET-1438779). Work was performed in the University of California Santa Barbara (UCSB) Materials Research Laboratory Central Facilities, a member of the NSF-funded Materials Research Facilities Network, which is supported by the NSF Materials Research Science and Engineering Centers Program under Grant DMR 1121053, and in the UCSB Nanofabrication Facility, a member of the NSF-funded National Nanotechnology Infrastructure Network.

Bibliography

[1] Banerjee A, Williams I, Azevedo RN, Helgeson ME, Squires TM. Soluto-inertial phenomena: Designing long-range, long-lasting, surface-specific interactions in suspensions. *Proceedings of the National Academy of Sciences.* 2016; 113(31): 8612-8617.

[2] Leo A, Hansch C, Elkins D. Partition coefficients and their uses. *Chemical Reviews.* 1971; 71(6): 525.

[3] Tam KC, Wyn-Jones E. Insights on polymer surfactant complex structures during the binding of surfactants to polymers as measured by equilibrium and structural techniques. *Chemical Society reviews.* 2006; 35(8): 693–709.

[4] Kim J, Gao Y, Hebebrand C, Peirtsegaele E, Helgeson ME. Polymer-surfactant complexation as a generic route to responsive viscoelastic nanoemulsions. *Soft Matter.* 2013; 9: 6897-6910.

[5] Bartolo D, Degré G, Nghe P, Studer V. Microfluidic stickers. *Lab on a Chip.* 2008; 8: 274–279.

[6] Dendukuri D, Gu SS, Pregibon DC, Hatton TA, Doyle PS. Stop-flow lithography in a microfluidic device. *Lab on a Chip.* 2007; 7(7): 818–828.

[7] Paustian JS, Azevedo RN, Lundin STB, Gilkey MJ, Squires TM. Microfluidic microdialysis: Spatiotemporal control over solution microenvironments using integrated hydrogel membrane microwindows. *Physical Review X.* 2014; 3: 1–13.

[8] Helgeson ME, Chapin SC, Doyle PS. Hydrogel microparticles from lithographic processes: Novel materials for fundamental and applied colloid science. *Curr. Opin. Colloid Interf. Sci.* 2011; 16(2): 106–117.

[9] Derjaguin BV, Dukhin SS, Korotkova AA. Diffusiophoresis in electrolyte solutions and its role in the Mechanism of the formation of films from caoutchouc latexes by the ionic deposition method. *Progress in Surface Science.* 1993; 43(20): 153–158.

[10] Anderson JL, Lowell ME, Prieve DC. Motion of a particle generated by chemical gradients Part 1. Non-electrolytes. *Journal of Fluid Mechanics.* 1982; 117: 107–121.

[11] Crocker JC, Grier DG. Methods of Digital Video Microscopy for Colloidal Studies. *Journal of Colloid and Interface Science.* 1996; 179: 298–310.

[12] Gray AT, Mould E, Royall CP, Williams I. Structural characterisation of polycrystalline colloidal monolayers in the presence of aspherical impurities. *Journal of Physics: Condensed Matter.* 2015; 27: 194108.

[13] Leaist DO. Binary diffusion of micellar electrolytes. *Journal of Colloid and Interface Science.* 1986; 111(1): 230–239.

[14] Prieve DC. Migration of a colloidal particle in a gradient of electrolyte concentration. *Advances in Colloid and Interface Science.* 1982; 16: 321–335.

[15] McDermott JJ, Kar A, Daher M, et al. Self-generated diffusioosmotic flows from calcium carbonate micropumps. *Langmuir.* 2012; 28: 15491–15497.

[16] Zheng Jm, Pollack GH. Long-range forces extending from polymer-gel surfaces. *Physical Review E.* 2003; 68: 031408.

[17] Florea D, Musa S, Huyghe JMR, Wyss HM. Long-range repulsion of colloids driven by ion exchange and diffusiophoresis. *Proceedings of the National Academy of Sciences of the United States of America.* 2014; 111(18): 6554–9.

[18] Zwanikken JW. Steering colloidal particles over millimeter distances with soluto-inertial beacons. *Proceedings of the National Academy of Sciences.* 2016; 113(31): 8565–8567.

[19] Love JC, Wolfe DB, Jacobs HO, Whitesides GM. Microscope projection photolithography for rapid prototyping of masters with micron-scale features for use in soft lithography. *Langmuir.* 2001; 17(19): 6005–6012.

[20] Paustian JS, Angulo CD, Nery-Azevedo R, Shi N, Abdel-Fattah AI, Squires TM. Direct Measurements of Colloidal Solvophoresis under Imposed Solvent and Solute Gradients. *Langmuir.* 2015; 31: 4402–4410.

Chapter 4

Triggering and combining soluto-inertial beacons

We now highlight the versatility of the soluto-inertial (SI) concept, demonstrating suspension interactions mediated by beacons with a variety of qualitatively distinct physico-chemical properties. Figure 4.1 depicts the new SI strategies explored here. In particular, we first describe a class of thermo-responsive beacons that can be actuated with temperature as a trigger to release trapped solute and initiate diffusiophoretic (DP) migration in neighboring particles (Fig. 4.1B-1, B-2). Next, we combine distinct beacons and introduce SI dipole interactions where a beacon "source" releases solute which is absorbed by a beacon "sink". This dipolar flux directs particle motion to propagate along well defined trajectories as depicted in Fig. 4.1C. Alternatively, multiple beacon sources, each emitting different solute provide new mechanisms to separate colloidal mixtures (Fig. 4.1D). A final variant on the multi-source beacon strategy involves SI beacons that release solutes that react with each other (Fig. 4.1E). We show that this reaction results in faster, longer-lasting SI migration, and enables targeting colloids to 'focus' at

This chapter is adapted from Banerjee, Squires *Science Advances.* 2019; accepted - in press.

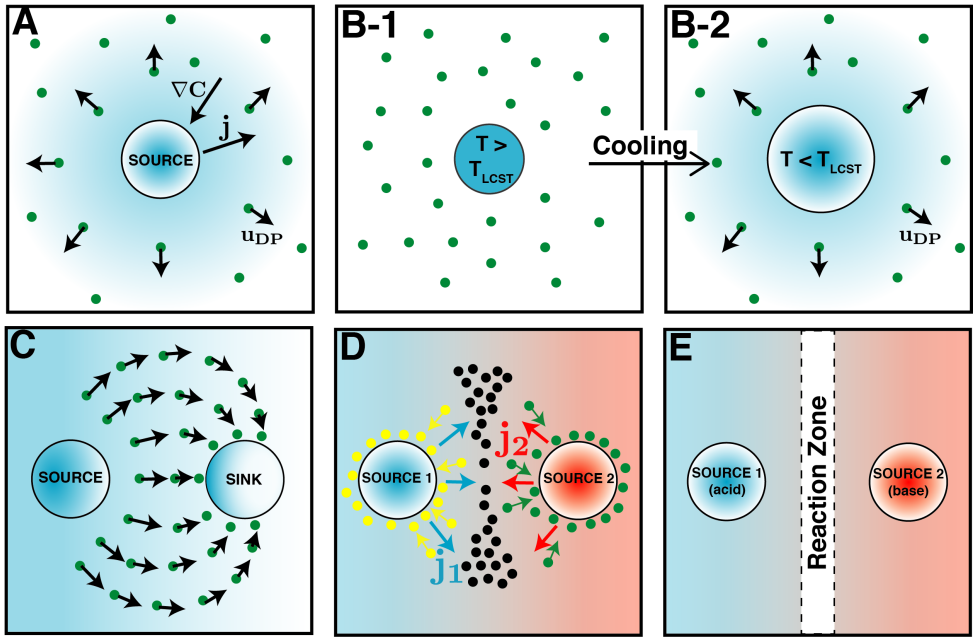

Figure 4.1: Employing SI beacons of one or more types to drive controlled colloidal migration. (A) A single SI beacon "source" that maintains solute outflux, driving DP migration (here down gradient) of particles, giving SI "repulsion". (B-1) Triggered release: a thermo-sensitive beacon keeps solute trapped at high enough temperature ($T > T_{LCST}$); (B-2) upon cooling below LCST, the beacon releases the solute, initiating SI migration. (C) SI Dipole: SI beacon source emits solute, as in (A), whereas the SI beacon "sink" absorbs the solute, establishing an SI dipolar flux that directs particle migration from one beacon to the other. (D) Combining SI beacon sources releasing distinct solutes may attract one particle species (yellow) to one source, a second species (green) to a second source, and repelling a third species of particle (black) from both. (E) SI beacon sources releasing solutes that react with one another (e.g. acid-base), establish long-lasting fluxes from each beacon to the reaction zone, driving particles accordingly.

intermediate locations in the suspension.

4.1 Triggered solute release and SI migration

The SI concept refers to beacons that absorb or release large amounts of solute in response to change in background solute concentration. Typically, SI beacons respond immediately when placed in contact with a solution with mismatched solute concentration

below the equilibrium value. Here, we demonstrate advanced strategies that employ an external trigger to initiate SI outflux from the beacon.

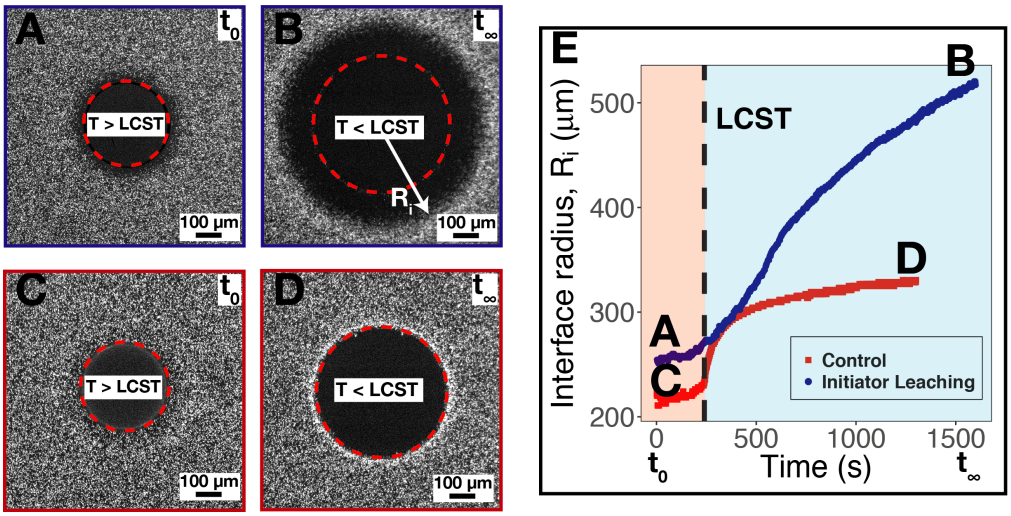

Figure 4.2: Triggered solute release and SI migration using pNIPAm beacons. (A) A pNIPAm gel above the LCST can be used to trap solute molecules. Dashed red line shows the gel boundary. (B) The gel swells when it cools below the LCST, the trapped solute diffuses out, establishing a concentration gradient that causes neighboring particles to migrate via DP. Control experiment: (C) The gel above the LCST closes its pores and occupies a smaller volume. (D) As the gel cools down the pores open up and it expands, pushing the neighboring particles out of the way. (E) Points represent the change in the particle interface radius (R_i) as the gels undergo transition at the LCST.

We use the temperature-sensitive polymer, poly-N-isopropylacrylamide (pNIPAm), crosslinked with methylene bis-acrylamide to make hydrogels (SI beacons)[1] using the projection lithography technique described previously.[2] pNIPAm has a lower critical solution temperature (LCST) of about 33 °C.[3] At temperatures below this LCST, it swells and absorbs water, whereas above the LCST, it phase separates into a dense polymer phase that expels solvent. We exploit this feature to trap solute within the beacon above the LCST. When it is cooled below the LCST, however, the hydrogel beacon swells, opening its pores and releasing the trapped solute.

Figure 4.2A shows a pNIPAm beacon at 50 °C, above LCST, so that the pNIPAm forms

a dense, collapsed polymer phase that traps the residual photoinitiator (α-ketoglutaric acid), which will serve as the SI solute. Negatively charged polystyrene (PS) particles are expected to electro-diffusiophoretically move down acidic gradients[4] and we confirm this trend for α-ketoglutaric acid using the three-channel microfluidic DP device of Paustian *et al.*[5] (Fig. 4.3).

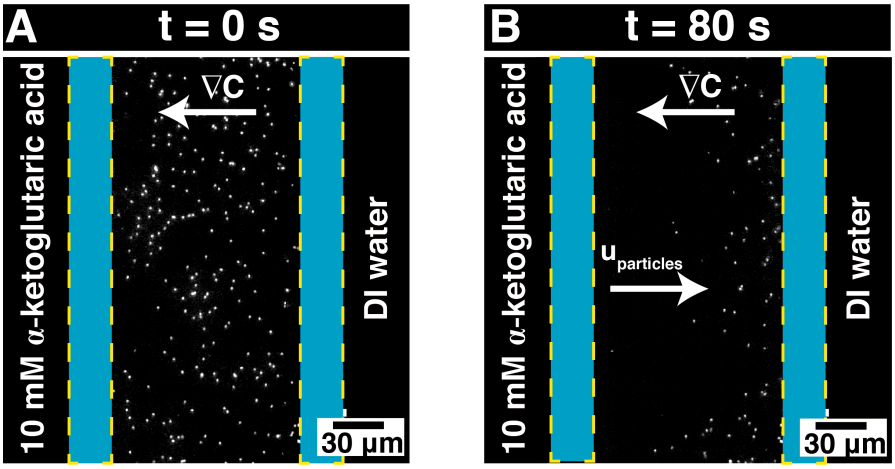

Figure 4.3: Migration of negative PS colloids under $\alpha-$ketoglutaric acid gradient. Negatively charged PS particles, (A) initially uniformly distributed, (B) migrate diffusiophoretically down $\alpha-$ketoglutaric acid gradients, as seen after 80 s.

So long as T>LCST, particles show no sign of DP migration, which would imply solute release (first 300 seconds of the blue data points in Fig. 4.2E). Upon cooling below LCST, the pNIPAm beacon expands (red dashed circle, Fig. 4.2B) releasing solute that drives SI repulsion of particles well beyond the edge of the swelling beacon (Fig. 4.2B and blue data points in Fig. 4.2E). As control, Fig. 4.2C shows a pNIPAm hydrogel from which all solute has been flushed, then raised above LCST. As the beacon is cooled below LCST, it swells as in Fig. 4.2B. In this case however, no solute is released that would drive SI DP, and so particles simply move to accomodate the expanding gel (Fig. 4.2D and red data points in Fig. 4.2E). The particle interface coincides with the beacon boundary, which quickly reaches a new radius upon cooling.

4.2 Source-sink pairs of SI beacons: SI dipole

The next strategy involves sculpting solute fluxes using one beacon as source to emit solute (here sodium dodecyl sulfate, SDS) and a second (empty) beacon as sink to absorb it. SI migration of particles is directed from the source to the sink as the diffusive solute flux forms a dipole. This targeted delivery of suspended particles represents enhanced control over DP migration compared to the single source case. Moreover, as DP velocities typically scale as the inverse of the solute concentration ($u_{DP} \propto \nabla \ln C$), SI dipoles can enhance u_{DP} and increase the duration of particle migration by maintaining a low background concentration, compared to an isolated source.

Figure 4.4A shows an isolated SI source releasing SDS, which drives radial migration of negatively charged PS particles, away from the beacon, consistent with previous findings.[2,6] The solute gradient and hence the particle motion is significantly altered when a sink absorbs SDS, causing colloids to be directed into the sink (Fig. 4.4B). A third, control experiment (Fig. 4.4C) is also performed using an inert obstacle in place of the solute sink, to show that solute absorption is responsible for the dipolar DP pattern, not merely the physical presence of a second beacon.

While the streak lines shown in Fig. 4.4A-C display qualitative features of SI migration behavior, particle tracking reveals quantitative details. For example, the azimuthal particle velocity V_ϕ is approximately zero around isolated SI source (blue squares in Fig. 4.4D), as expected for radial migration. Similarly, $V_\phi \approx 0$ for radial SI repulsion for the source and inert obstacle case (black diamonds), except near the obstacle. For source-sink dipole however, $V_\phi \neq 0$ (red circles). This source-sink SI migration behavior is confirmed using numerical computations on COMSOL, by first computing the diffusive flux between the source and the sink and then calculating $u_{DP} \propto \nabla \ln C$ (dashed lines in Fig. 4.4D, see Materials and Methods for full mass transport model).

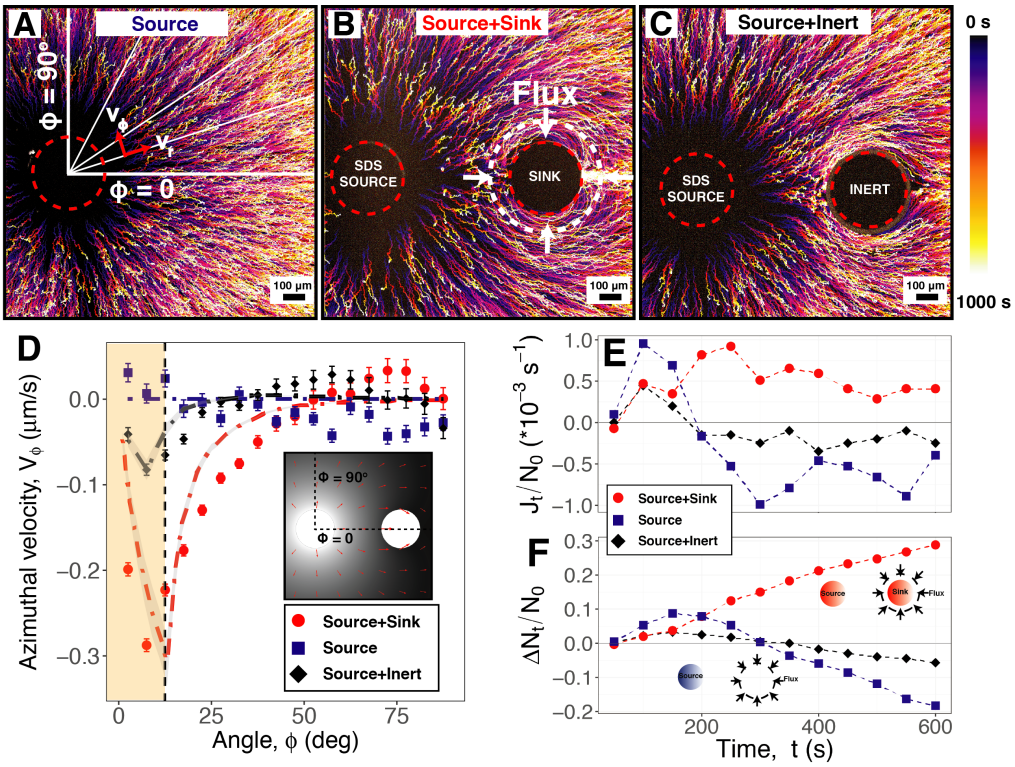

Figure 4.4: Soluto-inertial source-sink dipole. Streak lines showing the trajectories of negatively charged PS particles migrating due to (A) an SDS source, (B) both SDS source and sink, and (C) an SDS source and an inert obstacle that does not absorb SDS. (D) Time-averaged azimuthal particle velocities as a function of angular position with respect to the source centre under the scenarios depicted in (A-C). Error bars represent standard deviation. Points show experimental data. Lines are predictions from COMSOL computations. Shaded region shows angle subtended by sink at source centre, $\phi_{\text{sink}} = 12.5°$. Inset shows solute concentration field and local particle velocities as computed by COMSOL. (E) Flux of particles, J_t entering a region with radius $r = 1.5R_{beacon}$ around the sink. (F) Cumulative particles captured in the region as function of time (as a fraction of number of particles in that region at $t = 0$, N_0). Dashed lines are for visual guidance.

Figure 4.4E shows the flux of particles "collected" by the sink, determined by counting the change in the number of particles inside a circular region of radius $r = 1.5R_{beacon}$ around the sink per unit time, $J_t = \frac{1}{\Delta t} \sum_{t}^{t+\Delta t} N_{in} - N_{out}$. This flux is normalized by the total particles in that region counted at time $t = 0$, N_0. For both the isolated source (Fig. 4.4E, blue squares) and inert obstacle (black diamonds), this flux is initially positive as particles are repelled from the source, and repulsion "front" enters the region, then becomes negative after approximately 200 seconds once repulsion front passes beyond the ROI. The source-sink pair, by contrast, shows particle collection persisting for at least 600 seconds (red circles). The cumulative change in particle collection, $\Delta N_t = \sum_{0}^{t} N_{in} - N_{out}$ (normalized by N_0), shown in Fig. 4.4F, increases monotonically for the dipole, yet becomes negative after about 300 seconds for the other two cases, indicating a net loss of particles.

4.3 Pairs of SI beacon sources loaded with distinct solutes

Multiple SI beacon sources, each emitting a distinct solute may be combined to enable more complex particle collection strategies. For example, one source may repel particles while the other may attract, similar to the source-sink case, although with distinct solutes. The two beacons create a composite solute gradient which hastens migration from one to the other. This is shown in Fig. 4.5A where an SDS source (blue circle) repels negatively charged PS particles while a second beacon emitting the ionic liquid, 1-n-hexyl-3-methylimidazolium iodide ([C_6mim][I]; red circle) attracts particles. The combined effect is particle migration towards the right-hand beacon. The streak lines show particle trajectories over the first 1000 seconds of the experiment.

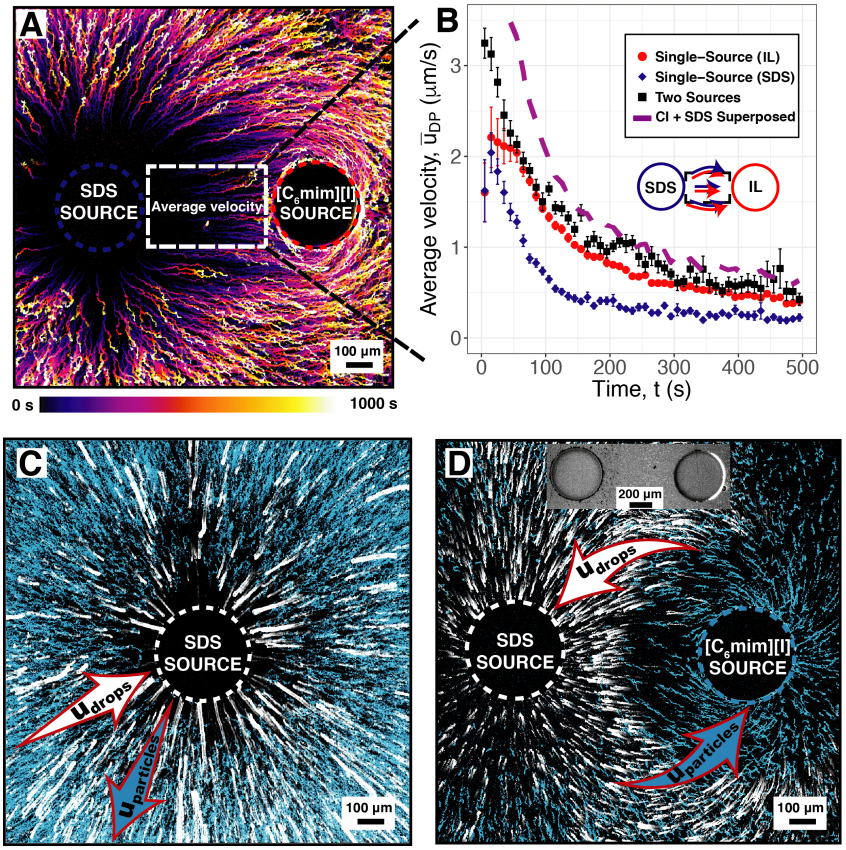

Figure 4.5: SI migration driven by two sources releasing distinct solutes. (A) Streak lines show negatively charged PS particles repelled by SDS source and attracted to ionic liquid (IL), [C_6mim][I] source. (B) SI particle velocities, averaged in the inter-beacon region, are larger when migrating under the composite gradient (black squares), than under either source in isolation, though slower than simple superposition of the two sources (purple dash). Error bars show standard deviation. (C) An SDS source repels negative PS particles (blue streaks), but simultaneously attracts decane drops (white streaks). (D) Distinct beacon sources, one releasing SDS (left), other releasing IL, [C_6mim][I] (right). Decane drops (white) migrate towards the SDS source beacon, whereas negative PS beads migrate towards the [C_6mim][I] source beacon. Inset shows accumulation of decane (black) and PS (white) particles around the two beacons at the end of the experiment.

To quantify the enhancement of both the magnitude and duration of u_{DP}, we calculate the average velocity of particles in the region between the two beacons as a function of time (Fig. 4.5B). We compare the speed and duration of migration under the composite solute gradient with those measured under each of the single solute gradients. Our observations

are as predicted: the composite gradient (black points) results in faster particle migration in the inter-beacon region than either of the two single solute gradients (blue diamonds and red circles). However, the resultant velocity under the composite gradient is less than the simple superposition of contributions from the individual sources (purple dashed line), discussed later.

The direction of particle migration depends on the nature of interaction between the solute and particle surface. We had previously exploited this feature to demonstrate oppositely-directed migration of negative PS beads and decane drops under an SDS gradient generated by a single beacon source (Fig. 4.5C,[2]). Here, we use the same principle to show that a combination of beacon sources releasing distinct solutes (SDS and $[C_6mim][I]$ in this case) causes negative PS beads to be attracted by the $[C_6mim][I]$ source (blue streaks in Fig. 4.5D) and decane drops by the SDS source (white streaks). The particles are eventually separated from the mixture, as seen in the inset of Fig. 4.5D – dark decane drops collect around the SDS beacon while a bright PS cloud forms around the $[C_6mim][I]$ beacon. The attraction of decane drops by an SDS source is not explained by DP, but is rather a consequence of "soluto-capillary" migration and is discussed later.

4.4 Pairs of SI beacon sources loaded with reactive solutes

Finally, we show that SI migration can be driven by two (or more) solute species that react with one another at an intermediate location. A strong flux of each reactant is directed to the reaction zone in this case, as the reactants are constantly consumed in the reaction. For example, a reactive multi-source system is shown in Fig. 4.6, where the reaction between $Ca(OH)_2$ (calcium hydroxide) and $C_7H_6O_2$ (benzoic acid) drives

positively charged PS particles towards the acidic beacon (Fig. 4.6A), and negatively charged PS particles towards the basic beacon (Fig. 4.6B). The streak lines show particle trajectories over the first 1000 seconds of the experiment.

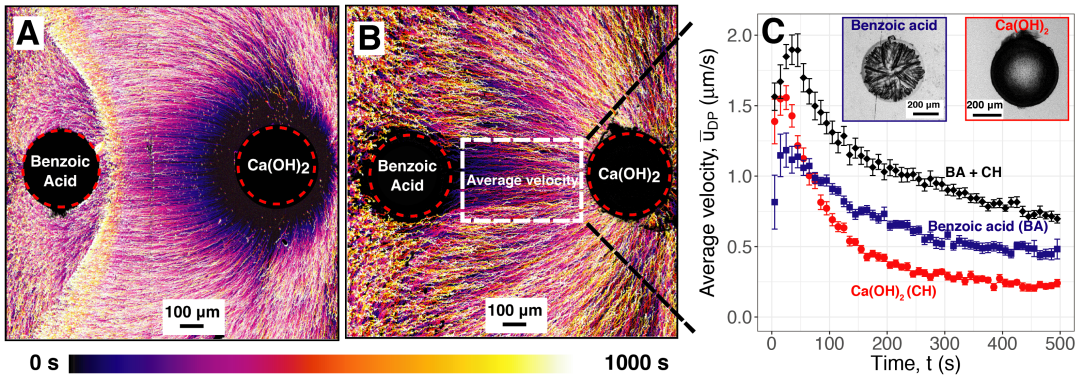

Figure 4.6: SI migration driven by reactive solutes. Streak lines showing migration under the flux generated by the reaction between $Ca(OH)_2$ and benzoic acid. (A) Aminated (positive) PS particles migrate towards the acidic beacon, while (B) sulfonated (negative) PS particles migrate towards the basic $Ca(OH)_2$ source. (C) Beads migrate the fastest and for a longer duration, when there is a reaction between the acid and base (black diamonds) as opposed to migrating under the flux of acid (blue squares) or base (red circles) alone. Error bars show standard deviation. Inset shows $Ca(OH)_2$ and benzoic acid crystals stored in the PEG-DA beacons in their solid form.

In addition to maintaining long-lived solute fluxes, reactive solutes prevent background solute concentration from growing continuously, which would generally suppress u_{DP}, since it is proportional to $\nabla \ln C$. Figure 4.6C shows the average particle velocities in the inter-beacon region as a function of time for the acid-base reaction (black diamonds), and under the single-component gradients of benzoic acid (blue squares) and calcium hydroxide (red circles). In the reactive, two-solute system, a steady particle flux is sustained for thousands of seconds, with higher migration velocities, compared to SI migration under the individual sources.

Thus far, SI beacons have been charged with solute by exploiting associative interaction between polymer and solute.[7–9] In this case however, we precipitate the solutes $Ca(OH)_2$ and $C_7H_6O_2$ inside the beacons in their solid forms (Fig. 4.6C Inset). The timescale for

SI interaction is therefore set by the solubility of the solid crystal in water, rather than by the partition coefficient or association constant of solute with the gel.

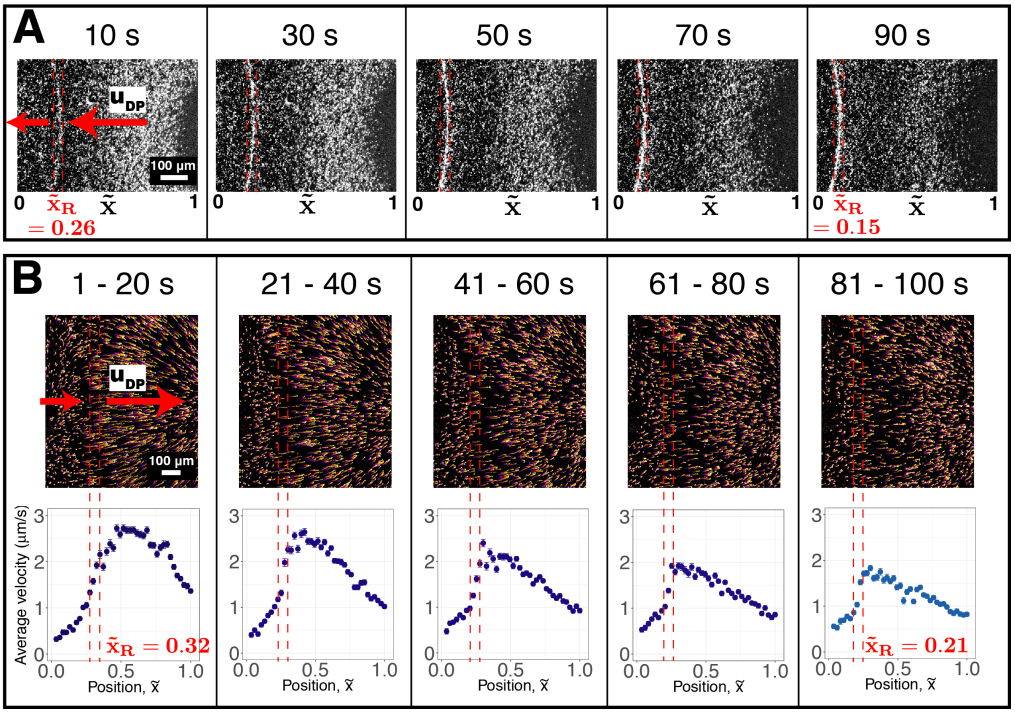

Figure 4.7: Focusing and defocusing of particles migrating under an acid-base flux. (A) Positive PS particles focus at the reaction zone. (B) Negative PS particles defocus at the reaction zone, which is defined as the region where a maximum change in velocity is observed. The reaction zone ($\tilde{x}_R$) gradually shifts to the left (towards the acid source) over the course of the experiment. Error bars represent standard deviation in average velocities over the time intervals. Positions are normalized by the distance between the two beacons.

The reaction between $Ca(OH)_2$ and $C_7H_6O_2$ obeys the following stoichiometry,

$$2\,C_7H_5O_2^- + 2\,H^+ + Ca^{2+} + 2\,OH^- \underset{k_b}{\overset{k_f}{\rightleftharpoons}} 2\,H_2O + Ca(C_7H_5O_2)_2 \tag{4.1}$$

implying that H^+ and OH^- fluxes abruptly terminate at the reaction zone, where they react to form water. It was recently shown that solute reactions (acid-base) may cause colloids to 'focus' diffusiophoretically.[4] This is indeed observed at the reaction between $Ca(OH)_2$ and $C_7H_6O_2$, where positive PS particles focus (Fig. 4.7A) and negative PS

particles defocus (Fig. 4.7B). While focusing is directly evident in the micrographs, defocusing is more difficult to discern. In both cases, the velocity on the right hand side of the reaction zone is greater than the left, causing a defocusing when particles move from left to right (negative PS) and focusing when they move from right to left (positive PS). Additionally, the reaction zone ($\tilde{x}_R$) gradually shifts towards the acidic beacon, which is a consequence of the ratio of diffusivities and solubilities of the two reactive species in water and the reaction stoichiometry (see scaling arguments presented in Materials and Methods).

4.5 Discussion and Conclusion

We have shown here that beacons can be triggered externally to release trapped solute and consequently initiate SI interactions by simply changing the local temperature in the beacon. We acknowledge that this is only one class of stimuli responsive beacon materials and users of such interactions might further expand on this work by designing beacons that can be activated by complimentary triggers such as light,[10,11] pH,[12] electric field[13] or ultrasound,[14] drawing inspiration from the controlled drug delivery literature.[15]

Using different combinations of two or more beacons, we have also demonstrated distinct strategies to direct and enhance colloidal migration over distances that are hundreds of times further than typical equilibrium suspension interactions. Each of our different strategies come with unique benefits and one might be preferred depending on the specific application. The source-sink dipole system requires minimal raw material input (only one solute is needed) and is a clean system as solute is absorbed by the sink. Moreover, the system is conceptually straightforward and simple mass transport models capture the experimental nuances, allowing theoretical prediction of behaviour.

Any combination of solutes can be used in the multi-source system which gives freedom

to tailor the directionality and speed of migration. Each solute-particle interaction adds a degree of control. This suggests the use of multiple beacons and solutes in order to separate multi-component suspensions and enable beacon-specific targeted delivery. The multi-source system with reactive solutes adds a further degree of tunability by introducing the ability to focus or defocus particles at intermediate locations. The chemical reaction maintains low background concentrations, maintaining larger velocities for longer durations. Solute outflux in the distinct multi-beacon strategies discussed here is mass transport limited, however, these beacons could in principle be replaced by pNIPAm beacons to initiate interactions on-demand.

Any solute gradient can potentially induce colloidal motion, so long as the solute interacts with the particle surface. The interaction may be electrostatic in nature in which case the particles migrate via DP. It may also be driven by capillary/interfacial forces, where the solute reduces the surface tension of the particle, creating Marangoni stresses along the surface.[16–18] These surface tension gradients cause the decane drops in Fig. 4.5C,D to move towards higher concentrations of SDS, i.e. towards regions where the droplets can lower their surface tension in water. Chemical gradients may further give rise to density gradients, which could lead to density driven fluid flows.[19] Solute concentrations in our experiments, however, are small enough, and microfluidic geometries are confined enough that we neither expect nor observe buoyancy-driven convective flows. An interesting aspect to note is that PS particles in Fig. 4.4B as well as in Fig. 4.5A,D accumulate at the back of the beacon absorbing SDS. We hypothesize that this is due to the formation of concentration gradient around the periphery, pertaining to slow intra-diffusion of SDS within the beacon.

The difficulty in modeling systems with more than one interacting solute species stems from the fact that concentration profiles in these systems are not simply additive. In multicomponent electrolyte systems, the ionic fluxes balance one another in order

to maintain local electro-neutrality, resulting in a net electric field that drives the DP migration. Thus, detailed information on the specific ion concentration profiles between the sources is required to use classic DP theories and correctly predict resultant particle velocities.[20] The non-trivial consequences of coupled, multicomponent fluxes is highlighted in the fact that the contribution of different sources do not superimpose in Fig. 4.5B and the velocity profiles on either side of the reaction zone are discontinuous in Fig. 4.7, resulting in focusing or defocusing of particles in reactive systems.

We envision that suitably designed, controlled SI interactions will find a range of applications in soft matter and mesoscale systems. Researchers are starting to realize the ubiquity of the DP phenomenon[21] and have demonstrated its versatility in a variety of applications such as deposition of latex on steel,[22] water purification,[23] transport into and out of dead end pores,[24,25] self propelling particles[26–29] and active matter.[30–32] The strategies demonstrated here show that concentration gradients can be exploited as a controllable external field for suspension manipulation and may augment existing techniques for colloidal handling and processing. These may include sorting particles or cells with similar size but different surface chemistry,[33] driving particles to target regions and delivering active ingredients, enhancing rates of suspension flocculation in dilute suspensions where even commercial flocculants would take much longer to form aggregates, analyzing colloidal mixtures and phase behavior, directing colloidal assembly and synthesizing novel materials.

4.6 Materials and Methods

4.6.1 Device Fabrication

A computer-controlled laser cutter (Trotec Speedy 100) cuts the channel design into 60 μm-thick Scotch tape. This is stuck to a Petri dish, which is used as a master for making a polydimethylsiloxane (PDMS) replica of the design. The PDMS master is used to fabricate the device in "microfluidic stickers" (NOA – 81; Norland Adhesive).[34] A glass cover slide is used to seal the device, with holes drilled to provide access for inlet and outlet tubing. A PDMS inlet is ozone-bonded to the cover slide to provide support for pins and tubings. The device is then baked at 80 °C for at least 4 hours to strengthen bonding. For the triggered release experiments, the microfluidic device has same dimensions as the one used in our previous work.[2] For the multi-beacon experiments, a two inlet, single outlet microfluidic device is used, where the two inlets enable the simultaneous flow of two different liquid streams side by side. The two inlets are 500 μm wide while the center channel where the inlets merge has a width of 4000 μm.

4.6.2 Sample Preparations

Precursor solutions of pNIPAm are prepared by mixing 1 M NIPAM (Sigma-Aldrich) solution with 0.5 mol% cross-linker (N, N'-methylenebisacrylamide; Sigma-Aldrich) and 5 mol% photoinitiator ($\alpha-$ketoglutaric acid; Sigma-Aldrich) in deionized (DI) water; PEG-DA precursor solutions are prepared by mixing 33% (vol/vol) PEG(700)-DA (Sigma-Aldrich) with 4% (vol/vol) photoinitiator (2-hydroxy-2-methylpropiophenone; Sigma-Aldrich) in DI water. Stock solutions of SDS (Sigma-Aldrich), [C_6mim][I] (Sigma-Aldrich) and NaOH (EMD Millipore) in DI water and $CaCl_2.2H_2O$ (Sigma-Aldrich), benzoic acid (Acros Organics) in ethanol are prepared and diluted according to the experimental

requirements; Negative and positive PS suspensions are prepared by suspending 0.25% (vol/vol) fluorescent sulfonated PS beads, 1 μm in diameter (FS03F; Bangs Laboratories) and 0.5% (vol/vol) aminated PS beads, 1.8 μm in diameter (PA04N; Bangs Laboratories) in DI water, respectively. Surfactant-free suspensions of decane drops are created by sonicating 2% (vol/vol) decane (Sigma-Aldrich) in DI water for 1 minute.

4.6.3 Experimental Setup

1. Hydrogel (beacon): pNIPAm and PEG-DA gels are used as SI structures and fabricated using the microscope projection lithography technique.[35] A UV lamp is set to 30 mW/cm^2 (measured at an empty objective slot). A 1000 μm diameter circular photomask is inserted into the field stop of an inverted microscope (Nikon TE-2000U) and aligned as described previously.[36] pNIPAm/PEG-DA precursor solution is injected until the channel is filled. The syringe is disconnected, and 2 min are allowed for flow to relax. Then a 20 s (for pNIPAm gels) and 500 ms (for PEG-DA gels) UV exposure is used with a 10$\times$ objective to photopolymerize the gel. This results in hydrogel posts of diameter $375 - 425$ μm. The precursor solution is flushed from the device by flowing DI water for 2 hours for the PEG-DA gels.

2. The pNIPAm gel is flushed with DI water for 24 hours for the control experiment, and only 10 minutes when some amount of residual photoinitiator is desired inside the gel. The microfluidic device is mounted on a thermal stage (Instec TSA12Gi) to control the temperature of the pNIPAm gel. The device is maintained at 50 ^{o}C at the beginning of the experiment. Negative PS suspension at the same temperature is introduced into the device, flow is stopped using technique described in[5] and video recording (Andor iXon 885 fluorescence camera) is started with a 4$\times$ objective at one frame per second with 0.1 s exposure time. The temperature of the stage

is then lowered to 25 °C to allow the gel to cool down and cross the LCST. Video recording is stopped 30 minutes after the gel undergoes the transition.

3. Source-Sink: Two streams, one with 5 mM SDS in water and the other with clean DI water, are flowed simultaneously into the channel using the two inlets of the device. In this way one of the beacons (the source) is loaded with SDS, while the other (sink) remains unloaded. After loading the source for 20 minutes, the two streams are flushed out by displacing with the suspension of negative PS particles. The flow is stopped and video recording is started.

    - Inert sink: An NOA - 81 post is used as the inert structure and fabricated using microscope projection lithography technique, following the same procedure as with the PEG-DA beacons.

4. Multiple source: Two streams, one with 5 mM SDS in water and the other with 5 mM [C_6mim][I] in water, are flowed simultaneously into the channel. Both the sources are loaded for 20 minutes, before flushing with a suspension of negative PS particles/decane drops. Flow is stopped and image series are recorded.

5. Multiple sources with reaction: Two streams, one with 0.15 g/mL of $CaCl_2.2H_2O$ in ethanol and the other with 0.4 g/mL benzoic acid in ethanol, are flowed simultaneously into the channel. The two beacons are loaded for 10 minutes and subsequently flushed with 0.08 g/mL NaOH in water and DI water, respectively. The NaOH reacts with $CaCl_2$ to precipitate out $Ca(OH)_2$ in the first beacon while water reduces solvent quality for benzoic acid, resulting in BA crystal formation in the second beacon (Fig. 4.6C Inset). The two streams are then flushed by displacing with the PS suspensions. Flow is stopped and image series are recorded.

4.6.4 Data Analysis

Particles are identified and trajectories are linked from the fluorescent micrographs following the same procedure as described in.[2] The azimuthal velocity in Fig. 4.4D is calculated by first dividing the micrograph along the line of symmetry (y = 0) and analyzing only one half (to reduce computation time). Instantaneous particle velocities in the radial and tangential direction are obtained from frame-to-frame displacements, and velocity profiles are calculated by averaging the velocities within angular regions of 5 degrees width with the origin fixed at the center of the source. The velocity profiles are further averaged over an interval of 500 seconds. The space average velocities in Fig. 4.5C and 4.6C are extracted by first cropping the micrograph in the space between the two beacons into rectangular regions with approximate dimensions, 320 x 250 pixels and then measuring the displacement of the particles in the x-direction (and hence the x component of the velocity). The velocity profiles are calculated independently over 10 s intervals, throughout the experiment, and averaged over all of space. Velocity for single source systems in these cases refers to the average velocity of particles in the space between source-sink beacon pairs of corresponding solutes. The time average velocities in Fig. 4.7B are also extracted in the same way as the space average velocities. The velocity profiles in this case are however calculated by averaging the velocities within spatial bins of 10 pixels width, and further averaged over the given time interval. Splitting the experiment into chunks in this way provides more samples in each bin, improving the statistics of averaging and suppressing noise in the velocity profiles. The particle flux in Fig. 4.4E,F is calculated by directly counting the number of particles entering and exiting a region of radius $r \approx 300\ \mu\text{m} \approx 1.5R_{beacon}$ around the sink. This number is then normalized by the total number of particles counted in that region at the beginning of the experiment. The particle flux for a single source (blue points in Fig. 4.4E,F) is calculated

by counting the number of particles entering an imaginary ring (of $r \approx 300$ μm), situated at the same location as the sink in the source-sink experiments.

4.6.5 Model for SI dipole

The `Transport of Diluted Species` module of COMSOL Multiphysics is used to numerically solve the coupled solute and particle conservation equations. The microfluidic device and beacon dimensions used for the computations are directly obtained from experimental measurements and other physical paramters such as the diffusion coefficient of SDS are obtained from the literature. Space is meshed with a triangular mesh and solute and particle concentration profiles are calculated. Results are then exported in matrix form and post-processed in R to obtain radial (V_r) and azimuthal (V_ϕ) particle velocities.

The unsteady diffusion of solute in the source and sink obeys

$$\frac{\partial C_i}{\partial t} = \boldsymbol{\nabla} \cdot D_B \boldsymbol{\nabla} C_i, \tag{4.2}$$

where, D_B is the diffusivity of SDS in the PEG-DA beacon, and C_i is the concentration of solute inside the source/sink. Similarly, the concentration profile of SDS in solution can be obtained by solving

$$\frac{\partial C_S}{\partial t} = \boldsymbol{\nabla} \cdot D_S \boldsymbol{\nabla} C_S, \tag{4.3}$$

where, D_S is the diffusivity of SDS in water and C_S is the concentration in solution. Equations 4.2 and 4.3 are subject to the following initial and boundary conditions

$$\text{Source}: \quad C_i(t=0) = PC_0, \tag{4.4}$$

$$\text{Sink}: \quad C_i(t=0) = 0, \tag{4.5}$$

$$C_S(t=0) = 0, \tag{4.6}$$

$$C_i = PC_S \quad \text{at the solution} - \text{beacon boundary}, \tag{4.7}$$

$$\hat{\boldsymbol{n}} \cdot D_S \boldsymbol{\nabla} C_S = \hat{\boldsymbol{n}} \cdot D_B \boldsymbol{\nabla} C_i \quad \text{at the solution} - \text{beacon boundary}, \tag{4.8}$$

$$\hat{\boldsymbol{n}} \cdot D_S \boldsymbol{\nabla} C_S = 0 \quad \text{at the edge of the channel.} \tag{4.9}$$

Here, $\hat{\boldsymbol{n}}$ is the outward unit normal on the respective boundaries P is the partition coefficient of SDS in the PEG-DA beacon and C_0 is the known initial loading concentration. Having solved for the concentration profile of SDS in solution, the x and y DP velocities can be calculated, imposing

$$\boldsymbol{u_{DP}^{x}} = D_{DP} \frac{\partial C_S}{\partial x} \frac{1}{C_S} \hat{\boldsymbol{e}}_{\boldsymbol{x}}, \tag{4.10}$$

$$\boldsymbol{u_{DP}^{y}} = D_{DP} \frac{\partial C_S}{\partial y} \frac{1}{C_S} \hat{\boldsymbol{e}}_{\boldsymbol{y}}, \tag{4.11}$$

where $\hat{\boldsymbol{e}}_{\boldsymbol{x}}$ and $\hat{\boldsymbol{e}}_{\boldsymbol{y}}$ are unit normals in the x- and y-directions, respectively, and D_{DP} is the DP mobility of particles. The DP velocity can be used to solve for the concentration profile of PS particles in the suspension, following

$$\frac{\partial C_P}{\partial t} = \boldsymbol{\nabla} \cdot (D_P \boldsymbol{\nabla} C_P - \boldsymbol{u_{DP}} C_P), \tag{4.12}$$

where, D_P is the diffusivity of the particles and C_P is their concentration in suspension. The conservation equation 4.12 is subject to the following initial and boundary conditions

$$C_P(t=0) = C_P^0, \tag{4.13}$$

$$\hat{\boldsymbol{n}} \cdot (\boldsymbol{u_{DP}} C_P - D_P \boldsymbol{\nabla} C_P) = 0 \quad \text{at beacon and channel boundaries}, \tag{4.14}$$

$$C_P = 0 \quad \text{inside source and sink at all times.} \tag{4.15}$$

Particle velocities obtained from this numerical model show good agreement with the experimentally measured velocities, as seen in Fig. 4.4D. Both experiments and computations further reveal eventual accumulation of particles at the back of the sink. Our hypothesis for this observation is as follows – the diffusion of SDS inside the beacon is slow enough to create concentration gradients along the periphery of the sink, where the front (side of the sink that directly faces the source) attains a higher concentration than the back. PS particles that move down an SDS gradient, then naturally migrate to the back of the sink, towards a lower concentration. The values of D_B, D_S, P and D_{DP} used for the numerical model are reported in table 4.1.

D_S	D_B	P	D_{DP}
780 μm^2/s[37]	70 μm^2/s	4	60 μm^2/s[6]

Table 4.1: Parameters used for numerically calculating the concentration profile of PS particles migrating under an SDS flux, generated by source-sink pair of SI beacons.

4.6.6 Focusing/defocusing of PS particles migrating under flux generated by an acid-base reaction

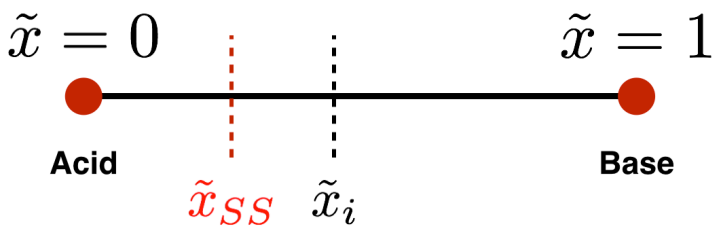

Figure 4.8: Predicting focusing/defocusing of particles migrating under reactive fluxes. The reaction between the acid and base released by the two beacon sources situated at $\tilde{x} = 0$ and 1, respectively establishes an initial reaction site where the two species first meet ($\tilde{x}_i$). The reaction then reaches a steady state, which leads to a gradual shift in the location of the reaction zone ($\tilde{x}_{SS}$) towards the acidic beacon.

The reaction front ($\tilde{x}_R$ in Fig. 4.7) shifts towards the acidic beacon, over the course of the experiment. Here we present a simple analysis to speculate the cause of this shift, by calculating the diffusion time for the two species as well as doing a flux balance at the reaction site at steady state. The basic argument is that the acid and the base solute molecules first meet at some intermediate location between the two beacons ($\tilde{x}_i$) and the location of this meeting point depends purely on the diffusivity of the two species. Eventually they establish a steady state, where the two species react completely to form water and their corresponding salt, which results in a shift in the reaction zone ($\tilde{x}_{SS}$; Fig. 4.8). The actual experiments are 2D in nature, however we restrict our analysis to a 1D system for ease of calculation and sake of simplicity. We believe the arguments presented here should be qualitatively applicable to a 2D system.

To obtain the first meeting point, we equate the diffusive time for the acid and the base

$$\tau = \frac{\tilde{x}_i^2}{D_A} = \frac{(1-\tilde{x}_i)^2}{D_B}, \tag{4.16}$$

$$\tilde{x}_i = \frac{1}{1+\sqrt{\frac{D_B}{D_A}}} = \frac{1}{1+\sqrt{D_r}}, \tag{4.17}$$

where, τ is the diffusive time, $\tilde{x}_i$ is the initial meeting point of the two species, D_B and D_A are the diffusivities of the base and acid respectively, while D_r is their ratio, $D_r = D_B/D_A$. As expected, the first meeting point simply depends on the ratio of diffusivity of the acid and the base in water.

At steady state, the acidic flux balances the basic flux, assuming the reaction goes to completion. The reaction stoichiometry governs two moles of benzoic acid to react with

one mole of calcium hydroxide, leading to the following flux balance equation

$$-D_A \frac{\Delta C_A}{\Delta x}\bigg|_{\tilde{x}=\tilde{x}_{SS}} = 2D_B \frac{\Delta C_B}{\Delta x}\bigg|_{\tilde{x}=x\tilde{s}_{SS}}, \tag{4.18}$$

$$-D_A \frac{0 - C_A^0}{\tilde{x}_{SS}} \approx 2D_B \frac{0 - C_B^0}{\tilde{x}_{SS} - 1}, \tag{4.19}$$

$$\tilde{x}_{SS} = \frac{1}{1 + 2\frac{D_B}{D_A}\frac{C_B^0}{C_A^0}} \approx \frac{1}{1 + 2D_r S_r}, \tag{4.20}$$

where, $\tilde{x}_{SS}$ is the steady state reaction zone, C_B^0 and C_A^0 are the solubilities of the base and the acid in water, respectively while S_r is their ratio. Thus the steady state location of the reaction zone not only depends on the diffusivity, but also on the ratio of solubility of the two species.

D_A	D_B	C_A^0	C_B^0
1000 μm^2/s[38]	1600 μm^2/s[39]	22 mM	23 mM

Table 4.2: Diffusivity and solubility of benzoic acid and calcium hydroxide in water.

Table 4.2 lists values of D_A, D_B, C_A^0, and C_B^0 for benzoic acid and calcium hydroxide. From equations 4.17 and 4.20, we can conclude that the location of the initial and steady state reaction sites only depends on the ratio of diffusivity (D_r) and solubility (S_r) of the acid and the base. For benzoic acid and calcium hydroxide, these values are 1.6 and 1.05 respectively. Plugging these values of D_r and S_r into equations 4.17 and 4.20 reveals, $\tilde{x}_i = 0.44$ and $\tilde{x}_{SS} = 0.23$. Thus, it becomes directly evident from these simple calculations that the steady state location of the reaction front at latter times is much closer to the acidic beacon than its initial location, consistent with our experimental observations. 2D systems however, are inherently unsteady and therefore we do not claim any quantitative correlation between experimental findings and the analytical model. Nevertheless, the simple 1D model presented here provides a framework for tracking and predicting the approximate location of reaction fronts and consequently particle focusing/defocusing

regions in such reactive, multi-solute systems.

Acknowledgements

We gratefully acknowledge support from the National Science Foundation (NSF) under Grant CBET-1438779 and the Saudi Arabian Oil Company (Saudi Aramco). We thank Johanna Eriksson, Dr. Ian Williams, Dr. Nan Shi, Dr. Alexandra Bayles and Prof. Javier Read de Alaniz for valuable discussions. A portion of this work was performed in the Microfluidics Laboratory and the Biological Nanostructures Laboratory within the California NanoSystems Institute, supported by the University of California, Santa Barbara and the University of California, Office of the President, and in the Shared Experimental Facilities of the Materials Research Science and Engineering.

Bibliography

[1] Pelton R, Chibante P. Preparation of aqueous latices with n-isopropylacrylamide. *Colloids and Surfaces.* 1986; 20(3): 247 - 256.

[2] Banerjee A, Williams I, Azevedo RN, Helgeson ME, Squires TM. Soluto-inertial phenomena: Designing long-range, long-lasting, surface-specific interactions in suspensions. *Proceedings of the National Academy of Sciences.* 2016; 113(31): 8612-8617.

[3] Hirokawa Y, Tanaka T. Volume phase transition in a nonionic gel. *The Journal of Chemical Physics.* 1984; 81(12): 6379–6380.

[4] Shi N, Nery-Azevedo R, Abdel-Fattah AI, Squires TM. Diffusiophoretic Focusing of Suspended Colloids. *Physical Review Letters.* 2016; 258001(117): 1–5.

[5] Paustian JS, Angulo CD, Nery-Azevedo R, Shi N, Abdel-Fattah AI, Squires TM. Direct Measurements of Colloidal Solvophoresis under Imposed Solvent and Solute Gradients. *Langmuir.* 2015; 31: 4402–4410.

[6] Nery-Azevedo R, Banerjee A, Squires TM. Diffusiophoresis in Ionic Surfactant Gradients. *Langmuir.* 2017(1).

[7] Tam KC, Wyn-Jones E. Insights on polymer surfactant complex structures during the binding of surfactants to polymers as measured by equilibrium and structural techniques. *Chemical Society reviews.* 2006; 35(8): 693–709.

[8] Kim J, Gao Y, Hebebrand C, Peirtsegaele E, Helgeson ME. Polymer-surfactant complexation as a generic route to responsive viscoelastic nanoemulsions. *Soft Matter.* 2013; 9: 6897-6910.

[9] Luo S, Zhang S, Wang Y, et al. Complexes of ionic liquids with poly(ethylene glycol)s. *Journal of Organic Chemistry.* 2010; 75(6): 1888–1891.

[10] Kloxin AM, Kasko AM, Salinas CN, Anseth KS. Photodegradable hydrogels for dynamic tuning of physica and chemical properties. *Science.* 2009; 324: 59-63.

[11] Helmy S, Leibfarth FA, Oh S, Poelma JE, Hawker CJ, Alaniz J. Photoswitching using visible light: A new class of organic photochromic molecules. *Journal of the American Chemical Society.* 2014; 136(23): 8169-8172. PMID: 24848124.

[12] Zhang S, Bellinger AM, Glettig DL, et al. A ph-responsive supramolecular polymer gel as an enteric elastomer for use in gastric devices. *Nature Materials.* 2015; 14(10): 1065–1071.

[13] Murdan S. Electro-responsive drug delivery from hydrogels. *J Control Release.* 2003; 92(1-2): 1-17.

[14] Huebsch N, Kearney CJ, Zhao X, et al. Ultrasound-triggered disruption and self-healing of reversibly cross-linked hydrogels for drug delivery and enhanced chemotherapy. *Proceedings of the National Academy of Sciences.* 2014; 111(27): 9762–9767.

[15] Li J, Mooney DJ. Designing hydrogels for controlled drug delivery. *Nature Reviews Materials.* 2016; 1(12).

[16] Levich BG, Kuznetsov AM. On the motion of drops in liquids under the action of surface active substances. *Dokl. Acad. Nauk SSSR.* 1962; 146: 145–147.

[17] Squires TM, Quake SR. Microfluidics: Fluid physics at the nanoliter scale. *Rev. Mod. Phys..* 2005; 77: 977–1026.

[18] Jin C, Krüger C, Maass CC. Chemotaxis and autochemotaxis of self-propelling droplet swimmers. *Proceedings of the National Academy of Sciences.* 2017.

[19] Das S, Shklyaev OE, Altemose A, et al. Harnessing catalytic pumps for directional delivery of microparticles in microchambers. *Nature Communications.* 2017; 8: 14384 EP -.

[20] Chiang TY, Velegol D. Multi-ion diffusiophoresis. *Journal of Colloid And Interface Science.* 2014; 424: 120–123.

[21] Velegol D, Garg A, Guha R, Kar A, Kumar M. Origins of concentration gradients for diffusiophoresis. *Soft Matter.* 2016; 12: 4686–4703.

[22] Derjaguin BV, Dukhin SS, Korotkova AA. Diffusiophoresis in electrolyte solutions and its role in the Mechanism of the formation of films from caoutchouc latexes by the ionic deposition method. *Progress in Surface Science.* 1993; 43(20): 153–158.

[23] Shin S, Shardt O, Warren PB, Stone HA. Membraneless water filtration using CO 2. *Nature Communications.* 2017; 8(May): 1–6.

[24] Kar A, Chiang TY, Ortiz Rivera I, Sen A, Velegol D. Enhanced transport into and out of dead-end pores. *ACS nano.* 2015; 9(1): 746–53.

[25] Shin S, Um E, Sabass B, Ault JT, Rahimi M, Warren PB. Size-dependent control of colloid transport via solute gradients in dead-end channels. *Proceedings of the National Academy of Sciences.* 2016; 113(2): 257-261.

[26] Kline TR, Paxton WF, Mallouk TE, Sen A. Catalytic Nanomotors: Remote-Controlled Autonomous Movement of Striped Metallic Nanorods. *Angewandte Chemie.* 2005; 117(5): 754–756.

[27] Moran JL, Posner JD. Electrokinetic locomotion due to reaction-induced charge auto-electrophoresis. *Journal of Fluid Mechanics.* 2011; 680: 31–66.

[28] Brady JF. Particle motion driven by solute gradients with application to autonomous motion: continuum and colloidal perspectives. *Journal of Fluid Mechanics.* 2011; 667: 216–259.

[29] Golestanian R, Liverpool TB, Ajdari A. Propulsion of a molecular machine by asymmetric distribution of reaction products. *Physical Review Letters.* 2005; 94(22): 1–4.

[30] Ibele M, Mallouk TE, Sen A. Schooling behavior of light-powered autonomous micromotors in water. *Angewandte Chemie - International Edition.* 2009; 48(18): 3308–3312.

[31] Theurkauff I, Cottin-Bizonne C, Palacci J, Ybert C, Bocquet L. Dynamic clustering in active colloidal suspensions with chemical signaling. *Physical Review Letters.* 2012; 108(June): 1–5.

[32] Buttinoni I, Volpe G, Kümmel F, Volpe G, Bechinger C. Active Brownian motion tunable by light. *Journal of Physics: Condensed Matter.* 2012; 24: 284129.

[33] Fukuyama T, Fuke A, Mochizuki M, Kamei Ki, Maeda YT. Directing and boosting of cell migration by the entropic force gradient in polymer solution. *Langmuir.* 2015; 31(46): 12567-12572. PMID: 26496637.

[34] Bartolo D, Degré G, Nghe P, Studer V. Microfluidic stickers. *Lab on a Chip.* 2008; 8: 274–279.

[35] Dendukuri D, Gu SS, Pregibon DC, Hatton TA, Doyle PS. Stop-flow lithography in a microfluidic device. *Lab on a Chip.* 2007; 7(7): 818–828.

[36] Paustian JS, Azevedo RN, Lundin STB, Gilkey MJ, Squires TM. Microfluidic microdialysis: Spatiotemporal control over solution microenvironments using integrated hydrogel membrane microwindows. *Physical Review X.* 2014; 3: 1–13.

[37] Leaist DO. Binary diffusion of micellar electrolytes. *Journal of Colloid and Interface Science.* 1986; 111(1): 230–239.

[38] Noulty RA, Leaist DG. Diffusion coefficient of aqueous benzoic acid at 25.degree.c. *Journal of Chemical & Engineering Data.* 1987; 32(4): 418-420.

[39] Robinson RA, Stokes RH. *Electrolyte Solutions.* Butterworths, London 1959.

Chapter 5

Design strategies for engineering soluto-inertial suspension interactions

Designing SI interactions for a particular application requires a solute be chosen to attract or repel colloids of interest, and a beacon that slowly absorbs or releases that solute. Moreover, geometric and material parameters must be chosen with duration and range in mind. For example, gradients in solution can be established by source beacons that emit solute or sink beacons that absorb solute. However, since solute concentration profiles around sources and sinks can be quite different, they may give rise to qualitatively distinct DP velocity profiles, which typically vary with $\nabla \ln C$.[1–4] Consequently, the range and duration of interaction may differ significantly for sources and sinks, even though solute transport obeys the same mass conservation equations around them.

Here, we present a systematic map of the parameter space available for SI interactions. SI beacons must have high solute capacity (e.g. high partition coefficient or association

This chapter is adapted from Banerjee, Vogus, Squires *Physical Review E.* 2019; under review.

constant) to maintain long-lived solute gradients. Such gradients may also be established in solution by dissolving solids[5] and gases,[6] by ion exchange materials[7,8] as well as evaporating liquids[9] to drive SI suspension interactions. Velegol *et. al.* summarized a variety of distinct physical processes that establish concentration gradients and drive DP migration of colloids.[10] The strategies and guidelines laid out here should facilitate conceptual design and material selection for such systems more generally.

Specifically, we illustrate our strategy for two distinct classes of beacons – beacons that partition solute (e.g. oils), and beacons that associate with solute (e.g. hydrogels). Our approach is as follows: first, we identify the governing equations for a specific beacon material class, and isolate the design parameters. Next, we determine the time scales associated with various mass transport processes during solute loading and unloading. Comparing the time scales reveals the slowest, rate limiting step, which is significant conceptually and also motivates approximations that simplify the governing equations and solutions. Finally, we predict the DP velocity of colloidal particles interacting with beacon sources and sinks, and compare their qualitative features.

In our earlier work,[14] we used 2D cylindrical posts as beacons. However, since the mass transport in the 2D systems we modeled is inherently unsteady, our analysis here considers spheres, as will be relevant for freely suspended SI beacons.

5.1 SI beacons that partition solute

The first class of SI beacons are those that partition solute, meaning that it is energetically favorable for solute molecules to dissolve in the beacon phase than in the solution phase. At equilibrium, the solute concentration C_B inside the beacon exceeds

the concentration C_S in solution by the partition coefficient P,[11,12] defined by

$$P = \frac{C_B}{C_S}. \tag{5.1}$$

For example, an organic phase like octanol partitions hydrophobic solutes like butanol relative to an aqueous phase.[13] Solute diffuses within each phase according to

$$\frac{\partial C_B}{\partial t} = \frac{D_B}{r^2}\frac{\partial}{\partial r}\left(r^2\frac{\partial C_B}{\partial r}\right), \tag{5.2}$$

$$\frac{\partial C_S}{\partial t} = \frac{D_S}{r^2}\frac{\partial}{\partial r}\left(r^2\frac{\partial C_S}{\partial r}\right), \tag{5.3}$$

where D_B and D_S are solute diffusivities in the beacon and solution phases, respectively. Imposing concentration and flux continuity at the beacon-solution interface ($r = R_B$) gives

$$C_B(R_B, t) = PC_S(R_B, t), \tag{5.4}$$

$$D_B\frac{\partial C_B}{\partial r}\bigg|_{R_B} = D_S\frac{\partial C_S}{\partial r}\bigg|_{R_B}, \tag{5.5}$$

where R_B is the radius of the spherical beacon. A beacon source unloading solute obeys the initial conditions,

$$C_B(r \leq R_B,\ t = 0) = PC_0, \tag{5.6}$$

$$C_S(r > R_B,\ t = 0) = 0. \tag{5.7}$$

whereas a beacon sink in solution obeys

$$C_B(r \leq R_B,\ t = 0) = 0, \tag{5.8}$$

$$C_S(r > R_B,\ t = 0) = C_0. \tag{5.9}$$

Non-dimensionalizing Eqs. (5.2 – 5.5) with $C_S = C_0\tilde{C_S}$, $C_B = PC_0\tilde{C_B}$, $r = R_B\tilde{r}$ and $t = \tau_{SI}^0\tilde{t}$ (where τ_{SI}^0 is as yet undefined), gives

$$\frac{R_B^2}{\tau_{SI}^0 D_B}\frac{\partial\tilde{C}_B}{\partial\tilde{t}} = \tilde{\nabla}^2\tilde{C}_B, \tag{5.10}$$

$$\frac{R_B^2}{\tau_{SI}^0 D_S}\frac{\partial\tilde{C}_S}{\partial\tilde{t}} = \tilde{\nabla}^2\tilde{C}_S, \tag{5.11}$$

$$\tilde{C}_B(1,\tilde{t}) = \tilde{C}_S(1,\tilde{t}), \tag{5.12}$$

$$P\frac{D_B}{D_S}\frac{\partial\tilde{C}_B}{\partial\tilde{r}}\bigg|_1 = \frac{\partial\tilde{C}_S}{\partial\tilde{r}}\bigg|_1. \tag{5.13}$$

Two non-dimensional design parameters emerge: i) the partition coefficient P, and ii) the diffusivity ratio D_r between the beacon and solution phases,

$$D_r = \frac{D_B}{D_S}. \tag{5.14}$$

Three choices arise for the time scale τ_{SI}^0:

i) Intra-beacon diffusion time scale τ_B, required for solute profiles to reach quasi-steady state within the beacon, irrespective of what happens outside in solution,

$$\tau_B = \frac{R_B^2}{2\pi^2 D_B}; \tag{5.15}$$

ii) Solution diffusion time scale τ_S, required for solute profiles to reach quasi-steady state outside the beacon, irrespective of what happens inside,

$$\tau_S = \frac{R_B^2}{\pi^2 D_S}; \tag{5.16}$$

iii) Quasi-steady time scale τ_{QS}, described in our earlier work,[14] which arises when external mass transport is diffusion limited, yet strong partitioning ensures slow solute release,

$$\tau_{QS} = \frac{PR_B^2}{3D_S}. \tag{5.17}$$

We expect the longest of the three time scales to limit the dynamics of mass transport, and thus to set τ_{SI}^0.

5.1.1 SI dynamic regimes: Partitioning beacons

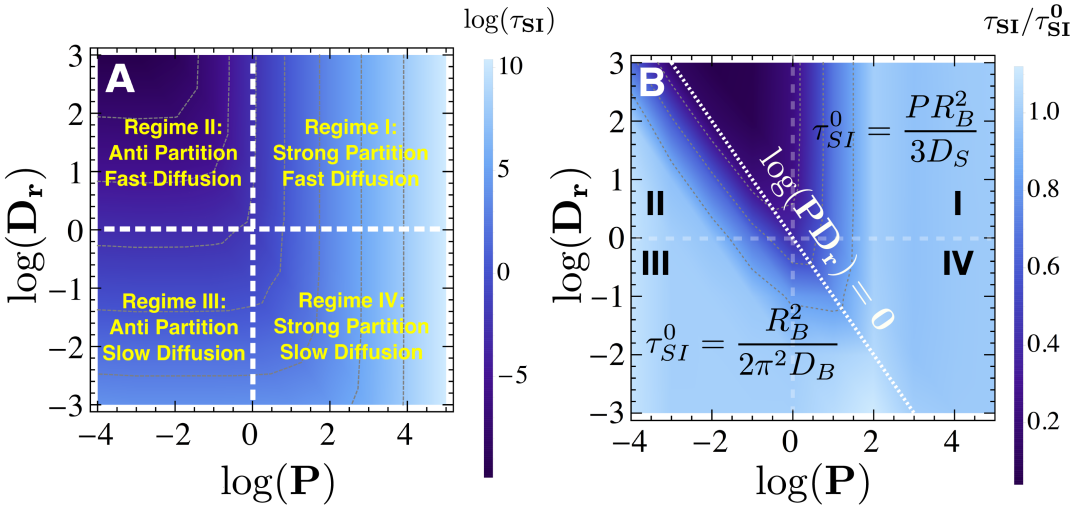

Figure 5.1: SI time, τ_{SI}, required for a partitioning beacon to unload solute, as a function of the partition coefficient P (Eq. 5.1) and diffusivity ratio D_r (Eq. 5.14). (A) Computed SI times required for beacon to unload 63% (1-1/e) of it's maximum initial concentration. Parameter space naturally divides into four qualitatively distinct solute transport regimes. (B) Scaling τ_{SI} in (A) by the combined SI time scale $\tau_{SI}^0 = \tau_{QS} + \tau_B$ (Eq. 5.18) collapses all data, except in regime II, which holds no interest for SI systems.

For brevity, we will explicitly discuss beacon sources that release solute, noting that beacon sinks that absorb solute obey identical governing equations (Eqs. 5.2 - 5.3) and boundary conditions (Eqs. 5.4 - 5.5), and hence follow similar mass transport dynamics.

To quantify the extended release property of beacons, we calculate the time required for them to release 63% (1-1/e) of their initial solute content and define it as the SI time, τ_{SI}. Figure 5.1 shows the computed SI times and the four qualitatively distinct regimes for solute transport that naturally emerge. Most promising for sustained solute release are strongly partitioning beacons ($P \gg 1$), for which solute diffusion may be limited externally ($D_r \gg 1$, regime I) or internally ($D_r \ll 1$, regime IV). Anti-partitioning ($P \ll 1$) may not seem promising, since solute molecules would prefer to be dissolved in the solution phase rather than the beacon phase, and hence leave the beacon quickly. However, sustained solute release is actually possible if intra-beacon diffusion is slow ($D_r \ll 1$, regime III). In regime II, beacons anti-partition solute ($P \ll 1$) and intra-beacon diffusion is fast ($D_r \gg 1$), which always leads to fast release. Thus, regime II is omitted from further consideration.

Regime	Condition	τ_{SI}	$\tilde{C}_B$	$\tilde{C}_S$
I	$PD_r \gg 1$ (Eq. 5.19)	$\frac{PR_B^2}{3D_S}$ (Eq. 5.17)	$\mathrm{e}^{-\tilde{t}}$ (Eq. 5.23)	$\frac{\mathrm{e}^{-\tilde{t}}}{\tilde{r}}$ (Eq. 5.24)
III	$PD_r \ll 1$ (Eq. 5.25)	$\frac{R_B^2}{2\pi^2 D_B}$ (Eq. 5.15)	$\frac{2}{\pi\tilde{r}}\sin(\pi\tilde{r})\mathrm{e}^{-\tilde{t}/2}$ (Eq. 5.28)	$2PD_r\frac{\mathrm{e}^{-\tilde{t}/2}}{\tilde{r}}$ (Eq. 5.30)
IV	$PD_r > 1$	$\frac{PR_B^2}{3D_S} + \frac{R_B^2}{2\pi^2 D_B}$	$\mathrm{e}^{-\tilde{t}}$	$\frac{\mathrm{e}^{-\tilde{t}}}{\tilde{r}}$
	$PD_r < 1$		$\frac{2}{\pi\tilde{r}}\sin(\pi\tilde{r})\mathrm{e}^{-\tilde{t}/2}$	$2PD_r\frac{\mathrm{e}^{-\tilde{t}/2}}{\tilde{r}}$

Table 5.1: Design summary of SI beacons that partition solute

Equations (5.15 - 5.17) describe time scales associated with various solute transport processes, with the longest among them limiting the dynamics of transport. Anticipating that systems of interest for SI interactions are limited by either strong partitioning or slow intra-beacon diffusion, we construct a combined time scale τ_{SI}^0, by combining τ_{QS}

(Eq. 5.17) and τ_B (Eq. 5.15)

$$\tau_{SI}^0 = \tau_{QS} + \tau_B = \frac{PR_B^2}{3D_S} + \frac{R_B^2}{2\pi^2 D_B}. \tag{5.18}$$

Scaling τ_{SI} in Fig. 5.1A by this combined time scale τ_{SI}^0 then collapses all computations, except in regime II (Fig. 5.1B).

In what follows, we derive approximate transport concentration profiles in the various regimes, with results summarized in Table 5.1.

Regime I – Strong partitioning, externally limited mass transport

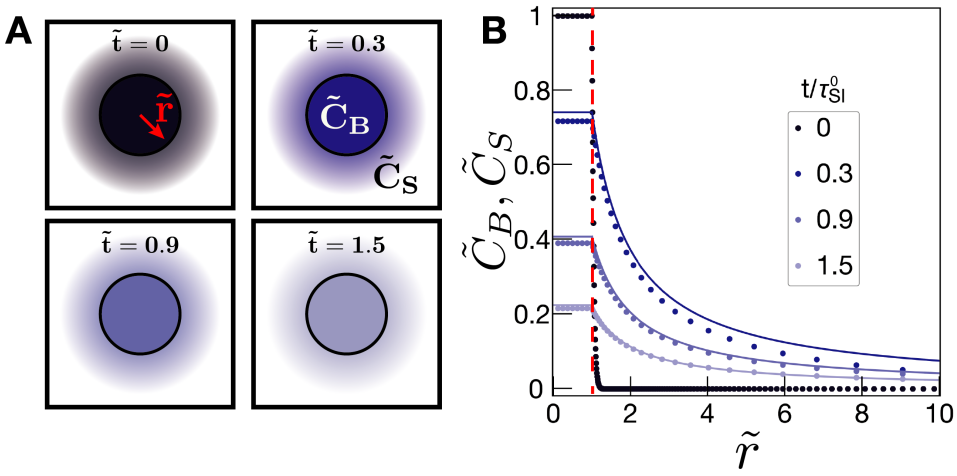

Figure 5.2: Partitioning beacons, regime I: Strong partitioning and fast internal diffusion. Concentration profiles inside ($\tilde{C}_B$) and outside ($\tilde{C}_S$) the beacon vs. radial distance from the center of the beacon at different times. (A) In this regime, solute concentrations inside the beacon are spatially uniform, with strong gradients outside in solution. (B) Computed profiles (points) and approximate analytical solutions (Eq. 5.23 and 5.24, lines) show no gradients in solute concentration inside the beacon and steep gradients outside. Computations performed with $P = 1000$ and $D_r = 1000$. Time is non-dimensionalized by $\tau_{SI}^0 \approx \tau_{QS} = PR_B^2/3D_S$ (Eq. 5.17).

Regime I corresponds to strongly partitioning beacons ($P \gg 1$), for which internal solute diffusion is fast ($D_r \gg 1$). Comparing the time scales from Eqs. (5.15 - 5.17)

reveals the quasi-steady time scale to be the slowest in this regime

$$\frac{\tau_{QS}}{\tau_B} = \frac{PR_B^2/3D_S}{R_B^2/2\pi^2 D_B} \approx PD_r \gg 1, \tag{5.19}$$

$$\frac{\tau_{QS}}{\tau_S} = \frac{PR_B^2/3D_S}{R_B^2/\pi^2 D_S} \approx P \gg 1, \tag{5.20}$$

and therefore, we assume $\tau_{SI}^0 \approx \tau_{QS}$. Here, the beacon concentration changes so slowly that concentration profiles within and outside the beacon reach quasi-steady state, and concentration gradients within the beacon can be neglected, $C_B(r,t) \sim C_B(t)$. Steady state diffusion in spherical coordinates further implies that solute profiles outside the beacon decay like $1/r$,

$$C_S(r,t) = \frac{C_B(t)}{P}\frac{R_B}{r}. \tag{5.21}$$

Balancing the diffusion limited outflux to the loss of solute from the beacon gives

$$\frac{4\pi R_B D_S C_B(t)}{P} = -\frac{d}{dt}\left[\frac{4}{3}\pi R_B^3 C_B(t)\right], \tag{5.22}$$

from which

$$C_B(t) = PC_0 \mathrm{e}^{-\frac{3D_S}{PR_B^2}t} \implies \tilde{C}_B = \exp(-\tilde{t}), \tag{5.23}$$

$$C_S(r,t) = C_0\frac{R_B}{r}\mathrm{e}^{-\frac{3D_S}{PR_B^2}t} \implies \tilde{C}_S = \frac{\exp(-\tilde{t})}{\tilde{r}}. \tag{5.24}$$

Computed concentration profiles (points) agree well with the analytical approximations (Eqs. 5.23 and 5.24, lines), as shown in Fig. 5.2.

Regime III – Anti-partitioning, internal diffusion limits mass transport

Regime III involves slow solute diffusion within the beacon ($D_r \ll 1$) and anti-partitioning between the beacon and solution ($P \ll 1$). The beacon diffusion time scale τ_B is the slowest amongst the three time scales (Eqs. 5.15 - 5.17), and is expected to limit SI unloading

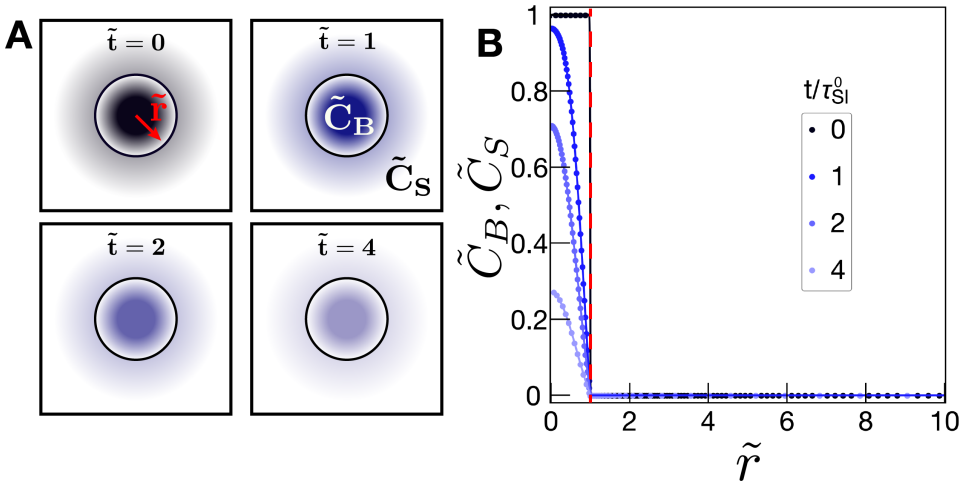

Figure 5.3: Partitioning beacons, regime III: Anti-partitioning and slow internal diffusion. Concentration profiles inside ($\tilde{C_B}$) and outside ($\tilde{C_S}$) the beacon, vs. radial distance from the center of the beacon at different times. (A) In this regime, solute concentration drops significantly within the beacon itself, with relatively weak gradients in solution. (B) Computations (points) and approximate analytical solutions (Eqs. 5.27 and 5.30, lines) show the large concentration gradients within the beacon and the weak gradients outside. Computations performed with $P = 0.001$ and $D_r = 0.001$. Time is non-dimensionalized by $\tau^0_{SI} \approx \tau_B = R_B^2/2\pi^2 D_B$ (Eq. 5.15).

$$\frac{\tau_{QS}}{\tau_B} = \frac{PR_B^2/3D_S}{R_B^2/2\pi^2 D_B} \approx PD_r \ll 1, \tag{5.25}$$

$$\frac{\tau_S}{\tau_B} = \frac{R_B^2/\pi^2 D_S}{R_B^2/2\pi^2 D_B} \approx D_r \ll 1. \tag{5.26}$$

We therefore assume $\tau^0_{SI} \approx \tau_B$. Since the beacon anti-partitions solute, we expect $C_S \ll C_B$. Moreover, intra-beacon diffusion is slow, which implies that almost the entire concentration drop occurs within the beacon. Thus, solving Eq. (5.2) with an approximate

boundary condition $C_B(R_B, t) = 0$ gives

$$\tilde{C}_B(\tilde{r}, \tilde{t}) = -\frac{2}{\tilde{r}} \sum_{n=1}^{\infty} \frac{(-1)^n}{n\pi} \sin(n\pi\tilde{r}) \exp\left(-\frac{n^2\tilde{t}}{2}\right), \tag{5.27}$$

which can be simplified at long times ($t > \tau_{SI}^0$) by simply retaining the slowest decaying eigenmode (n=1) to yield

$$\tilde{C}_B(\tilde{r}, \tilde{t}) \approx \frac{2}{\pi\tilde{r}} \sin \pi\tilde{r} \exp\left(-\frac{\tilde{t}}{2}\right). \tag{5.28}$$

Although the solution concentration C_S is small, DP migration is driven by solute gradients in solution. Therefore, to predict the DP velocity of particles generated by beacons in this regime, we must determine an approximate expression for C_S. The concentration profile outside the beacon evolves quasi-steadily as $1/r$, since internal mass transport is slow. The flux balance condition (Eq. 5.5) then gives

$$\tilde{C}_S(\tilde{r}, \tilde{t}) = -\frac{PD_r}{\tilde{r}} \left.\frac{\partial \tilde{C}_B}{\partial \tilde{r}}\right|_{\tilde{r}=1}. \tag{5.29}$$

From Eqs. (5.28) and (5.29), we obtain

$$\tilde{C}_S(\tilde{r}, \tilde{t}) \approx 2PD_r \frac{\exp(-\tilde{t}/2)}{\tilde{r}}. \tag{5.30}$$

Since P and D_r are both small in this regime, $\tilde{C}_S \propto PD_r$ is even smaller. Figure 5.3 shows good agreement between the approximate analytical solution (Eqs. 5.27 and 5.30, lines) and the full computed solution (points).

The DP migration velocity of particles is predicted[1,15] to obey

$$u_{DP} = D_{DP} \nabla \ln C_S, \tag{5.31}$$

where D_{DP} is the DP mobility of the particles. Equation (5.31) implies that even when ∇C_S is small, the DP velocity can be appreciable if C_S is also small. Therefore, observable DP colloidal migration may still be driven by SI beacons in this regime.

Regime IV – Strong partitioning, slow intra-beacon diffusion

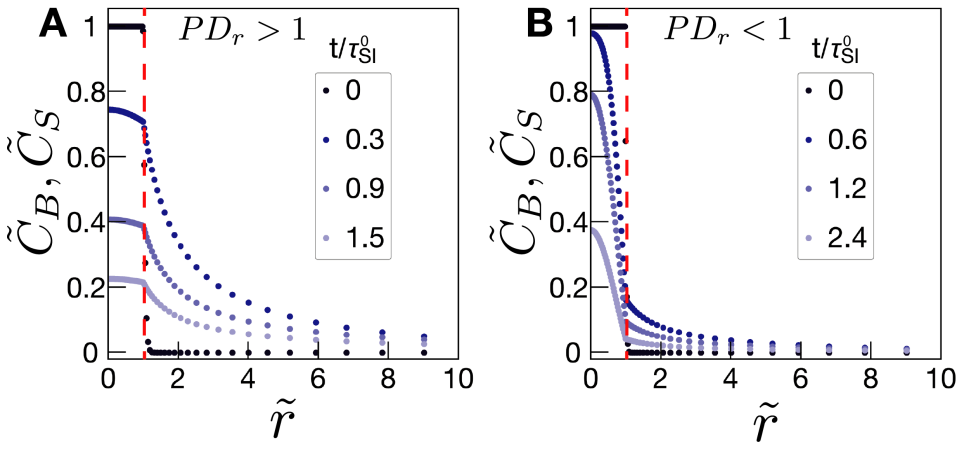

Figure 5.4: Partitioning beacons, regime IV: Strong partitioning and slow internal diffusion. Concentration profiles inside ($\tilde{C_B}$) and outside ($\tilde{C_S}$) the beacon vs. radial distance from the center of the beacon at different time steps. (A) When $PD_r > 1$, concentration profiles resemble those of regime I (Fig. 5.2), where diffusion is externally limited. (B) However, when $PD_r < 1$, internal transport is limiting and profiles look like those of regime III (Fig. 5.3). Time is scaled by $\tau^0_{SI} = \tau_{QS} + \tau_B$. Computations in (A) performed with $P = 1000$ and $D_r = 0.01$, whereas computations in (B) performed with $P = 100$ and $D_r = 0.001$. Time is non-dimensionalized by $\tau^0_{SI} = PR_B^2/3D_S + R_B^2/2\pi^2 D_B$ (Eq. 5.18).

In regime IV, solute partitioning in the beacon is strong like in regime I; however, internal diffusion is slow like in regime III. Mass transport limitations depend upon which process is the slowest. A flux balance across the beacon-solution interface reveals the time scale for SI unloading in this regime.

Under the quasi-steady state approximation, the solute concentration profile outside the beacon can be expressed as

$$C_S = \frac{C_B^i}{P}\frac{R_B}{r}, \tag{5.32}$$

where C_B^i is solute concentration at the beacon interface. The diffusive solute flux leaving the beacon,

$$J_S = D_S \frac{C_B^i}{PR_B}, \tag{5.33}$$

is balanced by a flux within the beacon,

$$J_B \approx D_B \frac{C_B^0 - C_B^i}{R_B}, \tag{5.34}$$

where C_B^0 is the concentration at the center of the beacon. Equating these two fluxes yields

$$C_B^i \approx C_B^0 \left(\frac{PD_r}{1 + PD_r} \right). \tag{5.35}$$

Balancing the loss of solute to the diffusion limited outflux from the beacon (Eq. 5.33), gives

$$\frac{4}{3}\pi R_B^3 \frac{dC_B^0}{dt} \approx -4\pi R_B^2 \frac{D_S C_B^i}{PR_B}. \tag{5.36}$$

Approximating $C_B^0 \propto \mathrm{e}^{-t/\tau_{SI}^0}$ leads to

$$\frac{R_B^2 C_B^0}{3\tau_{SI}^0} = \frac{D_S C_B^i}{P} \tag{5.37}$$

which ultimately results in

$$\tau_{SI}^0 \approx \frac{PR_B^2}{3D_S} \left(1 + \frac{1}{PD_r} \right) = \tau_{QS} + \tau_B 2\pi^2. \tag{5.38}$$

Two extremes of τ_{SI}^0 then emerge from Eq. (5.38). Internal solute diffusion is rate limiting when $PD_r \ll 1$, in which case

$$\tau_{SI}^0 \approx \frac{PR_B^2}{3D_S} \frac{1}{PD_r} \approx \frac{R_B^2}{D_B} \approx \tau_B, \tag{5.39}$$

as in regime III. Very strong partitioning ($PD_r \gg 1$), on the other hand, gives the quasi-steady time scale like in regime I,

$$\tau_{SI}^0 \approx \frac{PR_B^2}{3D_S} = \tau_{QS}. \tag{5.40}$$

Intermediate examples (i.e. regions with $PD_r < 1$ or $PD_r > 1$) are shown in Fig. 5.4.

5.1.2 Particle velocity near beacon sources and sinks

Solute gradients can be generated in solution by both beacon sources that release solute, and beacon sinks that absorb solute. Because sources and sinks are governed by the same mass transport equations, τ_{SI}^0 does not discriminate between solute loading or unloading. The resulting DP velocities in suspension, however, differ dramatically for these two situations, because DP velocities do not vary linearly in ∇C_S, but instead scale with $\nabla \ln C_S$.

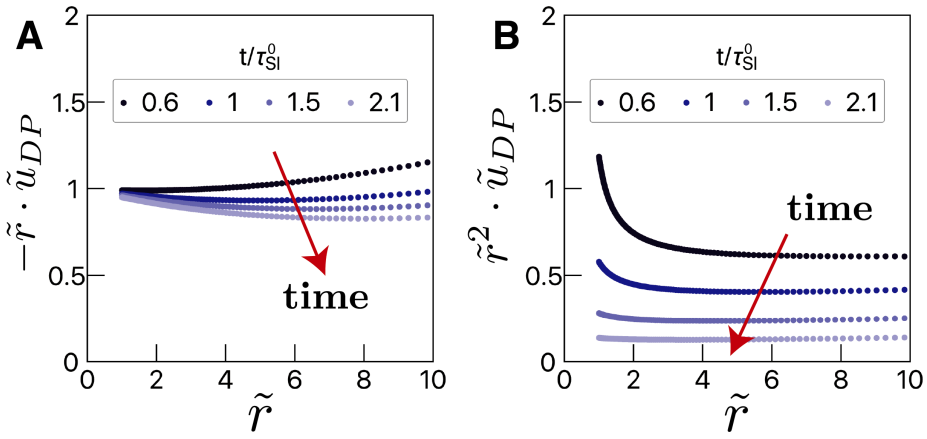

Figure 5.5: Diffusiophoretic velocity of particles driven by beacon (A) sources vs. (B) sinks in regime I. (A) The SI migration driven by sources decays like $\tilde{r}^{-1}$ (Eq. 5.43). By contrast, velocities generated by SI sinks decay more rapidly in space ($\tilde{r}^{-2}$) and exponentially in time (Eq. 5.45).

Regime I beacons that strongly partition solute highlight these differences. The

concentration outside a beacon source evolves according to (Eq. 5.24),

$$\tilde{C}_S^{\text{source}} = \frac{\exp(-\tilde{t})}{\tilde{r}}, \tag{5.41}$$

yet beacon sinks establish

$$\tilde{C}_S^{\text{sink}} = 1 - \frac{1}{\tilde{r}}\exp(-\tilde{t}). \tag{5.42}$$

The particle DP velocities driven by regime I beacon sources and sinks can then be evaluated using Eq. (5.31). SI sources drive DP velocities

$$\tilde{u}_{DP}^{\text{source}}(\tilde{r}) = -\frac{1}{\tilde{r}}, \tag{5.43}$$

whereas beacon sinks drive

$$\tilde{u}_{DP}^{\text{sink}}(\tilde{r},\tilde{t}) = \frac{1}{\tilde{r}^2}\frac{\exp(-\tilde{t})}{1-\frac{1}{\tilde{r}}\exp(-\tilde{t})}. \tag{5.44}$$

In both cases, u_{DP} is non-dimensionalized by D_{DP}/R_B.

One can immediately draw a striking contrast between the u_{DP} expressions for sources (Eq. 5.43) and sinks (Eq. 5.44). At large times ($t > \tau_{SI}^0$), SI migration around SI sinks decays exponentially (Fig. 5.5B) via

$$\tilde{u}_{DP}^{\text{sink}}(\tilde{r},\tilde{t}>1) = \frac{\exp(-\tilde{t})}{\tilde{r}^2}, \tag{5.45}$$

whereas SI interactions around SI source beacons show no apparent temporal dependence (Fig. 5.5A, Eq. 5.43). Moreover, DP velocities for SI beacon sinks decay more quickly in space ($\tilde{r}^{-2}$, Fig. 5.5B) than beacon sources ($\tilde{r}^{-1}$, Fig. 5.5A).

In regime III, where mass transport is limited internally, u_{DP} decays even faster for beacon sinks because most of the solute concentration drops across the beacon. Thus, gradients in solution are weak while background concentrations are high. Since u_{DP} scales as $\nabla C_S/C_S$, DP velocities for such sinks become vanishingly small. On the other hand, strong velocities can still be obtained with beacon sources in this regime, since small gradients are accompanied by small concentrations in solution, and ratios of ∇C_S to C_S remain appreciable. A greater flexibility in material selection can hence be achieved with beacon sources (either regime I or III), whereas materials for effective beacon sinks require rapid internal mass transport that is only realized in regime I.

5.2 SI beacons that associate with solute

The second class of beacons involves materials with high surface to volume ratio that associate with particular solutes, and therefore can store solute via adsorption. These materials include polymer hydrogels,[16] mesoporous silica particles,[17] and supraparticles.[18] The solute molecules associate with the beacon material with association constant K; the greater the value of K, the higher is the beacon's solute capacity.

Here, we model the mass transport within these porous beacon materials assuming linear adsorption-desorption kinetics, $\mathrm{C_{free}} \underset{\mathrm{k_{-1}}}{\overset{\mathrm{k_1}}{\rightleftharpoons}} \mathrm{C_{ads}}$, where C_{free} and C_{ads} are the concentrations of the free (unbound) and adsorbed species, respectively. k_1 and k_{-1} are the rates of adsorption and desorption, respectively, and the association constant is defined as

$$K = \frac{k_1}{k_{-1}}. \tag{5.46}$$

The concentration of free and adsorbed solute species within the beacon evolves

according to

$$\frac{dC_{\text{ads}}}{dt} = k_1 C_{\text{free}} - k_{-1} C_{\text{ads}}, \tag{5.47}$$

$$\frac{\partial C_{\text{free}}}{\partial t} = \frac{D_{\text{free}}}{r^2}\frac{\partial}{\partial r}\left(r^2 \frac{\partial C_{\text{free}}}{\partial r}\right) + k_{-1} C_{\text{ads}} - k_1 C_{\text{free}}. \tag{5.48}$$

The adsorbed molecules are bound to the beacon material and hence do not diffuse, while the free solute molecules diffuse with a diffusivity D_{free}. The solute transport in solution obeys Eq. (5.3). Diffusion of solute within these porous materials is usually slower than the diffusion in bulk solution due to the tortuous diffusion path.[19,20] To that end, and to reduce the complexity of the design space, the ratio of free solute diffusivity in the beacon and in solution is assumed to be small

$$D_r = \frac{D_{\text{free}}}{D_S} \ll 1. \tag{5.49}$$

The boundary conditions at the beacon-solution interface ($r = R_B$) are

$$C_{\text{free}}(R_B, t) = C_S(R_B, t), \tag{5.50}$$

$$D_{\text{free}} \left.\frac{\partial C_{\text{free}}}{\partial r}\right|_{R_B} = D_S \left.\frac{\partial C_S}{\partial r}\right|_{R_B}. \tag{5.51}$$

For a beacon source unloading solute, the following initial conditions hold

$$C_{\text{free}}(r \leq R_B,\ t = 0) = C_0, \tag{5.52}$$

$$C_{\text{ads}}(r \leq R_B,\ t = 0) = K C_0, \tag{5.53}$$

while for a beacon sink loading solute, the initial conditions are

$$C_{\text{free}}(r \leq R_B,\ t = 0) = 0, \tag{5.54}$$

$$C_{\text{ads}}(r \leq R_B,\ t = 0) = 0. \tag{5.55}$$

The initial condition for solute concentration in solution is given by Eqs. (5.7) and (5.9) for solute unloading (source) and loading (sink), respectively. Non-dimensionalizing Eqs. (5.47 – 5.51) with $C_{\text{free}} = C_0\tilde{C}_{\text{free}},\ C_{\text{ads}} = KC_0\tilde{C}_{\text{ads}},\ C_S = C_0\tilde{C}_S,\ r = R_B\tilde{r},$ and $t = \tau^0_{SI}\tilde{t}$, gives

$$\frac{K}{\tau^0_{SI}k_1}\frac{\partial\tilde{C}_{\text{ads}}}{\partial\tilde{t}} = \tilde{C}_{\text{free}} - \tilde{C}_{\text{ads}}, \tag{5.56}$$

$$\frac{R_B^2}{\tau^0_{SI}D_{\text{free}}}\frac{\partial\tilde{C}_{\text{free}}}{\partial\tilde{t}} = \tilde{\nabla}^2\tilde{C}_{\text{free}} + \frac{k_1R_B^2}{D_{\text{free}}}(\tilde{C}_{\text{ads}} - \tilde{C}_{\text{free}}), \tag{5.57}$$

$$\tilde{C}_{\text{free}}(1,\tilde{t}) = \tilde{C}_S(1,\tilde{t}), \tag{5.58}$$

$$\frac{D_{\text{free}}}{D_S}\frac{\partial\tilde{C}_{\text{free}}}{\partial\tilde{r}}\bigg|_1 = \frac{\partial\tilde{C}_S}{\partial\tilde{r}}\bigg|_1. \tag{5.59}$$

Two non-dimensional design parameters emerge: i) the association constant K, and ii) the Damköhler number,

$$Da = \frac{k_1R_B^2}{D_{\text{free}}}, \tag{5.60}$$

which expresses the relative rates of solute adsorption k_1, and diffusion D_{free}/R_B^2.

Three time scales (τ^0_{SI}) are relevant in these systems:

i) An effective diffusion time scale τ_B^{eff}, required for solute profiles inside the beacon to reach steady state when adsorption-desorption equilibration is rapid, such that $C_{\text{ads}} =$

KC_{free}. Adding Eqs. (5.47) and (5.48), and using this equilibrium condition reveals

$$\frac{\partial C_{\text{free}}}{\partial t} = \frac{D_{\text{free}}}{1+K}\frac{1}{r^2}\frac{\partial}{\partial r}\left(r^2\frac{\partial C_{\text{free}}}{\partial r}\right), \tag{5.61}$$

which implies that solute diffuses within the beacon with an effective diffusion coefficient[21]

$$D_{\text{eff}} = \frac{D_{\text{free}}}{1+K}. \tag{5.62}$$

The effective diffusion time scale τ_B^{eff} is therefore given by

$$\tau_B^{\text{eff}} = \frac{R_B^2}{2\pi^2 D_{\text{eff}}} = \frac{R_B^2(1+K)}{2\pi^2 D_{\text{free}}} = (1+K)\tau_B. \tag{5.63}$$

ii) The adsorption time scale τ_{ads}, required for free solute molecules to adsorb onto the beacon,

$$\tau_{\text{ads}} = \frac{1}{k_1}; \tag{5.64}$$

iii) The desorption time, τ_{des}, required for the adsorbed solute species to desorb from the beacon,

$$\tau_{\text{des}} = \frac{1}{k_{-1}}. \tag{5.65}$$

Since solute diffusion in the bulk is considered to be fast compared to diffusion and desorption of solute within the beacon, we do not include the solution diffusion time scale, $\tau_S = R_B^2/\pi^2 D_S$, in our analysis. We expect the longest of the three time scales (Eq. 5.63 - 5.65) to limit the dynamics of solute transport, and therefore to set τ_{SI}^0.

5.2.1 SI dynamic regimes: Associating beacons

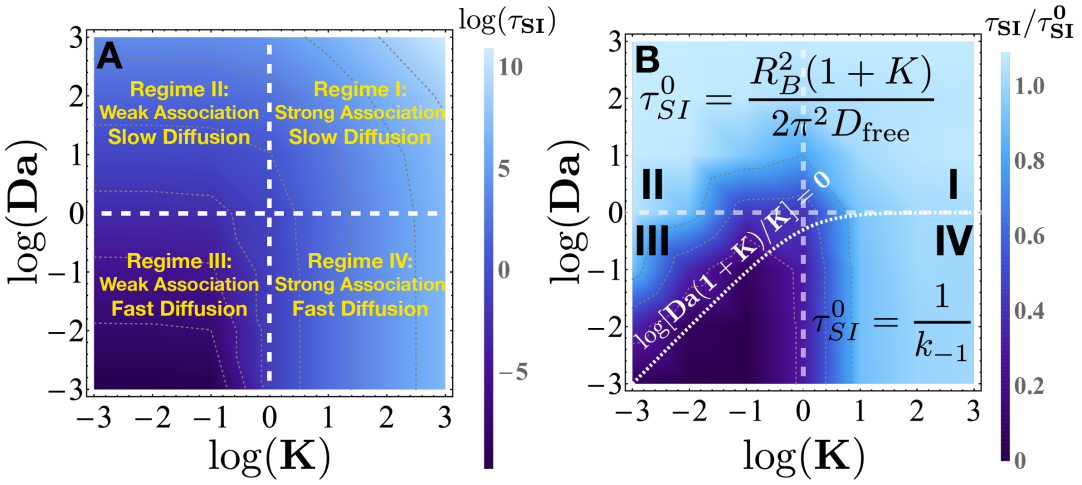

Figure 5.6: SI time, τ_{SI}, required for an associating beacon to unload solute, as a function of the association constant, K (Eq. 5.46) and the Damköhler number Da (Eq. 5.60). (A) Computed SI times required for beacon to unload 63% (1-1/e) of it's maximum initial concentration. Parameter space naturally divides into four qualitatively distinct solute transport regimes. (B) Scaling τ_{SI} in (A) by the combined SI time scale $\tau_{SI}^0 = \tau_{\text{des}} + \tau_B^{\text{eff}}$ (Eq. 5.66) collapses all data, except in regime III which holds no interest for SI systems.

We calculate the SI unloading time τ_{SI} for an associating beacon source that unloads solute, as a function of the association constant K (Eq. 5.46) and the Damköhler number Da (Eq. 5.60). Four distinct regimes for mass transport naturally emerge, with qualitatively distinct transport properties as shown in Fig. 5.6A. Most promising for sustained solute release are beacons that strongly associate with solute ($K \gg 1$), for which solute diffusion may be slow (regime I, $Da \gg 1$) or fast (regime IV, $Da \ll 1$). Although weakly associating beacons may not seem promising for sustained solute fluxes, long τ_{SI} may also be achieved when intra-beacon diffusion is slow (regime II, $Da \gg 1$). Regime III corresponds to weakly associating beacons ($K \ll 1$), for which solute diffusion is fast, giving beacons with low solute capacity. We therefore omit them from further consideration.

In each of these regimes, the longest of the three time scales τ_B^{eff} (Eq. 5.63), τ_{ads} (Eq.

5.64), and τ_{des} (Eq. 5.65) should govern the rate of solute transport. However, since SI unloading in the regimes considered here is either limited by internal diffusion or solute desorption from the beacon, and never by solute adsorption, we combine Eqs. (5.63) and (5.65) to obtain a general expression for the longest SI unloading time scale

$$\tau_{SI}^{0} = \tau_{\text{des}} + \tau_{B}^{\text{eff}} = \frac{1}{k_{-1}} + \frac{R_B^2(1+K)}{2\pi^2 D_{\text{free}}}. \tag{5.66}$$

Scaling τ_{SI} in Fig. 5.6A by this combined time scale collapses all data, except in regime III, as shown in Fig. 5.6B.

Regime	Condition	τ_{SI}	$\tilde{C}_{\text{free}}$	$\tilde{C}_{\text{ads}}$	$\tilde{C}_{\text{total}}$	$\tilde{C}_S$
I & II	$\frac{Da(1+K)}{K} \gg 1$ (Eq. 5.67)	$\frac{R_B^2(1+K)}{2\pi^2 D_{\text{free}}}$ (Eq. 5.63)	$\frac{2}{\pi\tilde{r}}\sin(\pi\tilde{r})\mathrm{e}^{-\tilde{t}/2}$ (Eq. 5.71)	$\tilde{C}_{\text{free}}$	$\tilde{C}_{\text{free}}$	$2D_r\frac{\mathrm{e}^{-\tilde{t}/2}}{\tilde{r}}$ (Eq. 5.72)
IV	$\frac{Da(1+K)}{K} \ll 1$ (Eq. 5.73)	$\frac{1}{k_{-1}}$ (Eq. 5.65)	≈ 0	$\mathrm{e}^{-\tilde{t}}$ (Eq. 5.75)	$\tilde{C}_{\text{ads}}$	$\frac{D_r Da}{3}\frac{\mathrm{e}^{-\tilde{t}}}{\tilde{r}}$ (Eq. 5.77)

Table 5.2: Design summary of SI beacons that associate with solutes

In what follows, we derive approximate solute concentration profiles in the various regimes, with results summarized in Table 5.2.

Regimes I and II: Intra-beacon solute diffusion slower than adsorption-desorption kinetics

Regimes I and II correspond to slow intra-beacon diffusion relative to adsorption-desorption. The Damköhler number is large in these systems ($Da \gg 1$), and the effective diffusion time scale (Eq. 5.63) is much greater than the adsorption (Eq. 5.64) and

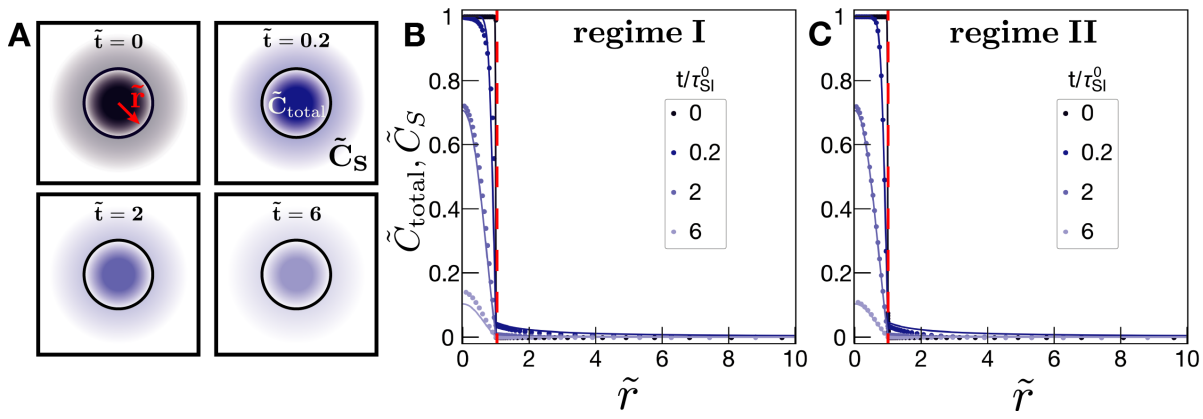

Figure 5.7: Associating beacons, regimes I and II: Internal solute diffusion is slower than adorption-desorption kinetics. Concentration profiles inside ($\tilde{C}_{\text{total}}$) and outside ($\tilde{C}_S$) the beacon vs. radial distance from the center of the beacon at different time steps. (A) In these regimes, solute concentration drops significantly within the beacon itself, with relatively weak gradients in solution. (B), (C) Concentration profiles computed numerically (points) and analytical approximations (Eq. 5.69 and 5.72, lines) show the strong gradients within the beacon and weak gradients outside, in regimes I and II respectively. Computations in (B) performed with $K = 100$, $Da = 100$, and $Dr = 0.01$, while computations in (C) performed with $K = 0.01$, $Da = 1000$, and $Dr = 0.01$. Time is non-dimensionalized by $\tau^0_{SI} \approx \tau^{\text{eff}}_B = R_B^2(1+K)/2\pi^2 D_{\text{free}}$ (Eq. 5.63).

desorption (Eq. 5.65) time scales,

$$\frac{\tau^{\text{eff}}_B}{\tau_{\text{des}}} = \frac{R_B^2(1+K)/2\pi^2 D_{\text{free}}}{1/k_{-1}} \approx \frac{Da(1+K)}{K} \gg 1, \tag{5.67}$$

$$\frac{\tau^{\text{eff}}_B}{\tau_{\text{ads}}} = \frac{R_B^2(1+K)/2\pi^2 D_{\text{free}}}{1/k_1} \approx Da(1+K) \gg 1. \tag{5.68}$$

We therefore expect τ^{eff}_B to limit the dynamics of SI unloading, and assume $\tau^0_{SI} \approx \tau^{\text{eff}}_B$. Since mass transport is diffusion-limited, adsorption-desorption is in quasi-equilibrium in these regimes, i.e. $\tilde{C}_{\text{ads}} = \tilde{C}_{\text{free}}$. Moreover, the rate limiting process of intra-beacon diffusion suggests that almost all concentration drops within the beacon. We therefore impose $C_{\text{free}}, C_{\text{ads}} \approx 0$ at the beacon boundary ($r = R_B$), in which case $\tilde{C}_{\text{free}}$ and $\tilde{C}_{\text{ads}}$ are

given by

$$\tilde{C}_{\text{free}} = \tilde{C}_{\text{ads}} = \tilde{C}_{\text{total}}(\tilde{r}, \tilde{t}) = -\frac{2}{\tilde{r}} \sum_{n=1}^{\infty} \left(\frac{(-1)^n}{n\pi} \right) \sin(n\pi\tilde{r}) \exp\left(-\frac{n^2 \tilde{t}}{2} \right). \tag{5.69}$$

C_{total} is the total beacon solute concentration, $C_{\text{total}} = C_{\text{free}} + C_{\text{ads}}$, which is normalized by $C_0 + KC_0$ to give

$$\tilde{C}_{\text{total}} = \frac{C_{\text{total}}}{C_0 + KC_0}. \tag{5.70}$$

Equation (5.69) can be further simplified at long times by keeping the slowest decaying eigenmode (n=1) to obtain

$$\tilde{C}_{\text{free}} = \tilde{C}_{\text{ads}} = \tilde{C}_{\text{total}}(\tilde{r}, \tilde{t}) \approx \frac{2}{\pi\tilde{r}} \sin \pi\tilde{r} \exp\left(-\frac{\tilde{t}}{2} \right). \tag{5.71}$$

Although solute concentration in solution C_S is small, because most of the concentration drops within the beacon, an approximate expression for C_S is required to predict DP velocity of particles. We therefore estimate C_S by assuming quasi-steady decay, and balancing the diffusive solute flux across the beacon interface ($r = R_B$) according to Eq. (5.51), to obtain

$$\tilde{C}_S(\tilde{r}, \tilde{t}) \approx 2D_r \frac{\exp(-\tilde{t}/2)}{\tilde{r}}. \tag{5.72}$$

Figure 5.7 compares the full computed concentration profiles (points) with the approximate analytical solutions (Eqs. 5.69, 5.72, lines).

Regime IV: Strong association, desorption limited mass transport

Regime IV involves strongly associating beacons ($K \gg 1$), for which intra-beacon diffusion is fast relative to adsorption-desorption ($Da \ll 1$). In this regime, the solute desorption time scale is rate limiting

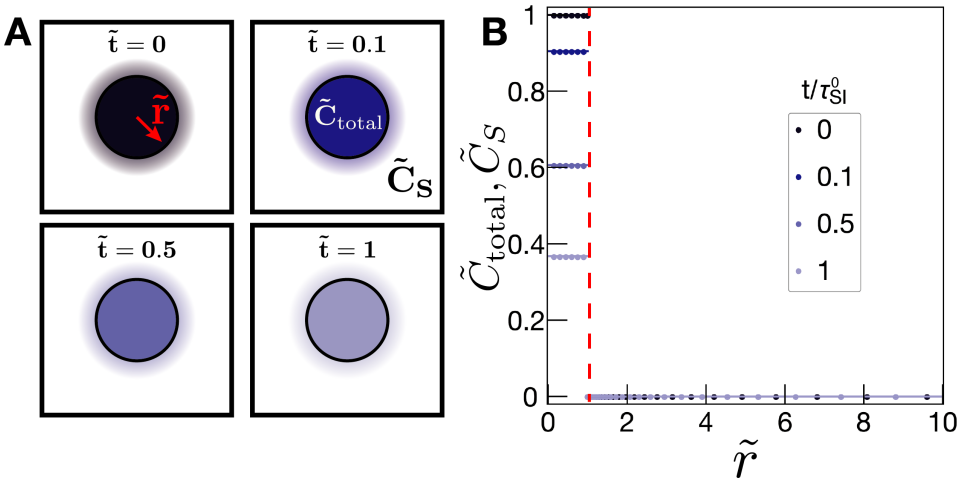

Figure 5.8: Associating beacons, regime IV: Fast internal diffusion, mass transport is solute desorption limited. Concentration profiles inside ($\tilde{C}_{\text{total}}$) and outside ($\tilde{C}_S$) the beacon vs. radial distance from the center of the beacon at different times. (A) In regime IV, solute concentration profiles are spatially uniform within the beacon, while concentrations outside in solution are small. (B) Profiles calculated numerically (points) and analytical approximations (Eqs. 5.75 and 5.77, lines) show the spatially uniform nature of the concentrations inside and small concentrations outside the beacon. Computations performed with $K = 1000$, $Da = 0.01$, and $D_r = 0.01$. Time is non-dimensionalized by $\tau^0_{SI} \approx \tau_{\text{des}} = 1/k_{-1}$ (Eq. 5.65).

$$\frac{\tau_B^{\text{eff}}}{\tau_{\text{des}}} = \frac{R_B^2(1+K)/2\pi^2 D_{\text{free}}}{1/k_{-1}} \approx \frac{Da(1+K)}{K} \ll 1, \tag{5.73}$$

$$\frac{\tau_{\text{ads}}}{\tau_{\text{des}}} = \frac{1/k_1}{1/k_{-1}} = \frac{1}{K} \ll 1, \tag{5.74}$$

and therefore, we assume $\tau^0_{SI} \approx \tau_{\text{des}}$. Rapid solute diffusion renders concentration profiles inside the beacon to be spatially uniform, $C_{\text{total}}(r,t) \sim C_{\text{total}}(t)$. In fact, $C_{\text{free}} \sim 0$ in this regime, since any solute molecule that desorbs from the beacon material quickly diffuses

away. Equation (5.47) then gives

$$\tilde{C}_{\text{ads}}(\tilde{t}) = \tilde{C}_{\text{total}}(\tilde{t}) = \exp(-\tilde{t}). \tag{5.75}$$

Since solute transport is limited by internal desorption, solution concentration profiles C_S outside the beacon evolve quasi-steadily. Balancing the diffusive outflux to the loss of solute from the beacon gives

$$4\pi R_B^2 D_S \frac{\partial C_S}{\partial r}\bigg|_{R_B} = \frac{\partial}{\partial t}\int_0^{R_B} 4\pi r^2 C_{\text{total}}(r,t)dr, \tag{5.76}$$

from which

$$\tilde{C}_S = \frac{D_r Da}{3}\frac{\exp(-\tilde{t})}{\tilde{r}}. \tag{5.77}$$

Figure 5.8 compares the approximate analytical solutions (Eqs. 5.75 and 5.77, lines) with numerical computations (points).

5.3 Discussion and Conclusion

Any SI application requires beacons to sustain solute fluxes. Additionally, the solute flux should also drive appreciable DP colloidal motion. Figure 5.9A shows a PEG-DA beacon sink absorbing SDS from solution that establishes long-lasting SDS flux, yet does not drive observable DP migration. This colloidal response to gradients generated by beacon sinks is in sharp contrast with the long-range migration driven by source beacons that emit SDS (Chapter 3, Fig. 3.3). We already noted in Section 5.1.2 (Eq. 5.43 and 5.44) that the nature of DP migration is sensitive to whether solute is loading or unloading. This system dependency is a consequence of the fact that DP velocities scale

with $\nabla C_S/C_S$, and not simply with ∇C_S. Thus, high background solute concentrations typically give weak DP velocities, as seen for SI sinks.

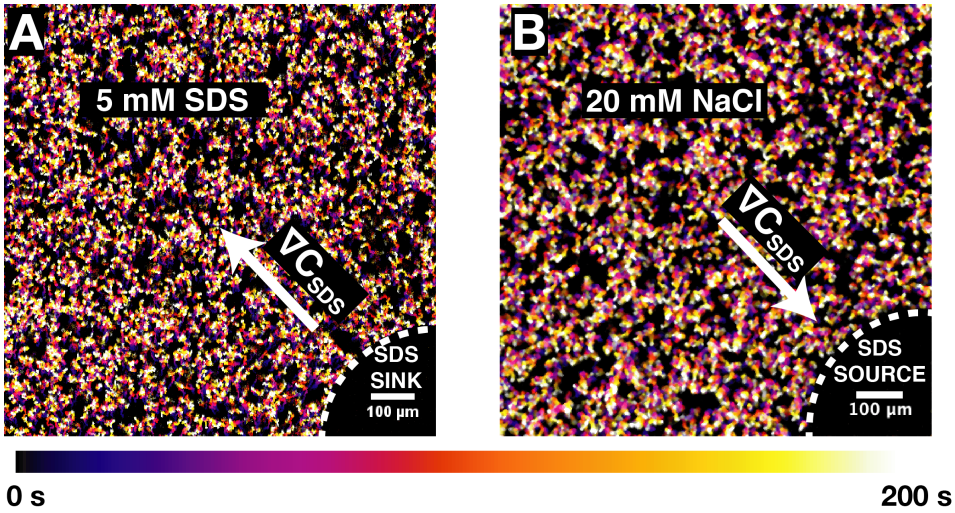

Figure 5.9: Ineffective SI strategies: High background concentrations suppress DP migration. (A) A PEG-DA beacon sink absorbing SDS shows no observable SI particle migration. (B) A PEG-DA beacon source unloading SDS into a 20 mM salt solution also fails to induce colloidal motion. In both cases, the absence of any detectable particle migration is evidenced by the streak lines that only show thermal fluctuations.

In fact, high background concentrations can also suppress SI migration driven by beacon sources. For example, Fig. 5.9B shows a PEG-DA beacon source unloading SDS into a 20 mM NaCl solution. Although negatively charged polystyrene (PS) particles are expected to migrate away from SDS sources, as in Fig. 3.3,[14,22] the added background salt suppresses the DP migration. Therefore, while long SI times τ_{SI} are necessary for effective SI interactions over sustained durations, appreciable DP mobilities are also required.

Selecting an appropriate beacon - solute combination is critical for designing soluto-inertial suspension interactions that extend over long range, and that last for sustained durations. Here, we carefully examined the design space for two such beacon material choices: beacons that partition solute or that associate with solute. By mapping parameter space, we identified the limiting mass transport processes in the distinct regimes, from which we derived simple analytical expressions for the evolution of solute concentration

profiles in solution. These expressions led to intuitive yet predictive approximations for the diffusiophoretic velocity profiles of particles driven by such beacons. The strategy outlined here yields a general framework that will allow users to navigate parameter space for particular systems of interest, and therefore to select appropriate materials to design these novel interactions.

Acknowledgements

Douglas Vogus is a co-author on this work. We gratefully acknowledge support from the American Chemical Society Petroleum Research Foundation (Grant 54141-ND5), National Science Foundation (Grant CBET-1438779) and the Saudi Arabian Oil Company (Saudi Aramco, Contract A-0002-2018). Any opinion, findings, and conclusions or recommendations expressed in this material are those of the authors and do not necessarily reflect the views of the National Science Foundation. A portion of this work was performed in the Microfluidics Laboratory within the California NanoSystems Institute, supported by the University of California, Santa Barbara and the University of California, Office of the President, and in the Shared Experimental Facilities of the Materials Research Science and Engineering Center at UCSB (MRSEC NSF DMR 1720256).

Bibliography

[1] Derjaguin BV, Dukhin SS, Korotkova AA. Diffusiophoresis in electrolyte solutions and its role in the Mechanism of the formation of films from caoutchouc latexes by the ionic deposition method. *Progress in Surface Science.* 1993; 43(20): 153–158.

[2] Prieve DC. Migration of a colloidal particle in a gradient of electrolyte concentration. *Advances in Colloid and Interface Science.* 1982; 16: 321–335.

[3] Prieve DC, Anderson JL, Ebel JP, Lowell ME. Motion of a particle generated by chemical gradients. Part 2. Electrolytes. *Journal of Fluid Mechanics.* 1984; 148: 247.

[4] Anderson JL. Colloid transport by interfacial forces. *Ann. Rev. Fluid Mech..* 1989; 21: 61–99.

[5] McDermott JJ, Kar A, Daher M, et al. Self-generated diffusioosmotic flows from calcium carbonate micropumps. *Langmuir.* 2012; 28: 15491–15497.

[6] Shin S, Shardt O, Warren PB, Stone HA. Membraneless water filtration using CO 2. *Nature Communications.* 2017; 8(May): 1–6.

[7] Florea D, Musa S, Huyghe JMR, Wyss HM. Long-range repulsion of colloids driven by ion exchange and diffusiophoresis. *Proceedings of the National Academy of Sciences of the United States of America.* 2014; 111(18): 6554–9.

[8] Niu R, Botin D, Weber J, Reinmüller A, Palberg T. Assembly and speed in ion-exchange-based modular phoretic microswimmers. *Langmuir.* 2017; 33(14): 3450-3457. PMID: 28346787.

[9] Guha R, Mohajerani F, Mukhopadhyay A, Collins MD, Sen A, Velegol D. Modulation of spatiotemporal particle patterning in evaporating droplets: Applications to diagnostics and materials science. *ACS Applied Materials & Interfaces.* 2017; 9(49): 43352-43362. PMID: 29143530.

[10] Velegol D, Garg A, Guha R, Kar A, Kumar M. Origins of concentration gradients for diffusiophoresis. *Soft Matter.* 2016; 12: 4686–4703.

[11] Leo A, Hansch C, Elkins D. Partition coefficients and their uses. *Chemical Reviews.* 1971; 71(6): 525.

[12] Dunn W, Block J, Pearlman R, Association AP, Pharmaceutical Sciences A. *Partition coefficient: determination and estimation.* Pergamon Press 1986.

[13] Sangster J. Octanol-water partition coefficients of simple organic compounds. *Journal of Physical and Chemical Reference Data.* 1989; 18(3): 1111-1229.

[14] Banerjee A, Williams I, Azevedo RN, Helgeson ME, Squires TM. Soluto-inertial phenomena: Designing long-range, long-lasting, surface-specific interactions in suspensions. *Proceedings of the National Academy of Sciences.* 2016; 113(31): 8612-8617.

[15] Anderson JL, Lowell ME, Prieve DC. Motion of a particle generated by chemical gradients Part 1. Non-electrolytes. *Journal of Fluid Mechanics.* 1982; 117: 107–121.

[16] Ahmed EM. Hydrogel: Preparation, characterization, and applications: A review. *Journal of Advanced Research.* 2015; 6(2): 105 - 121.

[17] Zhao D, Feng J, Huo Q, et al. Triblock copolymer syntheses of mesoporous silica with periodic 50 to 300 angstrom pores. *Science.* 1998; 279(5350): 548–552.

[18] Wintzheimer S, Granath T, Oppmann M, et al. Supraparticles: Functionality from uniform structural motifs. *ACS Nano.* 2018; 12(6): 5093-5120. PMID: 29763295.

[19] Amsden B. Solute diffusion within hydrogels. mechanisms and models. *Macromolecules.* 1998; 31(23): 8382-8395.

[20] Amsden B. Solute diffusion in hydrogels.: An examination of the retardation effect. *Polymer Gels and Networks.* 1998; 6(1): 13 - 43.

[21] Cussler EL. *Diffusion: Mass Transfer in Fluid Systems.* Cambridge Series in Chemical EngineeringCambridge University Press3 ed. 2009.

[22] Nery-Azevedo R, Banerjee A, Squires TM. Diffusiophoresis in Ionic Surfactant Gradients. *Langmuir.* 2017(1).

Chapter 6

Drop in "additives" for suspension manipulation: Sedimenting beacons

Our efforts thus far were focused on fixed cylindrical beacons that initiate and sustain colloidal migration in well-controlled microfluidic geometries (Fig. 6.1A,B). Here, we show SI interactions within 3D, bulk suspensions driven by spherical beacon additives. Due to their macroscopic size [$\mathcal{O}(100\ \mu\text{m})$] and relative density, these beacons sediment within the suspension. As the beacon falls, it establishes a convection-diffusion boundary layer that creates a trailing solute wake (Fig. 6.1C,D). Solute within the wake subsequently diffuses out radially, creating a concentration gradient that initiates DP migration of suspended objects (Fig. 6.1E,F).

The sign of the interaction (i.e. attraction or repulsion) depends upon the interactions between the solute and the surface chemistry of the colloid. If the solute-particle interaction is attractive, DP drives particles towards the wake, creating a region that is enriched in colloids, so that particle concentration in the wake N_{SI} exceeds the background concentration N_0. On the other hand, repulsive solute-particle interactions drive DP away from the wake, and thus create a depletion region in the suspension ($N_{SI} < N_0$).

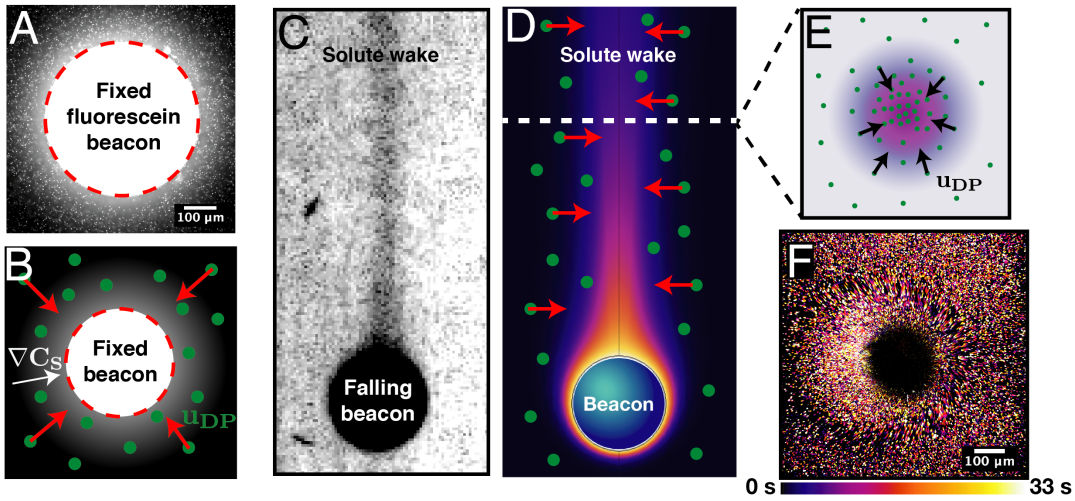

Figure 6.1: Freely falling SI beacons induce diffusiophoretic colloidal migration. (A) Fixed cylindrical beacon post establishes a radial concentration profile of a solute (fluorescein in this case), inside a microfluidic device. (B) The solute gradient drives radial DP migration of suspended colloids. (C) Experimental and (D) computational visualization of a sedimenting beacon that emits solute within a convection-diffusion boundary layer ahead of the beacon, and forming a solute wake behind. The experiment (C) comprises of a water drop unloading Oil Red O dye as it sediments through an oil bath. (E) As the solute in the wake diffuses radially outward, its concentration gradients drive suspended particles to migrate towards (or away) from the wake, creating regions in the suspension that are enriched in (or devoid of) particles. (F) Experimental demonstration of colloidal attraction and accumulation driven by the wake of a sedimenting beacon. The color-coded streak lines near the center of the wake show the direction of the diffusiophoretic migration towards the center.

We envision such bulk colloidal response to beacon additives to potentially open new ways to flocculate dilute suspensions on-demand where aggregation is diffusion limited,[1] concentrate analyte/antibody solutions for rapid bioassays and clarify oil from emulsions (eg. in biofuel production).

The chapter is structured as follows: first, we present an experimental realization of colloidal motion generated by the trailing solute wake of a sedimenting beacon. We compare two cases where the wake attracts or repels particles. Next, we present a general theory to describe the phenomenon and provide scaling arguments that capture the effect of the falling velocity and the beacon size on the mass of solute left behind in the wake.

Finally, we identify the design parameters that govern the particle response to the solute flux emanating from the wake, and map out parameter space with the goal of facilitating easy prediction of behavior.

6.1 Experiments

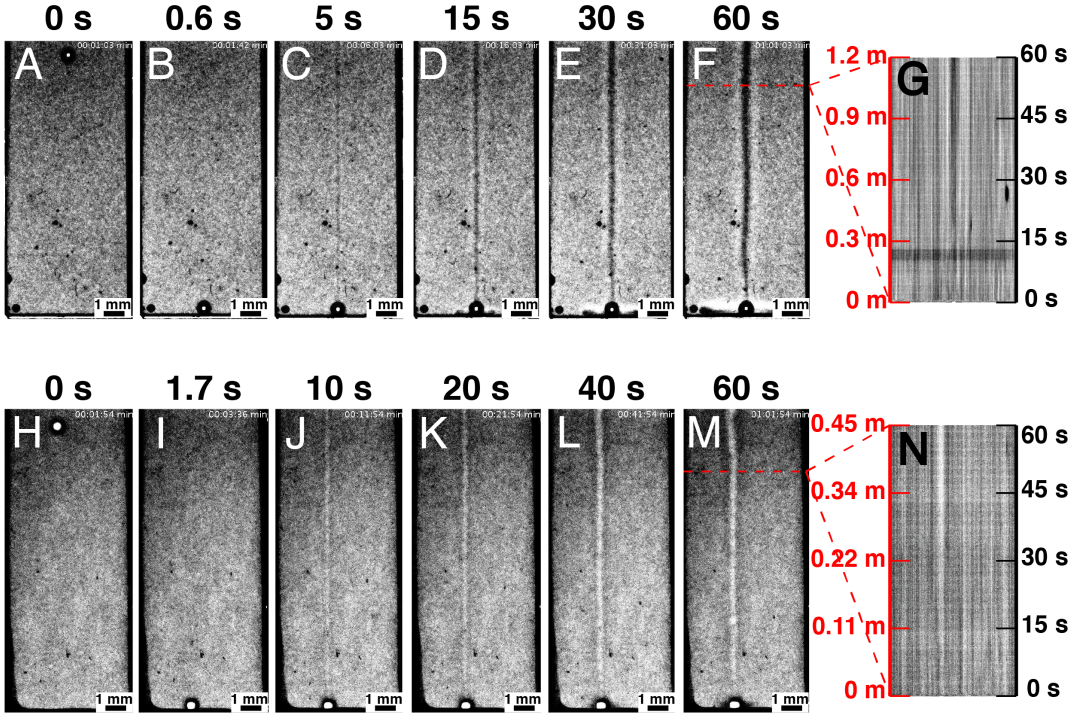

Figure 6.2: Falling beacons loaded with [C_4mim][I] and SDS create wakes that attract and repel particles, respectively. Images show six snapshots in time for the two different beacons – (A) the [C_4mim][I] beacon falls down at t=0 s and (B) hits the bottom of the container after 0.6 s; the wake diffuses out and collects particles, as seen after (C) 5 s, (D) 15 s, (E) 30 s, and (F) 60 s. (G) A pixel thick slice (at z = 11.5 mm), when stacked together, shows the temporal evolution of the particle concentration in the wake. The axis on the right shows the time elapsed after the beacon crosses the dashed red line in (F) and the axis on the left shows the distance the beacon would have fallen had the fluid been unbounded. (H) On the other hand, the SDS beacon falls down at t=0 s and (I) hits the bottom of the container after 1.7 s; here, however, the wake repels particles to create a depletion zone, as seen after (J) 10 s, (K) 20 s, (L) 40 s, and (M) 60 s. (N) A pixel thick slice (at z = 9 mm), when stacked together, shows the temporal evolution of the particle concentration in the wake. The axes on the left and right have the same interpretation as (G).

Experiments are performed with two distinct kinds of beacons – ionogel beacons that are loaded with the ionic liquid 1-n-butyl-3-methylimidazolium iodide ([C_4mim][I]) and beacons loaded with the surfactant sodium dodecyl sulfate (SDS). Our previous work showed beacons releasing [C_4mim][I] attract negatively charged colloids, whereas beacons emitting SDS repel them (Chapter 4). Figure 6.2A-F shows a 0.5 mm diameter ionogel beacon that sediments 12 mm in approximately 0.6 seconds, whose [C_4mim][I] wake attracts particles, creating a region where particle concentration exceeds the background concentration ($N_{SI} > N_0$). Images represent transmitted light, meaning that dark regions indicate higher particle concentration in the suspension and vice versa. Figure 6.2G shows the temporal evolution of the particle concentration in the suspension at a single position, 11.5 mm from the bottom of the sample cell, by stacking the line of pixels from each time. The axis on the right (black) shows the time elapsed after the beacon crosses the red dashed line (at 11.5 mm) in Fig. 6.2F. The axis on the left (red) shows the distance that the sedimenting ionogel beacon would have covered, had it continued to fall at its steady velocity of approximately 20 mm/s in an unbounded fluid.

Figure 6.2H-M shows a 0.5 mm diameter PEG-DA beacon loaded with SDS, which sediments more slowly (12.75 mm in approximately 1.7 seconds) due to its lower density. As expected, particles are repelled from the SDS wake, as indicated by the brighter streak in the center. Stacking slices as before shows the particle distribution vs time at a single position, 9 mm from the bottom of the sample cell (Fig. 6.2N). The axes on the left and right have the same meaning as Fig. 6.2G, albeit the axis on the left corresponds to the distance covered by the SDS beacon, sedimenting at a velocity of 7.5 mm/s in an unbounded fluid.

Figure 6.3A shows the particle concentration profile evolving in response to the [C_4mim][I] wake. Measured intensities represent a projected or apparent concentration profile, since the radially symmetric concentration profile is imaged from the side. The

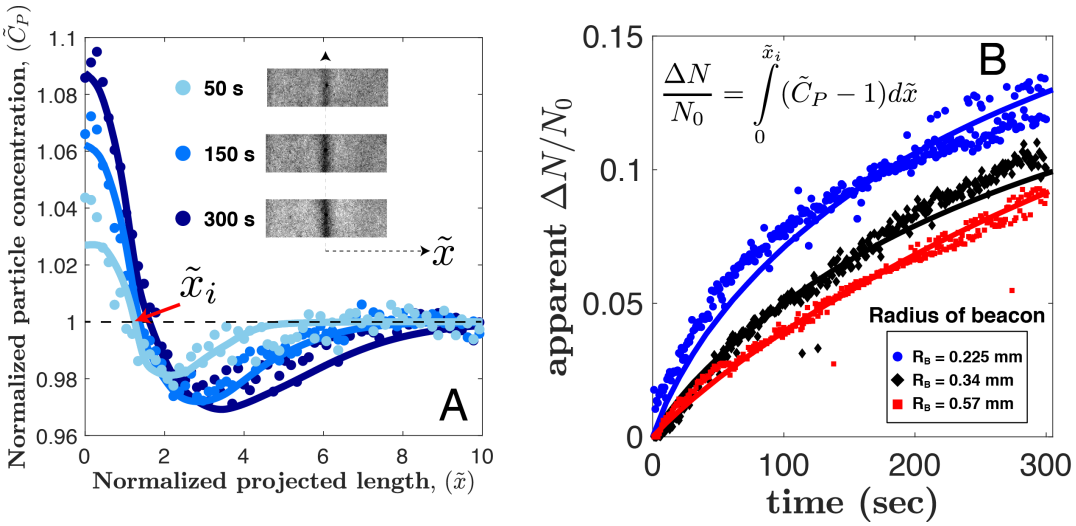

Figure 6.3: Particle attraction and accumulation by the wake of a falling ionogel beacon. (A) 1D projection of the particle concentration profile at different times. Profiles correspond to a beacon with $R_B = 0.225$ mm. (B) Apparent increase in the number of particles collected in the wake vs time for three different beacon sizes. Points show experimental data while lines represent results from numerical computations.

particle response to the $[C_4mim][I]$ flux is as expected – the attractive solute-particle interaction causes the colloids to accumulate at the center. However, since no new particles are created, mass conservation requires that the excess particles in the center be supplied by the neighboring regions of the suspension. This population balance leads to particle depletion right next to the excess, with a crossover at location x_i. Far from the wake, the bulk particle concentration is recovered. Experimental measurements (points) agree well with concentration profiles (lines) predicted from theory, details of which are presented later.

Particle collection over time in the "excess region" (N_{SI}) behind ionogel beacons of three different radii are compared in Fig. 6.3B. Specifically, we integrate the excess apparent particle concentration $\Delta N = N_{SI} - N_0$, across the excess region, and normalize

by the number of "background" colloids that would be swept by the sedimenting beacon.

$$\left.\frac{\Delta N}{N_0}\right|_{\text{apparent}} = \frac{\int_0^{x_i}(C_P(x) - C_{P0})|_{\text{projected}}dx}{\int_0^{R_B} C_{P0}|_{\text{projected}}dx} = \int_0^{\tilde{x}_i}(\tilde{C}_P(\tilde{x}) - 1)|_{\text{projected}}d\tilde{x}, \qquad (6.1)$$

where C_P is the particle concentration, C_{P0} is the background particle concentration, R_B is the beacon radius, and x_i is the crossover location. Points in Fig. 6.3B show the increase in the projected particle count over time for the different beacon sizes, measured directly from experiments. Theoretical predictions (line) from numerical computations, described below, agree well with the experiments.

6.2 Theory

6.2.1 Formation of solute wake behind a sedimenting beacon

SI interactions driven by sedimenting beacons can be treated in two steps. First, the SI beacon emits solute as it sediments, which is advected to the solute wake behind the beacon. The initial solute concentration profile can be obtained by solving convection-diffusion equation, using steady-state fluid flow around the falling beacon. Second, "far" behind the sedimenting beacon, the fluid is largely stagnant. Solute in the wake diffuses radially outward, obeying the transient mass conservation equation. Particle concentration can be calculated, by balancing particle diffusion to the diffusiophoretic migration in response to the solute concentration gradient. Separation of time scales in this manner allows us to independently calculate the solute distribution in the trailing wake at steady-state, and the subsequent transient diffusion in a static fluid.

We solve the first part in a frame, co-moving with the beacon, where the flow of fluid

past the beacon is fully-developed. The steady-state fluid flow around the beacon follows

$$\tilde{\nabla}^2\tilde{\boldsymbol{u}} - \tilde{\boldsymbol{\nabla}}\tilde{p} - Re\,(\tilde{\boldsymbol{u}}\cdot\tilde{\boldsymbol{\nabla}}\tilde{\boldsymbol{u}}) = 0, \tag{6.2}$$

$$\tilde{\boldsymbol{\nabla}}\cdot\tilde{\boldsymbol{u}} = 0. \tag{6.3}$$

where the velocity field $\boldsymbol{u} = U_B\tilde{\boldsymbol{u}}$ is non-dimensionalized by the beacon sedimentation velocity U_B, pressure $p = \tilde{p}\mu U_B/R_B$ by the viscous pressure scale with the fluid viscosity denoted by μ, and positions $r = R_B\tilde{r}$, $z = R_B\tilde{z}$ by the beacon radius R_B. With these scales, the Reynold number $Re = \rho_f U_B R_B/\mu$, where ρ_f is the fluid density.

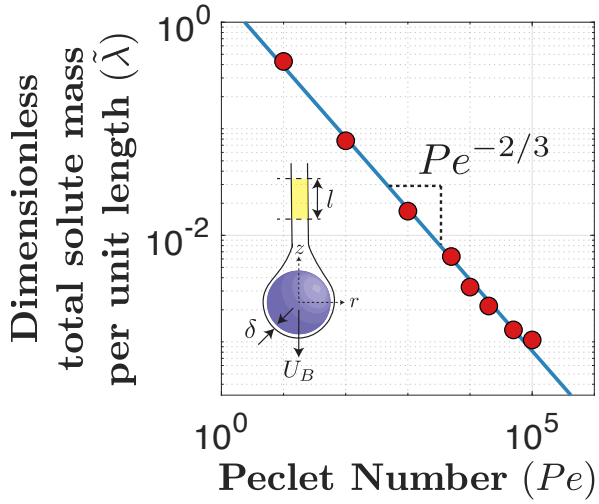

Figure 6.4: The dimensionless total mass of solute collected in the trailing wake of a sedimenting beacon, per unit length of the wake. Points show numerically computed values of dimensionless the mass per length vs. Pe (Eq. 6.6), while the solid line represents the $Pe^{-2/3}$ scaling derived in Eq. (6.10). Computations are performed in the Stokes flow regime with $Re = 0$.

Solute emitted from the beacon is advected by the fluid flow, obeying

$$\tilde{\nabla}^2\tilde{C}_S - Pe\,(\tilde{\boldsymbol{u}}\cdot\tilde{\boldsymbol{\nabla}}\tilde{C}_S) = 0, \tag{6.4}$$

where solute concentration $C_S = C_0\tilde{C}_S$ is non-dimensionalized by the solute saturation

concentration C_0, which gives a Peclet number $Pe = U_B R_B / D_S$, where D_S is the solute diffusivity in solution.

Figure 6.4 shows the dimensionless solute mass per unit length of the wake behind a sedimenting beacon. Individual data points are obtained using COMSOL to solve the fluid velocity profile (Eqs. 6.2 - 6.3 with $Re = 0$), which is used to solve for the solute concentration profile $\tilde{C}_S$ via Eq. (6.4). Finite Re has little effect, as discussed later. The total solute mass per unit length (λ) of the wake is then calculated according to

$$\lambda = 2\pi \int_0^\infty C_S(r, z = 10R_B) r dr, \tag{6.5}$$

which is normalized by $A_B C_0$ to give

$$\tilde{\lambda} = \frac{\lambda}{A_B C_0} = \frac{1}{2} \int_0^\infty \tilde{C}_S(\tilde{r}, \tilde{z} = 10) \tilde{r} d\tilde{r}, \tag{6.6}$$

where $A_B = 4\pi R_B^2$ is the surface area of the beacon. Note that the location $\tilde{z} = 10$ in the computations where $\tilde{\lambda}$ is calculated is arbitrary: solute conservation requires the solute mass per unit length to be independent of the location behind the beacon. Figure 6.4 reveals $\tilde{\lambda}$ to decay as $Pe^{-2/3}$ (solid line). We now present a simple scaling argument to rationalize this Pe dependence.

For fast falling beacons ($Pe > 1$), we expect the solute to form a convection-diffusion boundary layer around the beacon. Since the beacon surface obeys the no-slip boundary condition, we further expect the fluid immediately adjacent to the beacon to be locally undergoing shear flow. Therefore, the mass transport boundary layer δ obeys Lévêque scaling[2,3]

$$\delta = R_B Pe^{-1/3}. \tag{6.7}$$

The total number of solute molecules leaving the beacon per unit time can be approximated as

$$J = A_B D_S \nabla C_S \approx 4\pi R_B^2 D_S \frac{C_0}{\delta}. \tag{6.8}$$

The beacon sediments with velocity U_B. Thus, in time $t = l/U_B$, the flux J forms a solute wake, with total solute mass M given by

$$M \approx J \frac{l}{U_B}. \tag{6.9}$$

From Eqs. (6.8) and (6.9), the total mass of solute per unit length can then be expressed as

$$\lambda = \frac{M}{l} = \frac{J}{U_B} \approx \frac{4\pi R_B^2 D_S C_0}{R_B Pe^{-1/3} U_B} \approx A_B C_0 Pe^{-2/3}. \tag{6.10}$$

Equation (6.10) predicts $\tilde{\lambda} = \lambda / A_B C_0$ to scale like $Pe^{-2/3}$, consistent with the result obtained from full computations (Fig. 6.4).

6.2.2 DP response of suspended particles to the solute flux

Once the beacon falls far enough, the fluid can be considered to be largely stagnant. In the absence of flow, solute in the wake diffuses radially out according to

$$\frac{\partial \tilde{C}_S}{\partial \tilde{t}} - \tilde{\nabla}^2 \tilde{C}_S = 0, \tag{6.11}$$

where time is non-dimensionalized by the solute diffusion time scale $t = R_B^2 / D_S \tilde{t}$.

The particle concentration C_P in the suspension then evolves under this solute con-

centration gradient, as the particles migrate diffusiophoretically with velocity[4–6]

$$\boldsymbol{u_{DP}} = D_{DP}\boldsymbol{\nabla} \ln C_S, \tag{6.12}$$

where D_{DP} is the DP mobility, whose sign and magnitude depends upon the nature of the solute-particle interaction. Particles diffuse and move diffusiophoretically, obeying

$$\frac{\partial \tilde{C}_P}{\partial \tilde{t}} - \tilde{D}_P \tilde{\nabla}^2 \tilde{C}_P + \tilde{D}_{DP} \tilde{\boldsymbol{\nabla}} \cdot (\tilde{\boldsymbol{\nabla}} \ln \tilde{C}_S \, \tilde{C}_P) = 0. \tag{6.13}$$

Two additional dimensionless parameters emerge from Eq. (6.13): the ratio of particle to solute diffusivity

$$\tilde{D}_P = \frac{D_P}{D_S}, \tag{6.14}$$

and the ratio of the DP mobility to the solute diffusivity

$$\tilde{D}_{DP} = \frac{D_{DP}}{D_S}. \tag{6.15}$$

Figure 6.5A shows the evolution of the particle concentration profile (Eq. 6.13). As soon as solute starts diffusing out from the wake, a radial concentration gradient is established, which causes the particles to migrate via DP. Initially, solute concentration gradients ($\boldsymbol{\nabla} C_S$) are sharp, so $\boldsymbol{\nabla} \ln C_S$ is large enough that the DP flux ($\boldsymbol{u_{DP}} C_P$) is much greater than the diffusive particle flux ($D_{DP}\boldsymbol{\nabla} C_P$). Thus, the particle concentration in the center of the wake initially increases (assuming DP migration to be directed up the gradient, blue data points in Fig. 6.5A). Over time, $\boldsymbol{\nabla} \ln C_S$ weakens as solute diffuses out; at some time $t_{\max}$, particle diffusion starts to outcompete $\boldsymbol{u_{DP}}$, and the particle wake spreads (red data points in Fig. 6.5A). Eventually, the particle population relaxes back

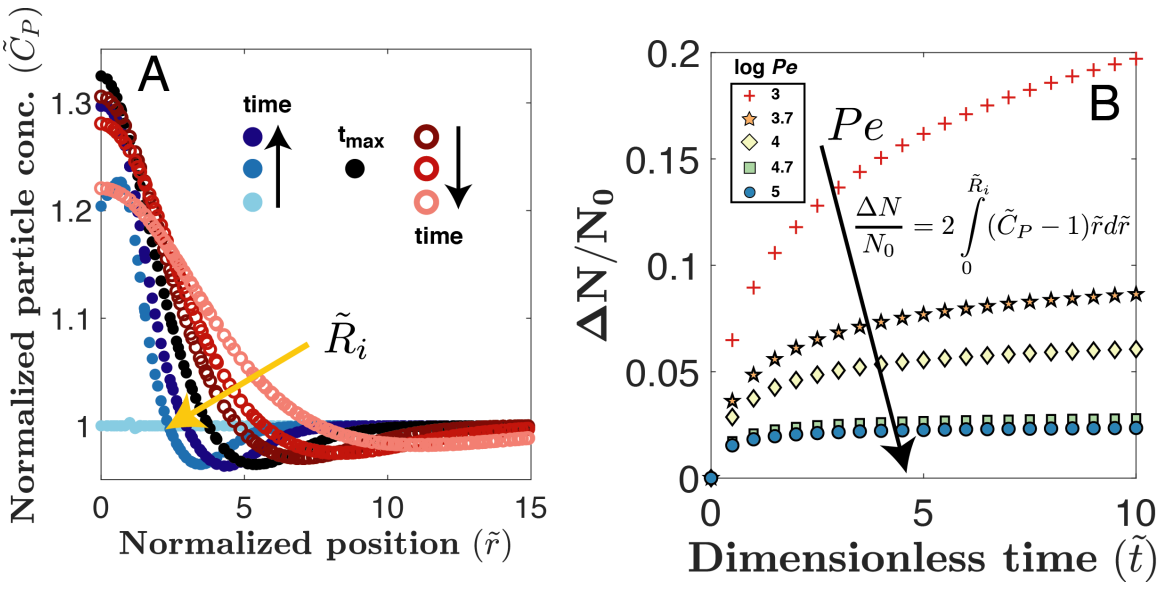

Figure 6.5: Particle response to the solute wake established by a falling beacon that attracts colloids. (A) Evolution of particle concentration in suspension after the formation of the wake. Blue points show the initial increase in the particle concentration, until it reaches a maximum value at $t_{\max}$. This maximum concentration profile is shown by the black points. The concentration relaxes as the DP velocity diminishes and the particles diffuse out, which is shown by the red points. The concentration profiles are calculated with $\tilde{D}_P = 10^{-1}$ and $\tilde{D}_{DP} = 10^{-1}$ to match the strengths of the particle diffusive flux and the DP flux and therefore, show their competition. (B) Excess particles ($\Delta N = N_{SI} - N_0$) collected by the wake of sedimenting beacons vs. Pe. Computations for the excess particles are performed with $\tilde{D}_P = 10^{-4}$ and $\tilde{D}_{DP} = 10^{-1}$ to match experimentally realistic conditions.

to its equilibrium uniform distribution (not shown).

The excess number of particles collected by the solute wake can be computed from the particle concentration profile C_P. From Fig. 6.5A, we note that $R_i(t)$ represents the boundary of the collection region, where the excess particles in the center of the wake is balanced by a net depletion of particles. Therefore, we compute the excess collected particles ($\Delta N = N_{SI} - N_0$) according to

$$\Delta N = 2\pi \int_0^{R_i} (C_P(r) - C_{P0}) r dr, \tag{6.16}$$

where we only account for the particle concentration up to R_i. Without DP, the particle concentration everywhere in the suspension would remain C_{P0} and ΔN would be zero. We further normalize ΔN by the number of particles swept by the sedimenting beacon

$$N_0 = 2\pi \int_0^{R_B} C_{P0} r dr = \pi R_B^2 C_{P0}, \tag{6.17}$$

to obtain

$$\frac{\Delta N}{N_0} = 2 \int_0^{\tilde{R}_i} (\tilde{C}_P(\tilde{r}) - 1) \tilde{r} d\tilde{r}. \tag{6.18}$$

Figure 6.5B shows computed values of the normalized excess particles collected in the wake ($\Delta N/N_0$) vs. time as a function of Pe (or sedimenting beacon velocity U_B). Figure 6.5B shows that the normalized excess collection $\Delta N/N_0$ decreases, as Pe increases. This computationally obtained trend is consistent with experimental measurements shown in Fig. 6.3, where $\Delta N/N_0$ decreases with increasing size of the falling beacon (or sedimenting velocity).

6.2.3 The effect of DP mobility and particle diffusivity on colloidal collection

We now examine the effect of the relative diffusivity $\tilde{D}_P$ and scaled DP mobility $\tilde{D}_{DP}$ on the particle collection in the wake, for a fixed beacon size (or Pe). Since Pe is kept fixed and its choice can be arbitrary, details of the initial solute concentration profile in the wake are not important. Therefore, to simplify our computational model, we approximate the initial solute distribution in the wake with a step function [of unit height and width, such that $\tilde{\lambda} = 1/4$, $Pe \approx \mathcal{O}(20)$], which eventually diffuses into a Gaussian profile. Figure 6.7A shows computed values of the excess particles collected in the wake

($\Delta N/N_0$, Eq. 6.18) as a function of relative diffusivities $\tilde{D}_P$, and scaled DP mobility $\tilde{D}_{DP}$. Normalizing this excess collection by the scaled DP mobility $\tilde{D}_{DP}$ collapses the different curves for all combinations of $\tilde{D}_{DP}$ and $\tilde{D}_P$, except in the physically unrealistic limit $\tilde{D}_P \sim \mathcal{O}(1)$. Without fully solving the coupled system of Eqs. (6.11 and 6.13), we propose a simple scaling argument to capture this data collapse, and predict the temporal evolution profile for the excess number of particles.

Integrating Eq. (6.13) over the area where there is an excess concentration of particles ($\Delta C_P > 0$) gives

$$\begin{aligned}\frac{\partial \Delta N}{\partial t} = \frac{\partial}{\partial t}\int_0^{\tilde{R}_i} \Delta\tilde{C}_p \tilde{r} d\tilde{r} = \int_0^{\tilde{R}_i} \{\, \tilde{D}_P \frac{1}{\tilde{r}}\frac{\partial}{\partial \tilde{r}}\left[\tilde{r}\frac{\partial}{\partial \tilde{r}}(1+\Delta\tilde{C}_P)\right] - \\ \tilde{D}_{DP}\frac{1}{\tilde{r}}\frac{\partial}{\partial \tilde{r}}\left[\tilde{r}\frac{\partial}{\partial \tilde{r}}\ln\tilde{C}_S(1+\Delta\tilde{C}_P)\right] \,\} \tilde{r} d\tilde{r},\end{aligned} \tag{6.19}$$

where $\Delta\tilde{C}_P = \tilde{C}_P - 1$, and $\Delta\tilde{C}_P = 0$ at $\tilde{r} = \tilde{R}_i$. Normalizing Eq. (6.19) by the number N_0 of particles swept by the sedimenting beacon (Eq. 6.17) and simplifying yields

$$\begin{aligned}\frac{\partial}{\partial \tilde{t}}\frac{\Delta N}{N_0} &= 2\left[\tilde{D}_P\tilde{r}\frac{\partial}{\partial\tilde{r}}(1+\Delta\tilde{C}_P) - \tilde{D}_{DP}\tilde{r}\frac{\partial}{\partial\tilde{r}}\ln\tilde{C}_S(1+\Delta\tilde{C}_P)\right]_{\tilde{r}=\tilde{R}_i} \\ &\approx \tilde{D}_P\tilde{r}\frac{\partial\tilde{C}_P}{\partial\tilde{r}}\bigg|_{\tilde{r}=\tilde{R}_i} - \tilde{D}_{DP}\tilde{r}\frac{\partial}{\partial\tilde{r}}\ln\tilde{C}_S\bigg|_{\tilde{r}=\tilde{R}_i}.\end{aligned} \tag{6.20}$$

Comparing the two terms on the right hand side of Eq. (6.20), reveals that the DP term always dominates the particle diffusion term, irrespective of the value of $\tilde{D}_{DP}$, so long as the normalized particle diffusivity $\tilde{D}_P$ is less than 1 (Fig. 6.6). Neglecting the diffusive term in Eq. (6.20) then gives

$$\frac{\partial}{\partial \tilde{t}}\frac{\Delta N}{N_0} \approx -\tilde{D}_{DP}\tilde{r}\frac{\partial}{\partial\tilde{r}}\ln\tilde{C}_S\bigg|_{\tilde{r}=\tilde{R}_i}. \tag{6.21}$$

Equation (6.21) predicts $\Delta N/N_0$ to be directly proportional to the normalized DP

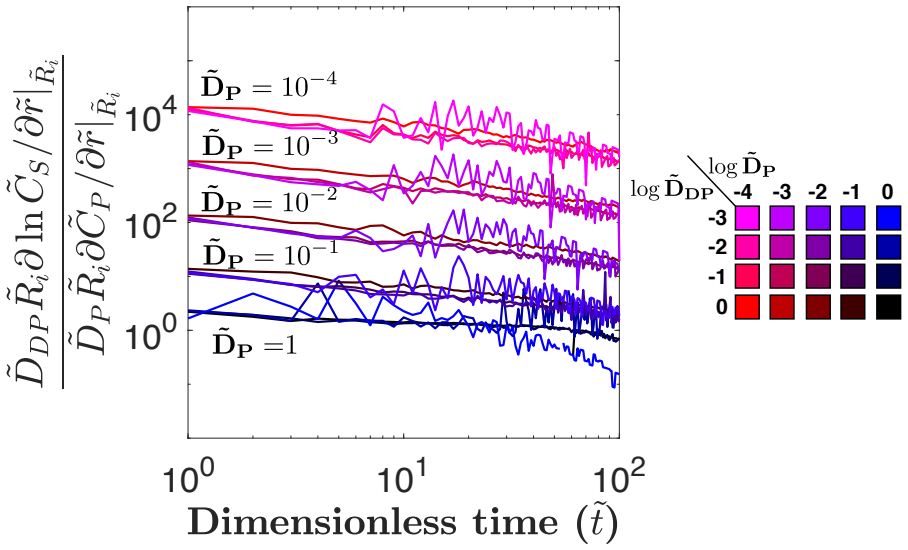

Figure 6.6: Comparison between the strength of the diffusiophoretic particle flux driven by the solute concentration gradient ($\tilde{D}_{DP}\tilde{R}_i\tilde{\boldsymbol{\nabla}}\ln\tilde{C}_S|_{\tilde{R}_i}$) and the diffusive particle flux ($\tilde{D}_P\tilde{R}_i\tilde{\boldsymbol{\nabla}}\tilde{C}_P|_{\tilde{R}_i}$), at different combinations of the scaled DP mobility $\tilde{D}_{DP}$ and particle diffusivity $\tilde{D}_P$.

mobility $\tilde{D}_{DP}$, as evidenced by the data collapse observed in Fig. 6.7A. Furthermore, Fig. 6.6 shows the DP term and the particle diffusivity term in Eq. (6.20) to be within the same order of magnitude, when $\tilde{D}_P = \mathcal{O}(1)$. Therefore, the scaling does not work in this case (Fig. 6.7A) since the diffusive term in Eq. (6.20) can no longer be ignored.

Equation (6.21) can be used to predict the excess particles collected (or depleted) by the wake of a falling beacon, and requires the solute concentration profile C_S in solution to be known.

Computations (Fig. 6.7B) reveal the total number of particles collected to depend on the total solute mass $\tilde{\lambda}$ in the wake, but not on the detailed solute profile, since thin wakes (blue) collect the same particle excess ΔN as wide pulses (red) of same overall mass $\tilde{\lambda}$. Since the number of particles collected does not depend on the thickness of the solute pulse, the initial wake may be assumed to be infinitely thin. This assumption then allows the diffusive solute concentration profile in solution to be approximated as a

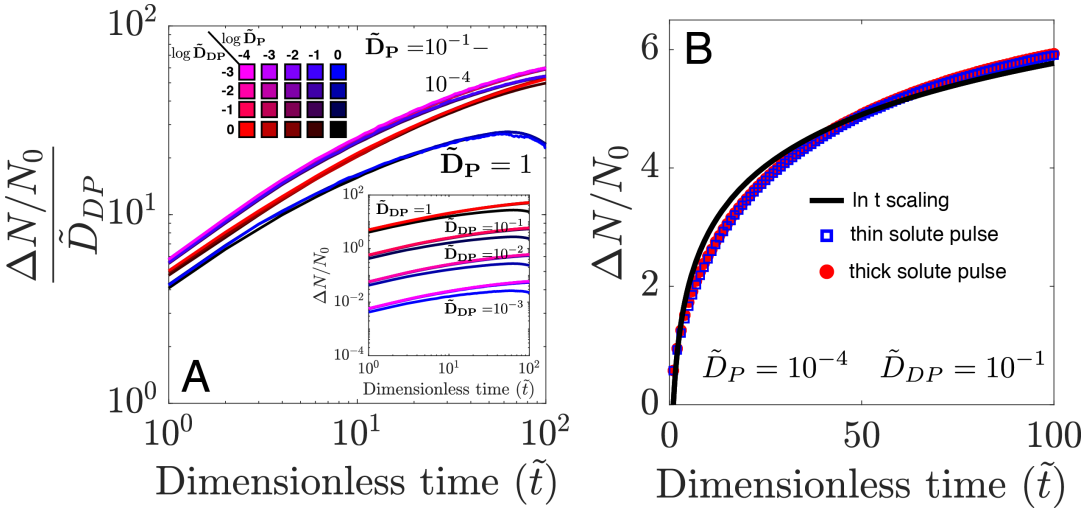

Figure 6.7: Effect of particle diffusivity ($\tilde{D}_P$) and DP mobility ($\tilde{D}_{DP}$) on colloidal collection (A) Excess particles collected in the wake ($\Delta N = N_{SI} - N_0$), due to their DP migration towards higher solute concentration vs. non-dimensional time. The different curves collapse when scaled by the dimensionless DP mobility ($\tilde{D}_{DP}$). Inset shows the raw, unscaled data. (B) Maintaining a constant mass of solute yet changing the width of the initial solute pulse does not impact the number of particles collected, shown by the red and blue data points. Moreover, the increase in particle count follows a logarithmic scaling in time (black curve). Computations in (B) are performed with $\tilde{D}_P = 10^{-4}$ and $\tilde{D}_{DP} = 10^{-1}$, motivated by experimentally realistic conditions. Time is non-dimensionalized by solute diffusion time scale, R_B^2/D_S.

Gaussian distribution, which in polar coordinates can be expressed as

$$C_S(r,t) = \frac{\lambda}{4\pi D_S t} \exp\left(-\frac{r^2}{4D_S t}\right) \tag{6.22}$$

Using this approximation for C_S in Eq. (6.21) predicts

$$\frac{\Delta N}{N_0} \approx \tilde{D}_{DP}\ \tilde{R}_i^2\ \ln \tilde{t}. \tag{6.23}$$

Note that to arrive at Eq. (6.23), we made the assumption that the cutoff location R_i is independent of time. This approximation appears to be a resonable one, when colloidal diffusion is slow and the particle concentration relaxes gradually ($\tilde{D}_P < 1$). We

verify the validity of this approximation, by tracking the evolution of $\tilde{R}_i$ over time in our computations (Fig. 6.8).

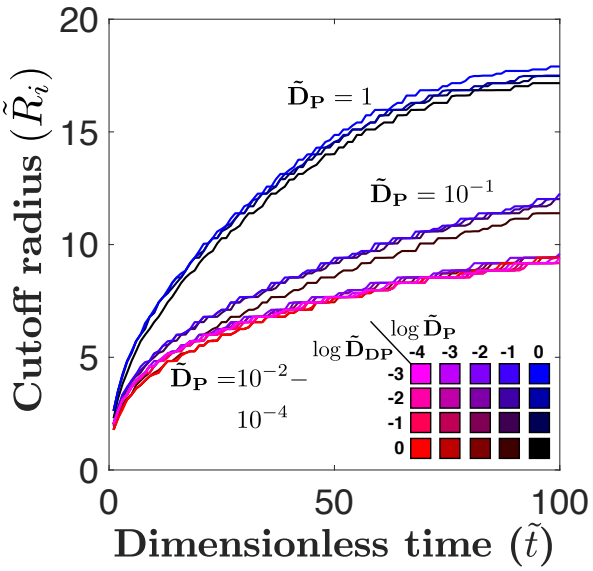

Figure 6.8: Temporal evolution of the cutoff location $\tilde{R}_i$ beyond which, the excess particles collected in the wake is balanced by a net depletion of particles in the suspension, at different combinations of the scaled DP mobility $\tilde{D}_{DP}$ and particle diffusivity $\tilde{D}_P$.

Two qualitative features emerge from the preceding scaling analysis. First, Eq. (6.23) predicts the excess number of particles in the wake ($\Delta N/N_0$) to be directly proportional to the scaled DP mobility $\tilde{D}_{DP}$, which explains the data collapse observed in Fig. 6.7A. Second, the particle count in the wake is expected to increase logarithmically with time, as is indeed observed in the full computations. Fig. 6.7B shows good agreement between the prediction from this logarithmic scaling (black curve) and the computed data (red and blue points). The slight deviation from the logarithmic trend might be due to the fact that $\tilde{R}_i$ is not a constant, but instead, changes weakly over time (Fig. 6.8).

6.3 Discussion

We have shown that the diffusiophoretic migration of suspended particles driven by the wake left behind a sedimenting beacon can be modeled by the separation of two time scales. One over which the steady-state solute concentration profile is established in the wake, and the other over which transient solute diffusion occurs in the quiescent fluid. We also demonstrated that the particle transport in the wake's vicinity is a balance between particle diffusion and advection due to the diffusiophoretic migration of particles under the solute flux.

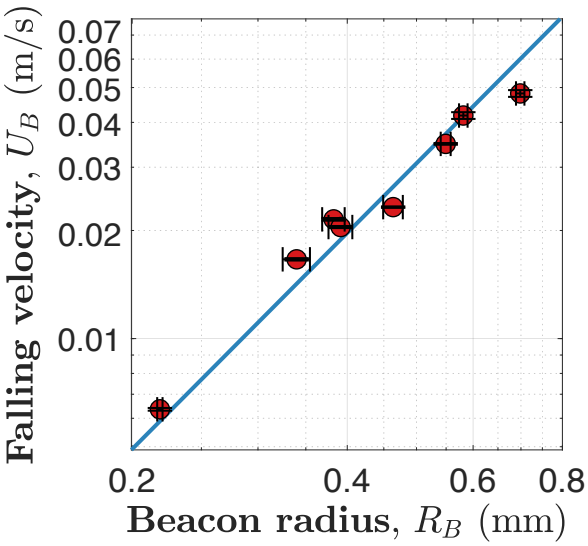

Figure 6.9: The falling velocity of ionogel beacons of different sizes. Points are velocities and radii calculated from movies of experiments while the solid line represents prediction from Eq. 6.24. Error bars show standard deviations in the measured velocities and radii.

Equations (6.2 - 6.4) can predict the steady-state characteristics of the solute distribution in the wake of a beacon, moving with any arbitrary velocity U_B, and therefore, are generally valid across all values of Re and Pe. For the special case of beacons sedimenting under gravity, however, the velocity in the Stokes flow limit ($Re < 1$) can be approximated

according to[7]

$$U_B = \frac{2}{9}\frac{\Delta\rho g R_B^2}{\mu}, \tag{6.24}$$

where $\Delta\rho = \rho_B - \rho_f$ is the difference in density of the beacon (ρ_B) and the fluid (ρ_f), and g is the acceleration due to gravity. Therefore, for freely-falling beacons in Stokes flow, Re and Pe can simply be expressed in terms of the size of the sedimenting beacon

$$Re = \frac{\rho_f U_B R_B}{\mu} \propto R_B^3, \tag{6.25}$$

$$Pe = \frac{U_B R_B}{D_S} \propto R_B^3. \tag{6.26}$$

Figure 6.9 shows the sedimenting velocities of ionogel beacons with different sizes, where points show the experimentally calculated velocities, while the line represents predictions from Eq. (6.24). The experimental measurements show good agreement with theory, using $\Delta\rho = 154$ kg/m^3 in Eq. (6.24) as the only fitting parameter.

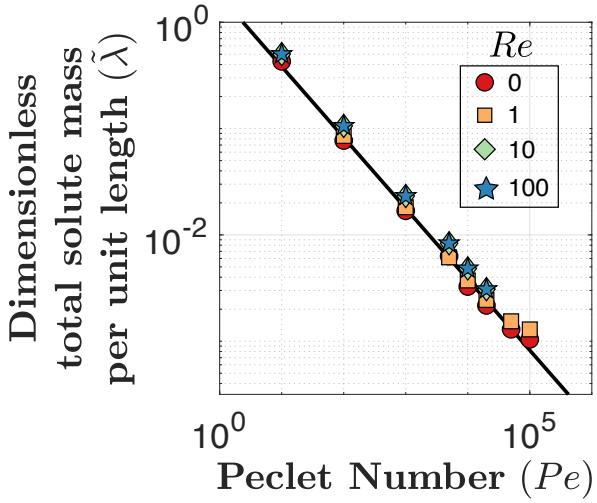

Figure 6.10: Dimensionless total solute mass per unit length ($\tilde{\lambda}$) of the wake, vs Pe, as a function of Re. Computations (points) reveal $\tilde{\lambda}$ to be independent of Re, scaling as $Pe^{-2/3}$ (line), irrespective of Re.

The total solute mass per unit length of the wake is expected to scale like $Pe^{-2/3}$ (Eq. 6.10). Although the scaling analysis makes no assumption about the Re, the computations in Fig. 6.4 are performed in the Stokes flow limit, with $Re = 0$. Figure 6.10 shows computations performed in the regime of inertially dominated momentum transport ($Re > 0$). A remarkable conclusion that can be drawn from Fig. 6.10 is that the total solute mass collected in the wake remains independent of Re and only depends on Pe (at least in the limit of $0 \leq Re \leq 100$). We therefore expect the $Pe^{-2/3}$ dependence of $\tilde{\lambda}$ (Eq. 6.10) to be generally valid across arbitrary values of Re, as shown by the solid black line in Fig. 6.10.

6.4 Conclusion

Soluto-inertial beacons, that establish long-lasting chemical gradients, can drive long-range diffusiophoretic migration of colloids. Although we had already demonstrated this concept in controlled 2D microfluidic geometries, here we showed that beacon additives can also drive long-range interactions in bulk, 3D suspensions. We specifically explored the high Pe limit, where macroscopic beacons sediment within the suspension and their sedimenting velocity advects some amount of solute in the trailing wake. In this limit, the beacon sedimentation is fast, such that the solute in the wake subsequently diffuses out in a relatively stagnant fluid. This solute flux then drives the diffusiophoretic migration of nearby suspended objects.

Based on the results described here, we further envision slowly falling beacons in the low Pe limit or even freely suspended beacons ($Pe = 0$) to not only induce migration of passive particles in the suspension, but also interact with each other. Interactions between such "active beacons" would suggest interesting possibilities in 3D self assembly and autonomous propulsion, akin to the interactions between active materials on 2D

planar surfaces reported previously.[8–13]

6.5 Materials and Methods

6.5.1 Sample cell fabrication

A 3 mm thick piece of acrylic is cut with a computer-controlled laser cutter (Trotec Speedy 100) in the dimensions of the sample chamber (6 mm wide and 40 mm tall). The acrylic is sandwiched between two glass slides and the assembly is sealed with UV curable glue (NOA-81; Norland Adhesive). The cell is then covered with a glass cover slip with a hole drilled in the center to provide access. Figure 6.11 shows a schematic of the sample cell.

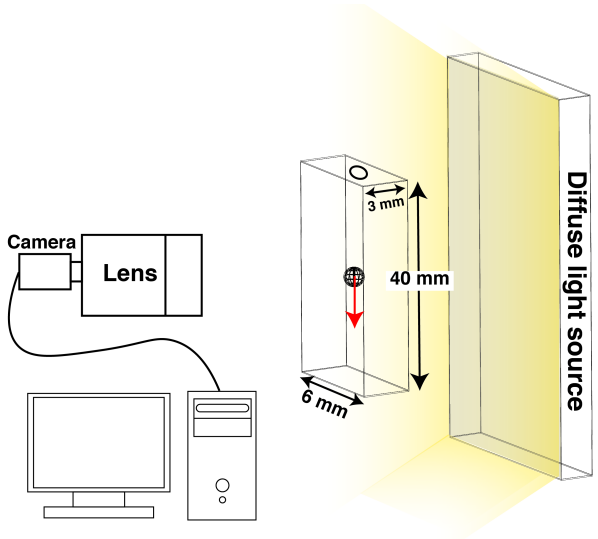

Figure 6.11: The experimental setup used to record the transmitted light intensity through a suspension of negatively charged polystyrene colloids. A uniform, diffuse white light source is held behind the sample cell containing the suspension. The sample cell itself is 40 mm tall, 6 mm wide and 3 mm thick, with the side walls made out of acrylic. The front, back, and top of the cell are enclosed with glass slides. A hole is drilled on the top slide that provides access into the cell. A CCD camera attached to a zoom lens is used to record images of the experimental setup at 10 frames per second.

6.5.2 Sample preparations

The ionogel precursor solution is prepared by mixing 32% (vol/vol) polyethylene glycol-diacrylate (PEG-DA) 700 (Sigma-Aldrich) with 66% (vol/vol) pure $[C_4mim][I]$ (Sigma-Aldrich) and 2% (vol/vol) photoinitiator (2-hydroxy-2-methylpropiophenone; Sigma-Aldrich). A drop of the precursor solution is carefully injected into a 1000 csT silicone oil (Sigma-Aldrich) bath and immediately placed inside a UV oven for 1 minute. The precursor drop cures under UV light into a spherical hydrogel, as it slowly falls down in the highly viscous oil bath. The polymerized gel (ionogel beacon) is subsequently scooped from the bottom of the bath and cleaned with a dry lens tissue. The SDS gel precursor is prepared by mixing 32% (vol/vol) PEG-DA with an SDS stock solution and 2% (vol/vol) photoinitiator, such that the resultant SDS concentration in the precursor is 200 mM. Spherical beacons are then created following the same technique as the ionogel beacons. Suspension of polystyrene (PS) particles is prepared by mixing 24% (vol/vol) glycerol (Thermo-Fisher) with 76% (vol/vol) deionized (DI) water and 0.025% (vol/vol) carboxylated (negatively charged), surfactant free PS beads, 2 μm in diameter (Magsphere Inc. SFCA002UM).

6.5.3 Image recording and data analysis

The suspension is illuminated with a thin laser sheet (Laserland 11061123) and a zoom lens (Computar MLM-3XMP) attached to a high speed camera (Ximea MQ013MG-ON) is used to record images from the bottom, at a frame rate of 100 frames/sec, to obtain the image stack shown in Fig. 6.1F. We hypothesize that the center of the image (Fig. 6.1F) looks dark, because the fallen beacon at the bottom of the sample cell blocks the scattered light from the colloids to enter the lens/camera.

Clamps are used to hold the sample cell in place and a zoom lens (Navitar Zoom

7000) attached to a CCD camera (Thorlabs DCU223M) is used to record images from the side (Fig. 6.2), at a frame rate of 10 frames/sec. A uniform, diffuse white light source is held behind the cell to maintain bright-field illumination throughout the experiment (Fig. 6.11). Image recording is started and the beacon is gently introduced into the sample cell with a pair of tweezers.

A calibration curve is obtained for the transmitted light intensity captured by the camera vs particle concentration in the suspension (Fig. 6.12). This calibration curve is subsequently used to obtain the particle distribution profiles from the brightfield images of the actual experiments. The excess amount of particles collected in the wake is then calculated from the particle concentration profiles, using the trapezoidal rule to evaluate the integral in Eq. 6.1.

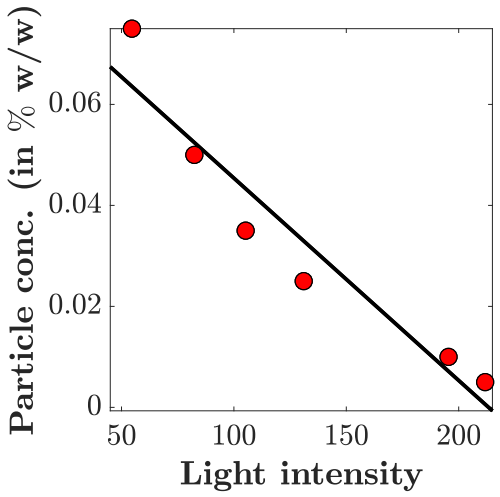

Figure 6.12: Calibration curve used for calculating the concentration of colloids in the suspension from the transmitted light intensity.

The falling beacon velocity in Fig. 6.9 is calculated by measuring the frame by frame displacement of the beacon from the recorded images. These measurements are then averaged over all the frames where displacement is observed, except the one where the beacon hits the bottom of the sample cell. The error bars show the standard deviation in averaging. The size and the location of the beacon are directly approximated from the

images, using the `imfindcircles` package on MATLAB.

6.5.4 COMSOL modeling

The `Laminar flow` and the `Transport of diluted species` modules in COMSOL Multiphysics are used to numerically solve the system of coupled differential equations (Eqs. 6.2, 6.3 and 6.4) in a 2D axisymmetric geometry. The computations are performed in the beacon's frame of reference; the beacon is kept fixed, while steady, fully-developed fluid flow is imposed at the sedimenting beacon velocity (corresponding to different values of Pe) to obtain solute concentration profile in the wake at steady state. The fluid flow is subject to the following boundary conditions

$$\tilde{\boldsymbol{u}} = 1\hat{\boldsymbol{e}}_{\boldsymbol{z}} \quad \text{at the bottom "inlet" of the computational domain, } \tilde{\mathrm{z}} = -100, \tag{6.27}$$

$$\tilde{p} = 0 \quad \text{at the top "outlet" of the computational domain, } \tilde{\mathrm{z}} = 100, \tag{6.28}$$

$$\tilde{\boldsymbol{u}} = 0 \quad \text{at the beacon} - \text{liquid interface}, \tag{6.29}$$

$$\hat{\boldsymbol{n}} \cdot \tilde{\boldsymbol{\nabla}}\tilde{\boldsymbol{u}} = 0 \quad \text{at } \tilde{\mathrm{r}} = 0 \text{ and the "outer edge" of the computational domain}, \tag{6.30}$$

where $\hat{\boldsymbol{e}}_{\boldsymbol{z}}$ is the unit normal in the $z-$direction, and $\hat{\boldsymbol{n}}$ is the outward unit normal on the respective boundaries. The following boundary conditions are imposed on the solute concentration

$$\tilde{C}_S = 1 \quad \text{at the beacon} - \text{fluid interface}, \tag{6.31}$$

$$\tilde{C}_S = 0 \quad \text{at the bottom "inlet" of the computational domain}, \tag{6.32}$$

$$\hat{\boldsymbol{n}} \cdot \tilde{\boldsymbol{\nabla}} C_S = 0 \quad \text{at } \tilde{\mathrm{r}} = 0 \text{ , at the top "outlet" and the "outer edge" of the computational domain.} \tag{6.33}$$

The steady-state solute concentration profile in the wake and uniform particle distribu-

tion in the suspension are used as initial conditions to solve Eqs. 6.11 and 6.13 using the `Transport of diluted species` and the `General form of PDE` modules respectively, in a 1D axisymmetric geometry. Symmetry at the center and no flux boundary conditions at the edges of the computational domain are imposed on the solute and particle concentrations, implying

$$\hat{\boldsymbol{n}} \cdot \tilde{\boldsymbol{\nabla}} \tilde{C}_S = 0 \quad \text{at } \tilde{\mathrm{r}} = 0, \text{ and the "outer edge".} \tag{6.34}$$

$$\hat{\boldsymbol{n}} \cdot \tilde{\boldsymbol{\nabla}} \tilde{C}_P = 0 \quad \text{at } \tilde{\mathrm{r}} = 0, \text{ and the "outer edge".} \tag{6.35}$$

Numerical solution to these equations reveals the particle distribution profile $\tilde{C}_P$.

The Parametric Sweep option on COMSOL is used to perform computations for several permutations and combinations of the design parameters. Computed values of the solute and particle concentration profiles are subsequently exported in matrix form, which are post processed and analyzed on MATLAB.

Acknowledgements

We gratefully acknowledge support from the National Science Foundation (Grant CBET-1438779) and the Saudi Arabian Oil Company (Saudi Aramco, Contract A-0002-2018). Any opinion, findings, and conclusions or recommendations expressed in this material are those of the authors and do not necessarily reflect the views of the National Science Foundation. A portion of this work was performed in the Microfluidics Laboratory within the California NanoSystems Institute, supported by the University of California, Santa Barbara and the University of California, Office of the President, and in the Shared Experimental Facilities of the Materials Research Science and Engineering Center at UCSB (MRSEC NSF DMR 1720256).

Bibliography

[1] Berg J. *An Introduction to Interfaces & Colloids: The Bridge to Nanoscience*. World Scientific 2010.

[2] Lévêque MA. The laws of heat transmission by convection. *Les Annales des Mines: Memoires.* 1928; 12(13): 201-299.

[3] Leal L. *Advanced Transport Phenomena: Fluid Mechanics and Convective Transport Processes*. Cambridge Series in Chemical EngineeringCambridge University Press 2007.

[4] Prieve DC. Migration of a colloidal particle in a gradient of electrolyte concentration. *Advances in Colloid and Interface Science.* 1982; 16: 321–335.

[5] Prieve DC, Anderson JL, Ebel JP, Lowell ME. Motion of a particle generated by chemical gradients. Part 2. Electrolytes. *Journal of Fluid Mechanics.* 1984; 148: 247.

[6] Anderson JL, Prieve DC. Diffusiophoresis: Migration of Colloidal Particles in Gradients of Solute Concentration. *Separation & Purification Reviews.* 1984; 13(1): 67–103.

[7] Lamb H, Caflisch R. *Hydrodynamics*. Cambridge Mathematical LibraryCambridge University Press 1993.

[8] Liebchen B, Niu R, Palberg T, Löwen H. Unraveling modular microswimmers: From self-assembly to ion-exchange-driven motors. *Phys. Rev. E.* 2018; 98: 052610.

[9] Moerman PG, Moyses HW, Wee EB, et al. Solute-mediated interactions between active droplets. *Phys. Rev. E.* 2017; 96: 032607.

[10] Niu R, Palberg T, Speck T. Self-assembly of colloidal molecules due to self-generated flow. *Phys. Rev. Lett..* 2017; 119: 028001.

[11] Niu R, Botin D, Weber J, Reinmüller A, Palberg T. Assembly and speed in ion-exchange-based modular phoretic microswimmers. *Langmuir.* 2017; 33(14): 3450-3457. PMID: 28346787.

[12] Theurkauff I, Cottin-Bizonne C, Palacci J, Ybert C, Bocquet L. Dynamic clustering in active colloidal suspensions with chemical signaling. *Physical Review Letters.* 2012; 108(June): 1–5.

[13] Palacci J, Sacanna S, Steinberg AP, Pine DJ, Chaikin PM. Living crystals of light-activated colloidal surfers. *Science.* 2013; 339: 936–340.

Chapter 7

Extensions and implications of the soluto-inertial effect

The ability to induce and sustain non-equilibrium, directed motion of microscopic objects over macroscopic length scales can have far reaching consequences. Situations where colloidal transport is diffusion limited can especially benefit from the soluto-inertial concept. Here we discuss some of the potential applications of this effect, with the goal of addressing important industrial challenges and current technological limitations.

7.1 Navigating complex dead-end geometries

Transporting fluid and/or colloids into dead-end pores is challenging, because pressure driven fluid flow is simply not an option. Advection is therefore restricted, and the only mode of transport available for suspended objects to enter and access these pores is diffusion. A micron sized colloid, however, would take about 23 days to diffuse a length of just 1 mm. On the other hand, if the particle was subjected to move with a steady velocity of even 1 μm/s, typical of phoretic motion,[1] it could cover that 1 mm distance in

less than 20 minutes. In fact, recent studies have shown diffusiophoretic (DP) migration velocities in such dead-end geometries to reach up to 50 μm/s.[2,3]

The situation gets more complicated, if particles were to navigate a complex, labyrinth-like network of pores and preferentially move to a specific target location. Again, simply relying on diffusive particle transport would mean waiting days for the particles to traverse even small distances. Moreover, diffusion by definition implies particles would explore all options in the network equally. However, if chemical gradients could somehow be established in these complex geometries, particles would phoretically migrate in the direction where the gradient is the strongest and therefore, towards a specific target in a fraction of the diffusive time.

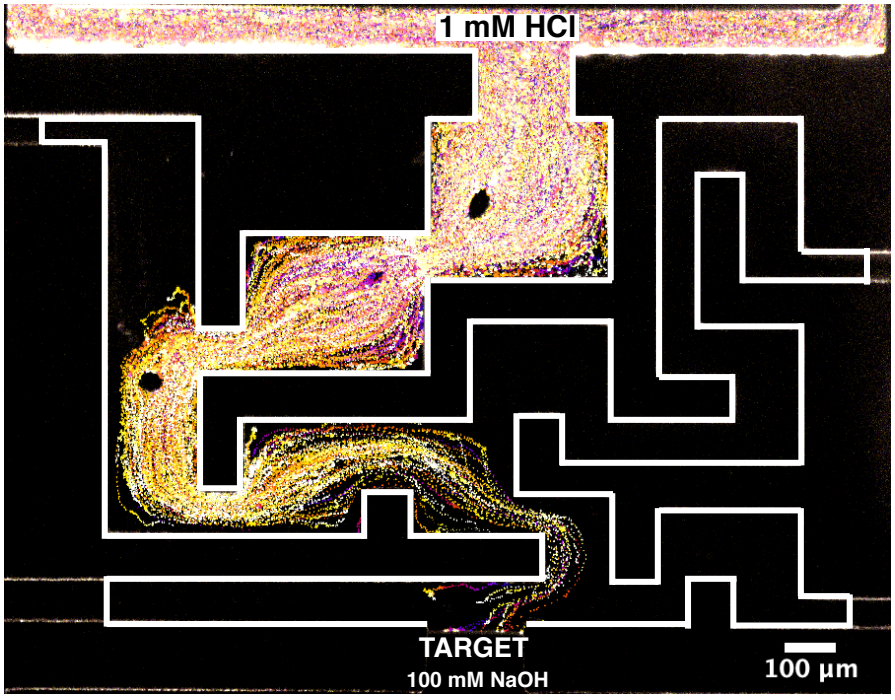

Figure 7.1: Solving a microfluidic maze via diffusiophoresis. A proton gradient established across a microfluidic maze, causes negative particles to diffusiophoretically move from an acidic to basic zone, down the gradient. In doing so, the particles solve the maze in about 10 minutes. The streak lines show a steady particle flux along the shortest path that solves the maze, with no flux recorded in any of the other dead ends within the maze.

To demonstrate this idea, we designed a microfluidic maze and established a proton gradient across it, to visualize the DP response of particles. Figure 7.1 shows the maze, where negatively charged polystyrene particles in 1 mM HCl solution enter the maze at the top. A 100 mM solution of NaOH is flowed at the the bottom of the maze next to a hydrogel (target), that allows diffusive transport of NaOH but blocks convection. Maintaining this steady flux of acid and base at the top and bottom of the maze respectively, causes negatively charged particles that migrate down the proton gradient[4] to solve the maze in about 10 minutes. In the absence of the gradient, the particles would have taken almost a year to traverse that same distance. Moreover, Fig. 7.1 also reveals the DP motion of the particles to be directed only along the shortest path that solves the maze, where the proton gradient is the strongest. The other four dead ends receive no particle flux.

Although the concentration gradient in this example is externally maintained with a constant supply of HCl and NaOH, the hydrogel at the bottom of the maze could, in principle, be replaced by a beacon loaded with a strongly partitioning or associating base. In fact, the beacon could be loaded with any solute that would interact with the surface of the colloid and cause it to migrate via DP, so long as the beacon maintains the gradient over long durations. In that case, a constant supply of solute would not be required as the beacon itself would maintain solute fluxes that are strong enough to drive DP migration. Note that we simply chose this acid-base model based on our observation in Chapter 4, which revealed that reactive solutes sustain stronger and longer lasting gradients.

The transport of suspended objects within such complicated geometries is quite relevant in the context of tissue engineering, material/gel synthesis and recovery, drug delivery,[5] transport in biochannels,[6] as well as oil exploration and recovery. For example, oil detection in the underground porous rock formations could be significantly expedited, by manipulating chemical gradients to deliver colloidal "detection agents" via DP. Moreover, recent studies have shown the injection of fresh water to dramatically enhance oil recovery,

compared to the injection of sea water.[7] While the origin of this effect is still unclear, the diffusio-osmotic flow driven by the salinity gradient (between the fresh water and connate fluids) could indeed play an important role in enhancing transport within these pores.[8]

Note that oil reservoirs have a high salt concentration, typically on the order of several thousand ppm. DP velocities that scale as the inverse of solute concentration ($u_{DP} \propto \nabla \ln C_S$) therefore, might be quite weak under such conditions (Fig. 5.9). For effective soluto-inertial interactions, sustained chemical gradients must also generate appreciable colloidal motion. Thus, an alternative approach to drive particle migration is necessary in cases where solute concentrations in solution are already high and DP motion is suppressed.

7.2 Soluto-capillary migration of colloids

We noted in Chapter 4 that interfacial tension gradients along the surface of a colloid generate Marangoni flows, which cause the drops to propel.[9] The motion of the drops is known as soluto-capillary migration and can serve as an alternative method to propel suspended materials, so long as the solute can modify their surface tension.

In Chapters 3 and 4, we had demonstrated soluto-capillary migration of decane drops under SDS gradients generated by a PEG-DA beacon source that associates with SDS (Fig. 3.3E, Fig. 4.5C,D). Here, we show soluto-capillary migration driven by a beacon that partitions solute, instead of associating with the solute. Octanol serves as the beacon phase and partitions butanol, with an octanol-water partition coefficient $P_{\text{ow}} \approx 8$.[10] The beacon therefore establishes long lasting butanol gradients, driving soluto-capillary motion of decane drops over tens of minutes.

Butanol reduces the surface tension of the suspended oil drops in water. Therefore, the side of the oil drop directly facing the butanol source has a lower surface tension

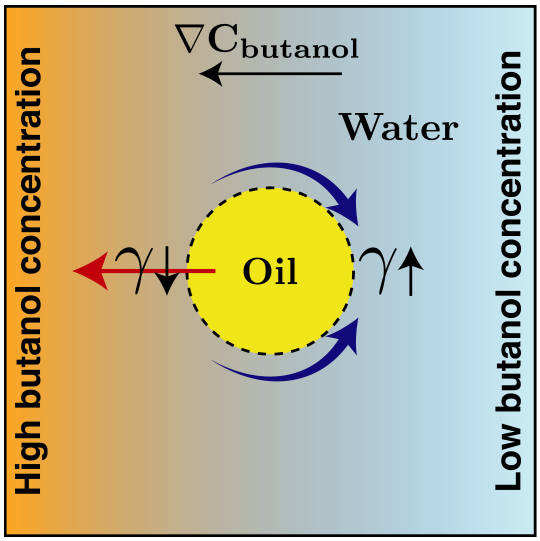

Figure 7.2: Mechanism of soluto-capillary droplet migration. The gradient of a solute that reduces the surface tension (γ) of a suspended drop, generates Marangoni flows along the surface of the drop. These flows are directed towards the higher surface tension side of the drop, causing the drop to propel towards regions of low surface tension or high solute concentration.

than the side facing away from the source (Fig. 7.2). The surface tension gradient along the droplet surface drives a Marangoni flow towards the high surface tension side, which in turn propels the drop to move in the opposite direction. Oil drops thus migrate up butanol gradients, i.e. towards beacon sources (Fig. 7.3A) or away from beacon sinks (Fig. 7.3C).

Soluto-capillary migration velocities (u_{SC}) scale with ∇C_S,[9] instead of the $\nabla \ln C_S$ in DP. We therefore use

$$u_{SC} = D_{SC} \nabla C_S, \tag{7.1}$$

to model the velocities observed in Figs. 7.3A and 7.3C. Assuming D_{SC} to be a constant that does not depend on C_S, and normalizing all data by the maximum measured and computed values, reveals good agreement between the measured and computed velocities,

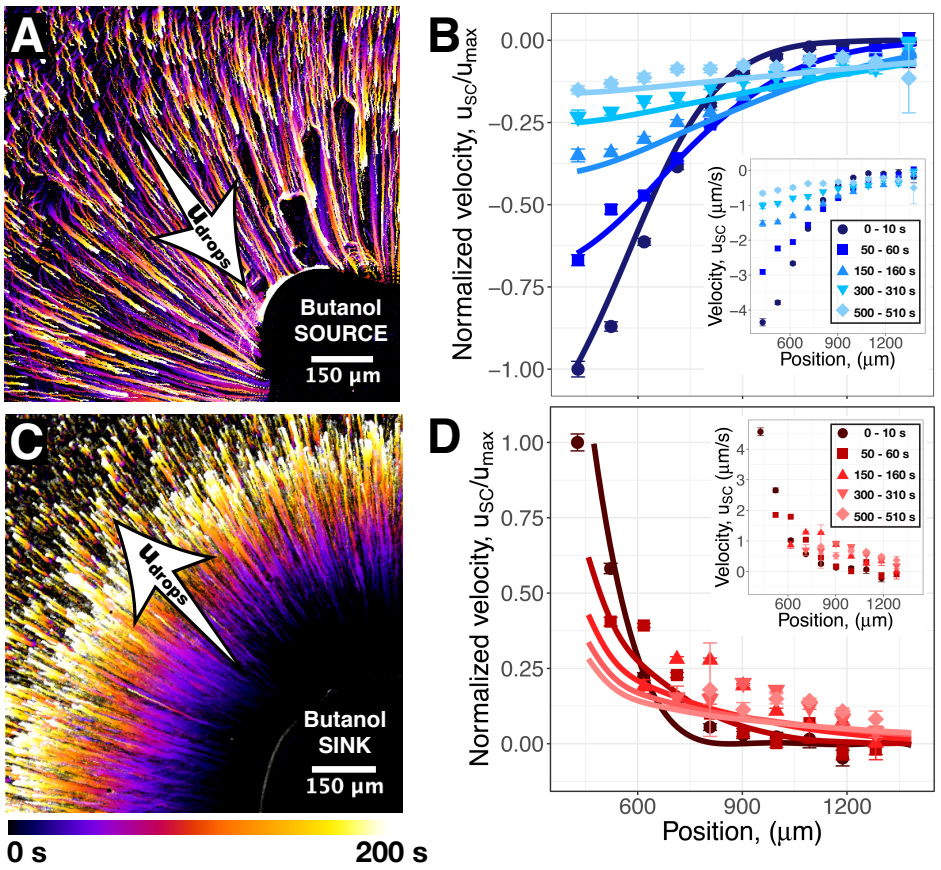

Figure 7.3: Soluto-capillary migration of decane drops driven by an octanol beacon that partitions butanol. (A) A beacon source, unloading butanol attracts oil drops. (B) Migration velocities (u_{SC}) follow a ∇C_S scaling, predictions (lines) from which agree well with experimentally measured data (points). The measured and computed velocities are normalized by the maximum measured and computed values respectively, to facilitate direct comparison between the two. Inset shows the raw experimentally tracked particle velocities. (C) A beacon sink, on the other hand, repels the oil drops. (D) Points represent the measured velocities while lines show computations based on $u_{SC} \propto \nabla C_S$ scaling. Inset shows the raw experimental data.

for both the source (Fig. 7.3B) and the sink (Fig. 7.3D).

While Fig. 7.3 shows the migration of oil (decane) drops in water, Fig. 7.4 on the other hand, shows the soluto-capillary migration of water drops in oil (octanol). The solute in this case is acetamide, with an octanol-water partition coefficient $P_{\text{ow}} \approx 0.055$,[10] which partitions into the aqueous beacon phase. The beacon source slowly unloads acetamide, which reduces the surface tension of the suspended water drops in oil. The acetamide

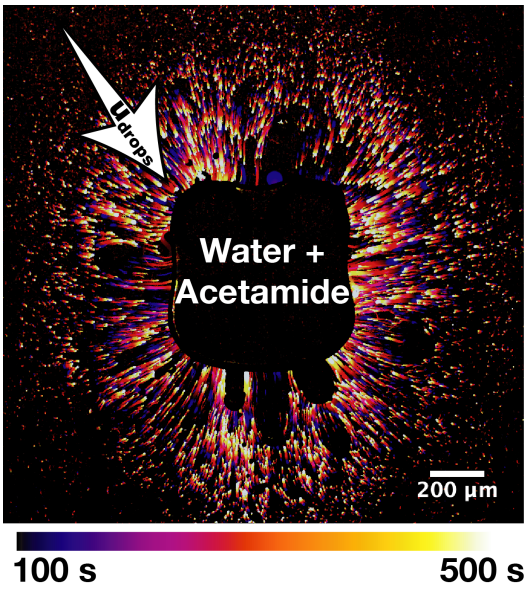

Figure 7.4: Soluto-capillary migration of water drops in oil, under acetamide gradients. The beacon phase (water) partitions acetamide and therefore, unloads it slowly into the background oil (octanol) phase, establishing long-lasting acetamide gradients. Acetamide reduces the surface tension of the water drops in oil, causing them to migrate towards the beacon due to the resultant solutal-Marangoni flows.

gradient established by the beacon, therefore, creates a surface tension gradient along the surface of the drops, causing them to move towards the beacon.

Equation 7.1 suggests soluto-capillary particle migration to only depend on the gradient of the solute concentration. Thus, appreciable motion can be driven, so long as the solute gradients are strong and the solute itself is interfacially active and capable of modifying the particle's surface tension. Of course, this mode of transport is only restricted to particles that have a finite surface tension such as oil drops in water or vice-versa, and would not be valid for solid objects. Nevertheless, the soluto-capillary strategy serves as a powerful transport mechanism that can boost the migration of particles in scenarios where the DP motion is weak, for example in highly concentrated salt solutions.

7.3 Clarifying dilute suspensions: Beacons embedded with flocculants

Several industrial applications such as water treatment and tailings management require the removal of fine particles from suspensions. In most of these applications, coagulants and flocculants are typically used to initiate colloidal aggregation and promote suspension flocculation.[11] This method generally works well for concentrated suspensions, where particles do not have to migrate large distances to find neighbors, and stick to form aggregates. However, triggering flocculation in dilute suspensions can be rather challenging.

In dilute suspensions, the diffusion limitation of particle aggregation, also known as Smoluchowski coagulation,[12] becomes important.[13] The time scale for aggregation τ_{DLA} depends on the ratio of the diffusion limited rate constant k_0 and the number density of colloids in the suspension N_0,

$$\tau_{\mathrm{DLA}} \propto \frac{k_0}{N_0}. \tag{7.2}$$

Thus, the lower the number density N_0, the longer is the aggregation time τ_{DLA}. The flocculation time scale further increases by the stability ratio[14,15]

$$W \sim k_0 \exp\left(\frac{\Delta G}{k_B T}\right), \tag{7.3}$$

for colloids with a repulsive interaction potential ΔG (such as those stabilized by electrostatics). Although coagulants (multivalent ions) and flocculants (polyelectrolytes) are often added to suspensions to reduce or eliminate this interaction potential ΔG, the Smoluchowski diffusion limitation still holds.

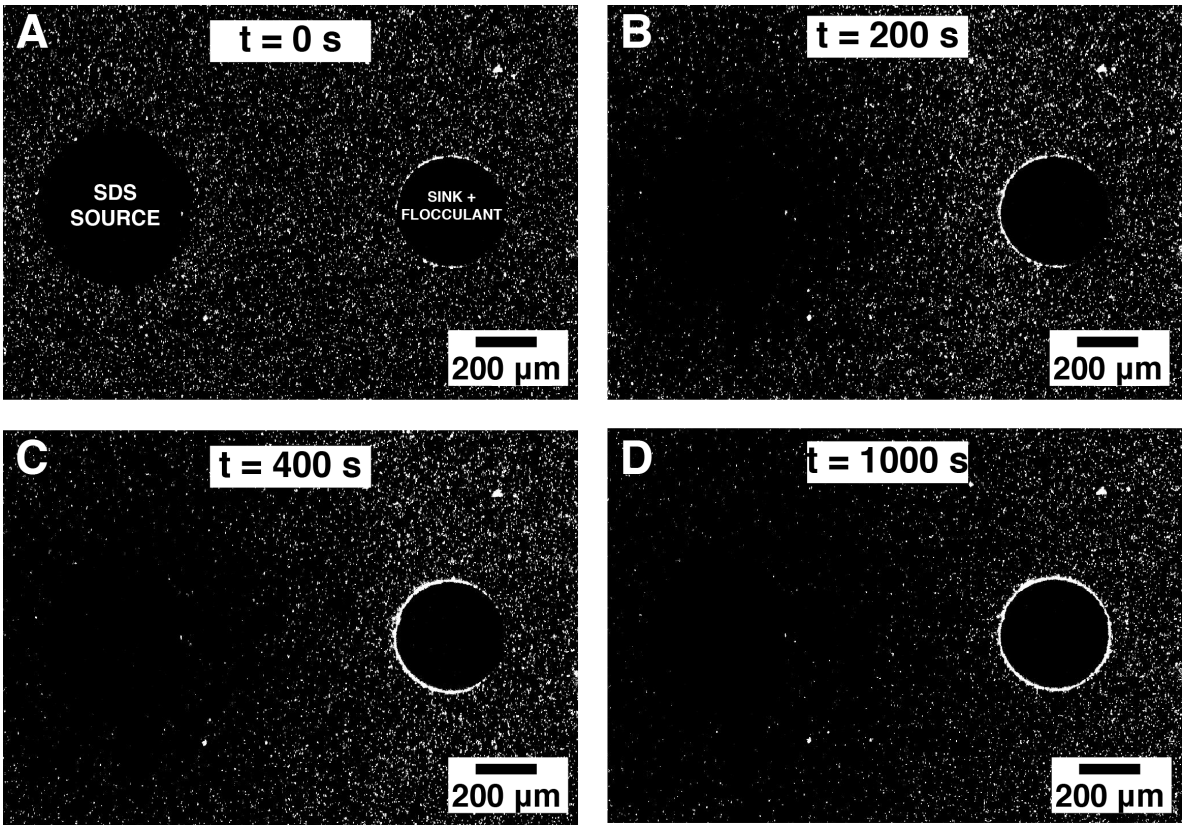

Figure 7.5: "Sticky" SI beacons embedded with flocculants. Dipolar SDS flux generated by a beacon source and a sink drive negatively charged polystyrene particles to migrate to the sink. The sink is decorated with the industrial flocculant (cationic polyelectrolyte), causing particles to irreversibly stick to it. This particle aggregation can be seen as a bright ring that forms around the periphery of the sink over time. Micrographs show particle distribution in the suspension at (A) t = 0 s, (B) t = 200 s, (C) t = 400 s, and (D) t= 1000 s.

The soluto-inertial strategy provides a way to direct colloids to specific locations in a controlled manner and thereby, increase the local number density of particles in those regions. A clear consequence of increasing N_0 would be a reduction in the amount of time needed to form aggregates, as predicted by Eq. 7.2. To demonstrate this idea, we revisit the soluto-inertial dipole interactions introduced in Chapter 4. We noted previously that the dipolar solute flux between the source and the sink, causes particles to migrate and accumulate near the sink. In this previous demonstration, however, the particles were

simply concentrated near the sink, but they did not aggregate because of the inter-particle repulsion.

Here, we use the same approach to direct particles but instead, decorate the beacon sink with an industrial flocculant (cationic polyelectrolyte). The flocculant reduces the repulsive interaction potential between the charged colloids. Thus, the particles are not only steered by the beacons to accumulate around the sink, but they also stick to it due to the presence of the flocculant (Fig. 7.5). This aggregation is observed as a bright ring of particles that line the periphery of the sink, which was not observed in the previous realization of the dipolar interaction. This simple observation, therefore, suggests the soluto-inertial concept, coupled with a strategy to eliminate the repulsion between colloids to be a potent alternative to drive dilute suspension flocculation.

7.4 Materials and Methods

7.4.1 Maze experiments

Device fabrication

The microfluidic maze is fabricated in microfluidic stickers (NOA 81, Norland Adhesives). The master is made in the cleanroom by photo-patterning a 30 μm thick layer of the negative photoresist (SU8 2015) on a 3-inch Si wafer, following standard photo-lithography techniques. The master is then used to make a negative polydimethylsiloxane (PDMS) replica mold of the design. The PDMS mold is used as a stamp to make the microfluidic stickers device, following the procedures outlined in.[16] Holes are punched in the sticker to provide fluid access into the device through the inlets and outlets. A PDMS block is further ozone bonded to the device, with holes punched at the inlet and outlet locations that provide support to the connector pins and tubings. The device is then baked at 120

^{o}C for at least 4 hours to strengthen bonding.

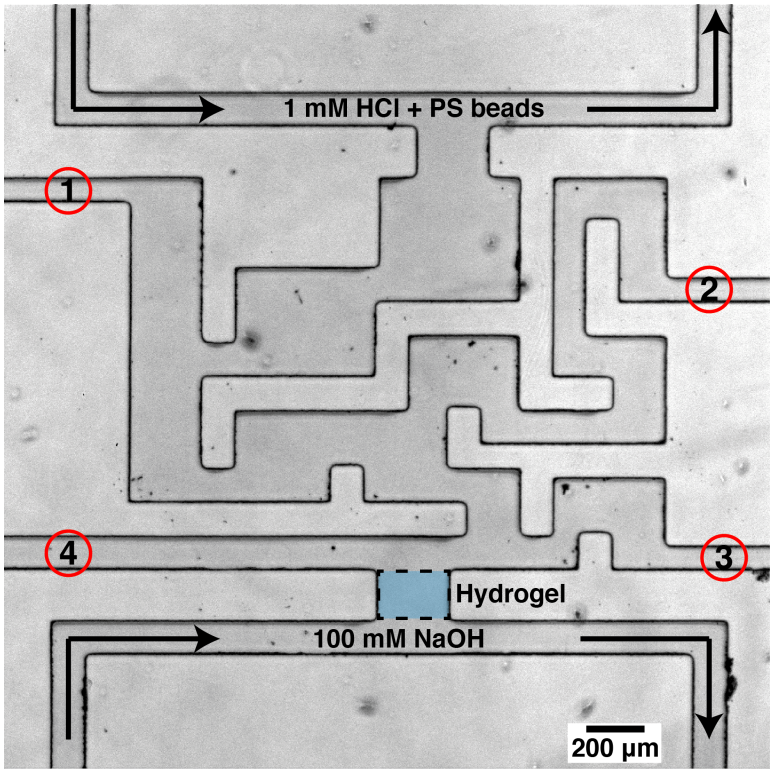

Figure 7.6: Microfluidic maze device configuration. The hydrogel is first fabricated using the microfluidic projection lithography technique.[17] The device is subsequently flushed with water. The dead ends (labeled 1 – 4) are initially open, and created by injecting the channels with NOA-81 UV curable glue and then quickly curing with UV light , one by one. The experiments are performed by supplying the bottom channel with 100 mM NaOH solution (which diffuses through the gel) and the top channel with negative PS beads in 1 mM HCl solution.

Experiments

The device (Fig. 7.6) is first injected with the hydrogel precursor solution (95 %vol/vol PEG400-DA, Polysciences + 5%vol/vol photoinitiator 2-hydroxy-2-methylpropiophenone, Sigma Aldrich). The PEG-DA gel is then fabricated at the location shown in Fig. 7.6, using the microscope projection lithography technique,[17] and separates the maze from the channel that supplies NaOH. The unreacted precursor is flushed out of the device with

water. Initially, the "dead-ends" are open to the flow of liquid, to enable fluid access into the device through pressure driven fluid flow. Once the precursor solution is flushed out with water, NOA-81 is injected through each of the four channels $(1, 2, 3, 4)$ and quickly polymerized with UV light to block them (one after the other, $1 \rightarrow 2 \rightarrow 3 \rightarrow 4$). The bottom and top channels are subsequently supplied with 100 mM NaOH and 1 mM HCl solutions respectively, with 0.25% (vol/vol) fluorescent sulfonated polystyrene beads, 1 μm in diameter (FS03F; Bangs Laboratories) added to the HCl solution.

7.4.2 Soluto-capillary experiments

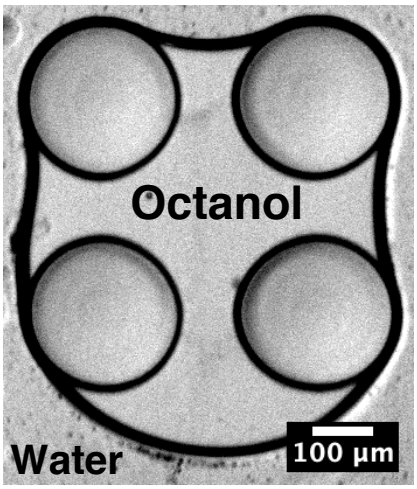

Figure 7.7: Octanol beacon trapped inside a microfluidic channel by four hydrophobic gel posts, surrounded by water.

Microfluidic devices for SI experiments are prepared as described previously,[18] although partitioning beacons (octanol, Sigma Aldrich) are held in place differently than adsorbing beacons (PEG-DA). The octanol beacon is trapped in the channel using four hydrophobic gel posts (Fig. 7.7). The posts are fabricated from a 95% vol/vol polymer (Trimethylolpropane triacrylate, Polysciences) and 5% vol/vol photoinitiator (2-hydroxy-2-methylpropiophenone, Sigma Aldrich) precursor solution, via the projection lithography

technique used previously to fabricate the PEG-DA beacons.[18] Octanol is presaturated overnight with deionized (DI) water, then flowed into the channel. Octanol is subsequently driven out of the channel using pressurized air, leaving octanol drop trapped between the four hydrophobic posts. This trapped octanol then serves as the beacon (Fig. 7.7).

The SI source beacons are loaded with butanol by filling channels with 0.5 M butanol (Sigma Aldrich) solution in DI water, which is left in contact with the octanol beacon for 20 minutes. SI experiments are initiated by introducing a suspension of surfactant-free decane drops (2% vol/vol in DI water, Sigma Aldrich). The flow is then stopped and image series is recorded (Andor iXon 885 fluorescence camera) with a 4× objective at 1 frame per second with an exposure time of 0.1 s.

SI sink experiments are performed by preparing an "empty" octanol beacon, then injecting a suspension of decane drops dispersed in 0.5 M butanol solution in DI water. The flow is then stopped, and image series is recorded. The recorded images are subsequently imported in R and analyzed via the same particle tracking routine used in our previous work[18] to obtain the particle velocity profiles.

The aqueous (DI water) beacon that generates acetamide gradients (Fig. 7.4) is held in place with four PEG-DA beacons (95 %vol/vol PEG400-DA, Polysciences + 5%vol/vol photoinitiator 2-hydroxy-2-methylpropiophenone, Sigma Aldrich). The beacon is pre-loaded with acetamide at a final concentration of 4.375 M, and then trapped in the device with the four PEG-DA posts. Water drops are prepared by sonicating 5 % vol/vol water in octanol (presaturated with water). The suspension is then flowed into the device after which, flow is stopped and image series is recorded.

7.4.3 Beacons embedded with flocculants

The precursor solution for "sticky" beacons is prepared by mixing 0.1% wt/wt of the cationic polyelectrolyte flocculant (SNF FLOPAM FO 4650 SH) with 33% vol/vol PEG700-DA (Sigma Aldrich) and 4% vol/vol photoinitiator (2-hydroxy-2-methylpropiophenone, Sigma Aldrich) in water. The beacon hydrogel is then photo-polymerized in the microfluidic device, following the same lithography technique described before.[18] The SI source beacon is the same PEG-DA hydrogel, without the added flocculant. The protocol followed for performing the SI dipole experiments is the same as described previously in Chapter 4.

Bibliography

[1] Abécassis B, Cottin-Bizonne C, Ybert C, Ajdari a, Bocquet L. Boosting migration of large particles by solute contrasts. *Nature materials.* 2008; 7: 785–789.

[2] Shin S, Um E, Sabass B, Ault JT, Rahimi M, Warren PB. Size-dependent control of colloid transport via solute gradients in dead-end channels. *Proceedings of the National Academy of Sciences.* 2016; 113(2): 257-261.

[3] Kar A, Chiang TY, Ortiz Rivera I, Sen A, Velegol D. Enhanced transport into and out of dead-end pores. *ACS nano.* 2015; 9(1): 746–53.

[4] Shi N, Nery-Azevedo R, Abdel-Fattah AI, Squires TM. Diffusiophoretic Focusing of Suspended Colloids. *Physical Review Letters.* 2016; 258001(117): 1–5.

[5] Verma R, Garg S. Current status of drug delivery technologies and future directions. *Pharmaceutical Technology On-Line.* 2001; 25(2): 1-14.

[6] Wei G, Xi W, Nussinov R, Ma B. Protein ensembles: How does nature harness thermodynamic fluctuations for life? the diverse functional roles of conformational ensembles in the cell. *Chemical Reviews.* 2016; 116(11): 6516–6551.

[7] Lager A, Webb KJ, Collins IR, Richmond DM. Losal enhanced oil recovery: Evidence of enhanced oil recovery at the reservoir scale. In *SPE Symposium on Improved Oil Recovery*(Tulsa, Oklahoma, USA): 12Society of Petroleum Engineers 2008.

[8] Marbach S, Bocquet L. Osmosis, from molecular insights to large-scale applications. *arXiv:1902.06219v2.* 2019.

[9] Levich BG, Kuznetsov AM. On the motion of drops in liquids under the action of surface active substances. *Dokl. Acad. Nauk SSSR.* 1962; 146: 145–147.

[10] Sangster J. Octanol-water partition coefficients of simple organic compounds. *Journal of Physical and Chemical Reference Data.* 1989; 18(3): 1111-1229.

[11] Bolto B, Gregory J. Organic polyelectrolytes in water treatment. *Water Research.* 2007; 41(11): 2301 - 2324.

[12] Smoluchowski vM. Mathematical theory of the kinetics of the coagulation of colloidal solutions. *Zeitschrift für Physikalische Chemie.* 1917; 19: 129-135.

[13] Russel W, Saville D, Schowalter W. *Colloidal Dispersions.* Cambridge Monographs on MechanicsCambridge University Press 1989.

[14] Fuchs N. Über die stabilität und aufladung der aerosole. *Zeitschrift für Physik.* 1934; 89(11): 736–743.

[15] Reerink H, Overbeek JTG. The rate of coagulation as a measure of the stability of silver iodide sols. *Discuss. Faraday Soc..* 1954; 18: 74-84.

[16] Bartolo D, Degré G, Nghe P, Studer V. Microfluidic stickers. *Lab on a Chip.* 2008; 8: 274–279.

[17] Dendukuri D, Gu SS, Pregibon DC, Hatton TA, Doyle PS. Stop-flow lithography in a microfluidic device. *Lab on a Chip.* 2007; 7(7): 818–828.

[18] Banerjee A, Williams I, Azevedo RN, Helgeson ME, Squires TM. Soluto-inertial phenomena: Designing long-range, long-lasting, surface-specific interactions in suspensions. *Proceedings of the National Academy of Sciences.* 2016; 113(31): 8612-8617.

Chapter 8

Conclusion and future work

We have demonstrated a novel concept to controllably drive suspended matter to target locations that are milimeters apart. These non-equilibrium, soluto-inertial interactions are driven by chemical beacons that establish long-lasting solute concentration gradients and drive diffusiophoretic particle migration. Alternatively, beacons that release surface active solutes may further drive soluto-capillary migration of particles with finitie surface tension. The term 'soluto-inertia' is derived by analogy with thermal-inertia, wherein high heat-capacity objects in poor heat-transfer media respond very slowly to changes in environmental temperature, and therefore maintain heat flux over extended periods of time. The interactions are versatile and highly tunable since the direction as well as the magnitude of propulsion depends on the chemical properties of the particle's surface. Thus, a combination of beacons can selectively collect different species of particles from a mixture, suggesting new possibilities in suspension screening and testing. Moreover, the beacon's chemical and physical properties may further be enhanced to delay equilibration, following specific design guidelines presented in this work. Specifically, we discussed two distinct classes of beacon materials that enable sustained solute release – beacons that partition solute, and beacons that associate with solute. In fact, beacon materials may

also be chosen such that their properties can be tuned by external triggers like light or temperature, to drive soluto-inertial migration on-demand.

Most promising interactions are perhaps the ones established in bulk, three dimensional suspensions since they most closely resemble real systems of interest. Although with macroscopic, sedimenting beacons we have shown that such bulk interactions are indeed feasible (Chapter 6), we believe that we have simply scratched the surface of what is possible. The true potential of these interaction will only be revealed once the beacon size is scaled down, to create freely suspended beacons that would generate chemical gradients and also migrate in response.

8.1 Future work: Towards fully autonomous soluto-inertial beacons

The soluto-inertial interactions demonstrated in Chapters 3 and 4 are essentially between a macroscopic beacon ($\sim 200\mu$m) and micron sized colloidal particles. While this serves as a necessary first step towards understanding the range, duration and strength of these interactions, the true challenge lies in designing interactions between *suspended* colloidal beacons that simultaneously establish fluxes and migrate. As we noted in Chapter 5, the soluto-inertial unloading time strongly depends on the size of the beacon, scaling with radius as R_B^2 and therefore, reducing the beacon size would significantly limit the duration of these interactions. Moreover, beacon sedimentation introduces additional complexity. Nevertheless, Fig. 8.1 shows some of the ways in which we envision the interactions between freely suspended beacons to operate. For the purpose of this discussion, we consider three dimensional SI beacons and assume diffusiophoretic migration to be directed up the concentration gradient.

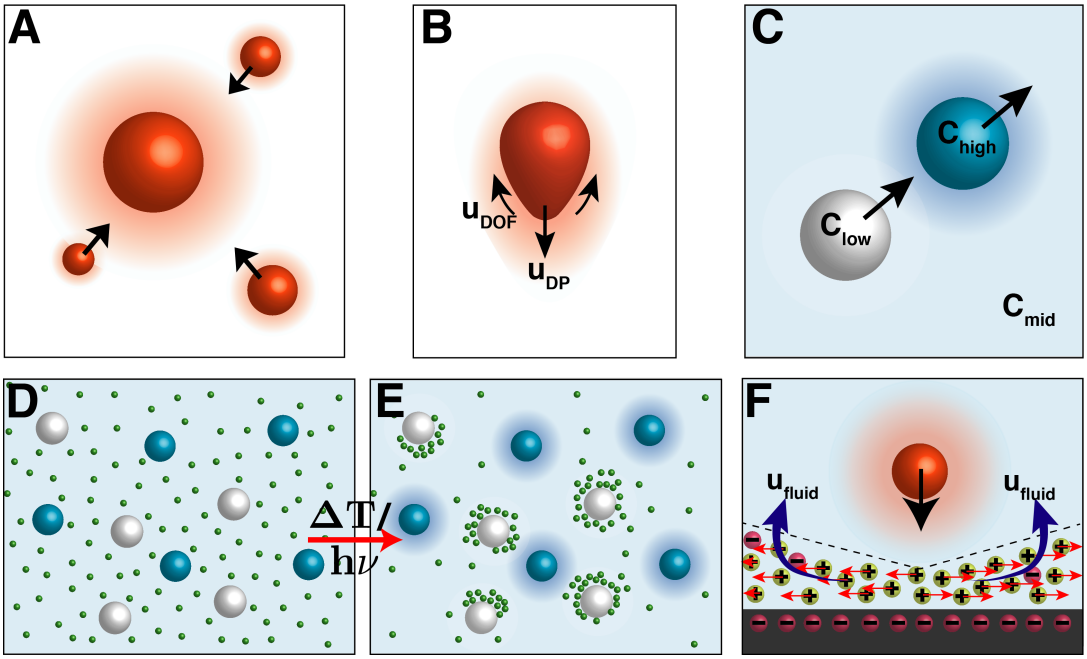

Figure 8.1: Hypothesized interactions between freely suspended SI beacons. (A) A large SI beacon establishes longer-ranged flux, thereby acting as a collector and attracting nearby, smaller beacons.(B) A physically anisotropic beacon has a higher flux at the sharp corner which causes it to spontaneously migrate. (C) Suspended SI sources and sinks chase each other. (D,E) Multiple sources and sinks establish strong local gradients that can be externally triggered to enable on-demand suspension destabilization. (F) Suspended beacons seek charged walls by driving diffusio-osmotic flow along the surface.

We expect larger SI beacons to establish longer-lasting and longer-ranging gradients than smaller SI beacons. Smaller beacons should therefore move towards the larger ones that act as sites for nucleation, thus promoting self assembly and crystal growth (Fig. 8.1A). Further, we hypothesize the behaviour of physically (or chemically) anisotropic SI beacons to be different from the spherical ones. For example, we expect regions with a higher curvature to have a higher solute out-flux, thereby inducing self-propulsion of the beacon (Fig. 8.1B). Dipole interactions between suspended beacons would give rise to the sink chasing the source (or vice versa), as one emits solute while the other absorbs (Fig. 8.1C). We also envisage the externally controllable interactions (through temperature or

light) between multiple beacon sources and sinks to provide the ability to incorporate strong local gradients in bulk suspensions on-demand (Fig. 8.1D,E). Sticky sinks (like the ones decorated with flocculants, discussed in Chapter 7) could further act as sites for the particles to aggregate and therefore, enable triggered suspension flocculation. Finally, we hope to engineer "smart beacon particles" that can interact with a wall, with a sense of direction. We anticipate a suspended beacon source in this case to set up a concentration gradient along the surface of the wall as it out-fluxes solute. This gradient should then drive a diffusio-osmotic fluid flow along the surface which, in turn, should generate a flow in the bulk that would make the particle 'sense' the gradient, and migrate towards the wall (Fig. 8.1F). Similarly, a beacon sink should be able to drive a reverse flow and migrate away from the wall. A partitioning beacon (like the ones discussed in Chapter 7) that releases a surface active solute should drive a Marangoni flow along a liquid-liquid interface, causing the beacon to migrate towards the interface and promoting faster coalescence. We expect similarly designed configurations and systems to offer exciting possibilities in active matter,[1–4] colloidal self assembly,[5,6] the creation of highly ordered colloidal structures,[7,8] and the synthesis of novel materials.

Bibliography

[1] Ebbens S. Active colloids: Progress and challenges towards realising autonomous applications. *Current Opinion in Colloid & Interface Science.* 2016; 21: 14 - 23.

[2] Liebchen B, Niu R, Palberg T, Löwen H. Unraveling modular microswimmers: From self-assembly to ion-exchange-driven motors. *Phys. Rev. E.* 2018; 98: 052610.

[3] Moerman PG, Moyses HW, Wee EB, et al. Solute-mediated interactions between active droplets. *Phys. Rev. E.* 2017; 96: 032607.

[4] Balazs AC, Fischer P, Sen A. Intelligent nano/micromotors: Using free energy to fabricate organized systems driven far from equilibrium. *Accounts of Chemical Research.* 2018; 51(12): 2979-2979. PMID: 30558428.

[5] Niu R, Palberg T, Speck T. Self-assembly of colloidal molecules due to self-generated flow. *Phys. Rev. Lett..* 2017; 119: 028001.

[6] Niu R, Botin D, Weber J, Reinmüller A, Palberg T. Assembly and speed in ion-exchange-based modular phoretic microswimmers. *Langmuir.* 2017; 33(14): 3450-3457. PMID: 28346787.

[7] Theurkauff I, Cottin-Bizonne C, Palacci J, Ybert C, Bocquet L. Dynamic clustering in active colloidal suspensions with chemical signaling. *Physical Review Letters.* 2012; 108(June): 1–5.

[8] Palacci J, Sacanna S, Steinberg AP, Pine DJ, Chaikin PM. Living crystals of light-activated colloidal surfers. *Science.* 2013; 339: 936–340.